Spring 2018

Investigation of Microfluidic Kelvin Water Dropper and Its Applications in Contact and Contactless Electrowetting

Elias Yazdanshenas
Old Dominion University

INVESTIGATION OF MICROFLUIDIC KELVIN WATER DROPPER AND ITS APPLICATIONS IN CONTACT AND CONTACTLESS ELECTROWETTING

by

Elias Yazdanshenas
M.Sc. August 2015, Old Dominion University
B.Sc. 2011, Azad University, Semnan Branch

A Dissertation Submitted to the Faculty of
Old Dominion University in Partial Fulfillment of the
Requirements for the Degree of

DOCTOR OF PHILOSOPHY

MECHANICAL AND AEROSPACE ENGINEERING

OLD DOMINION UNIVERSITY
May 2018

Approved by:

_____
Xiaoyu Zhang (Director)

_____
Shizi Qian (Member)

_____
Yan Peng (Member)

ABSTRACT

INVESTIGATION OF MICROFLUIDIC KELVIN WATER DROPPER FOR THE USE OF CONTACT AND CONTACTLESS ELECTROWETTING APPLICATION

Elias Yazdanshenas
Old Dominion University, 2018
Director: Xiaoyu Zhang

A typical Kelvin water dropper is a device that can convert gravitational potential energy to a high voltage electrostatic. This device consists of two inductors, two collectors, tubes, and electrical connections. A Kelvin water dropper is able to generate extremely high voltage by separating ions using two positive feedback loops. A Kelvin water dropper provides a low cost solution for the applications in which high voltage is needed. In the present research, low cost Microfluidic Kelvin Water Droppers (MKWDs) were developed and built in house for electrowetting applications. Two MKWDs with different tube inner diameters (254 and 508 μm) were constructed to evaluate their appropriate power output for electrowetting. It was demonstrated that higher flow rate led to higher voltage generated, whereas the MKWD with larger tube diameters generated less voltage.

Thereafter, contact electrowetting using the homemade MKWD was studied. Electrowetting is a process used to manipulate deformation of liquid droplets on a dielectric surface using an external electric field. In contact electrowetting, the droplet is in contact with a working electrode that applies the voltage. The electric field in the present research was applied using the MKWD. It was demonstrated that contact electrowetting of water droplets can be controlled using the MKWD. Then, a computational model was built to simulate the contact electrowetting using the MKWD. The model was successfully validated by comparing the experimental and simulation results.

Finally, contactless electrowetting using the MKWD was investigated. As compared to contact electrowetting, the working electrode was separated from the water droplets. When applying an electric field using the MKWD, it was observed that the water droplet first corrugated due to electrostatic attraction, and then collapsed due to electrowetting. Unlike contact electrowetting, two processes were involved in contactless electrowetting. To simulate two processes, the first model was built based on the theory of electrostatics, and the second model was based on the conventional electrowetting. Both models were validated by a nice agreement between the experimental and simulation data.

This thesis is dedicated my wife, Saharnaz Montazeri, without whose caring support it could not complete this dissertation.

ACKNOWLEDGMENTS

Many people have contributed in my dissertation. I would like to express my sincere gratitude to my family, advisors, my friends, and the staff at Old Dominion University.

My special appreciation to my wife, Saharnaz who suffered through my very painful Ph.D. process and long distance communication during the program. I love you so much no matter where I am. Thank you goes to my parents, brothers, and sister for their patience, motivation, and support.

My most warm gratitude goes to Dr. Zhang for hours of guidance during my Ph.D. program at ODU, his advice on the research, support of the research, and editing of this dissertation. I am grateful that he gave me the golden opportunity to do research under his supervision. Everything he has given me is priceless. I would like to express my thanks of gratitude to Dr. Qian, for helping me to learn COMSOL and providing me several types of equipment from his laboratory during my experiments. Thank you, Dr. Peng, for helping and advising me during my candidacy presentation and proposal defense.

Finally, thank you Mechanical and Aerospace Engineering Department, especially the Chair of the department, Dr. Sebastian Bawab, for providing the equipment and a friendly environment in which to study and perform this research. Thank you to the Batten College of Engineering and Technology Machine Shop for helping me fabricate my device and High-Performance Computing (HPC) for giving me the software.

Thank you to all the people of the Department of Mechanical and Aerospace Engineering, and it is an honor to have worked with you.

TABLE OF CONTENTS

LIST OF TABLES

LIST OF FIGURES

Figure Page

NOMENCLATURE

$E_0(z)$	Electric field
σ_0	Charge density
Z	Axis
a	Distance of radius
ε_0	Permittivity of vacuum
q_0	Charge
ρ	The thickness of the ring wire
p	The radius of the rod
L	The length of the rod
σ_s	Charge density
Uz	The potential on the rod
U_0	Potential
du	The distance of two points on the mesh
N	Equidistant points
σ_j	Discrete points
u_i	Discrete variable
u_j	Discrete points
P_i	Compact notation parameter
R	Resistance
Er	Electric field in the ring
φ	The angle that change between 0 to π

ν	Velocity
K	The complete elliptic integral of the first kind
$\mathrm{H}(\nu)$	Simplified of equation
$\tilde{\sigma}_s(u)$	A solution of the problem with fixed unity charge density on the ring
$\sigma_0(\beta)$	The charge density
Q	Charge
C	Capacitance
w	Energy
x	The distance between plugs
y	The average time
$C_{effective}$	Effective capacitance
C_{can}	The capacitance of aluminum can
C_{wire}	Connecting wires
C_{sp}	Spark plugs
Q_{ac}	Charge
V	Voltage
E_{air}	Electric filed in the air
d	The distance between the plugs
$\Delta V(t)$	Voltage difference
V_L	Voltage in left
V_R	Voltage in right
R_{RL}	Left and right beakers resistances,
C_{RL}	Left and right beakers capacitance,

t	Time
l	The separation distance of interest
A	Surface area
$\bar{E}$	The magnitude of the electric field
ε	Electric permittivity
dA	Area of the element
dl	The element of separation distance of interest,
m_d	Droplet mass
$F_{fr,d}$	The frictional force of the air on the droplet
q_d	The droplet charge
$W_{d,grav}$	Energy of gravity by droplet
g	The gravity acceleration
h'	A maximal falling height
γ	The surface tension
ω	Natural frequency
C_D	The capacitance between the ring and the water droplet
V_i	The voltage from the collector
R	Leakage resistance ground
C	The capacitance between the ring and water droplet
R_L	Leakage resistance between cans
C_L	Capacitance adjacent cans plus the capacitance of a load
ω_0	Frequency

α	Coefficient
U_0	The voltage at the time of zero
R_{Ground}	Resistance between kelvin water generator ground
C_{Load}	Capacity the load device as an example voltmeter
R	The resistance between right and left collectors
C	Capacity right and left collectors and inductors
C_{Drop}	The capacity of water drop
n	Number of the water droplets
a	Coefficients
b	Coefficients
F_{fr}	Frictional forces
μ	The viscosity of the fluid
u	Fluid velocity
β	Slip length
$\nabla \mathbf{u}$	Velocity gradient
$\mathbf{F}_s$	Surface tension force per unit volume,
$\mathbf{F}_b$	Various forces such as gravity, magnetic fields, and electric fields per unit volume.
T	Matrix transpose
δ	Direct delta function
n	Interface normal
$\mathbf{I}$	Identity matrix,
h	The grid spacing

$\emptyset$	Level set function
$\tilde{\mathbf{T}}$	Maxwell stress tensor
$\nabla \mathbf{V}$	Voltage gradient
D	The electric displacement field
γ_{SL}	Surface tension of solid-liquid interfaces
ρ_{sl}	The surface charge density of counter-ions
V	The applied voltage
v_p	The voltage of trapped charge and the capacitance across the interface
γ_0	The surface tension of solid-liquid interface at the potential zero charge
γ_{LG}	Surface tensions of interfaces liquid-gas
γ_{SG}	Surface tensions of interfaces solid-gas (γ_{SG}),
θ	Contact angle
θ_0	Initial contact angle
ε_r	Relative electrical
Vf1	Volume fraction for air
Vf2	Volume fraction of water
ε_{r1}	Absolute permittivity of air
ε_{r2}	Absolute permittivity of water

CHAPTER 1

INTRODUCTION

1.1 Kelvin Water Dropper

Conventionally electrostatic charges can be generated when two materials are rubbed each other. The phenomena can be found in our daily life such as rubbing silk with plastic, removing a sweater in the winter, etc. Historically, a lot of research was carried out to find a way to actually apply the electrostatic generators. The applications of electrostatic generators were found in several areas such as X-ray tubes [1], preservation of food products [2], nuclear physics [3], and physics research [4].

The conventional electrostatic generator converts mechanical work to electric energy, i.e. high voltage. A lot of electrostatic generators had been built such as the Wimshurst machine [5], the Holtz Electrostatic Influence Machine [6], and the Van De Graaff electrostatic generator, which was a well-known electrostatic generator back in the early 20th century [7]. Van De Graaff is an American physicist [8] who invented an electrostatic generator which generated a very high voltage. Fig. 1 shows a Van De Graaff machine that generates high voltage. An insulating belt that carries charges connects the bottom and top pulley. Electrostatic charges are generated through rubbing and the positive charges are transferred via the belt to the top collector (globe).

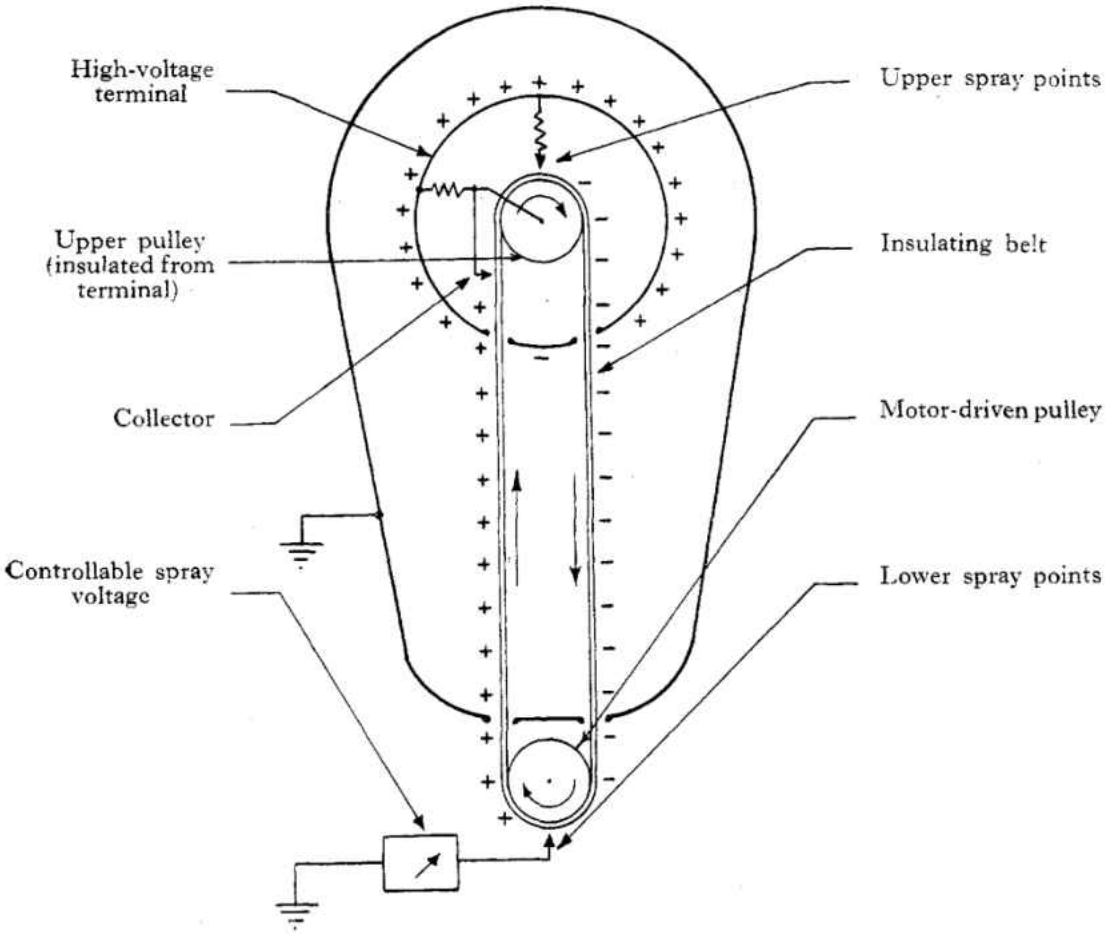

Fig. 1. Conventional Van De Graaff electrostatic generator [8].

Another terminology that has been widely used for contact electrification is the triboelectric effect, which happens with the friction of two distinct materials [9-11]. Charge generation based on the triboelectric effect can also be achieved through a contact-separation process [12]. Yang *et al*. [13] used two types of the triboelectric models, i.e. contact-separation (Fig. 2.a) and sliding model (Fig. 2.b), to generate electrical power. In both cases, Polytetrafluoroethylene (PTFE) was used to either rub against or contact-separate with an aluminum surface. Charges were collected by a copper surface through induction.

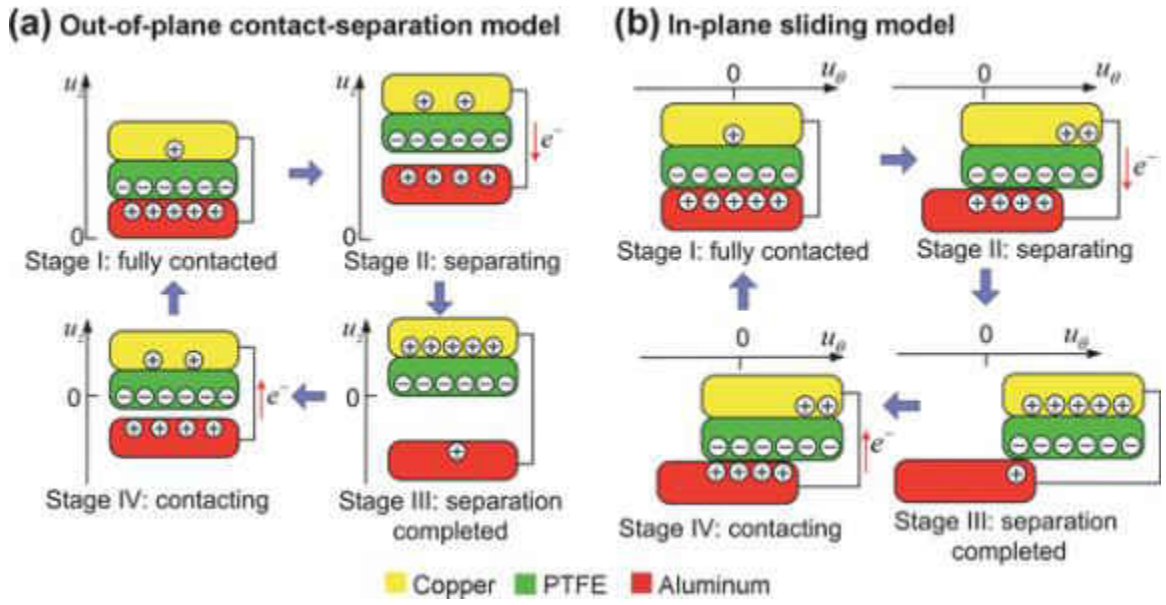

Fig. 2. The principle of the triboelectric generator [13].

Another electrostatic generator is the Kelvin water dropper, which was invented by William Thomson (Lord Kelvin) [14] from Glasgow University in 1867. The Kelvin water dropper was considered as a self-acting generator, as shown in Fig. 3, which generates high voltage output just by dripping water. It converts gravitational potential energy into electrical energy.

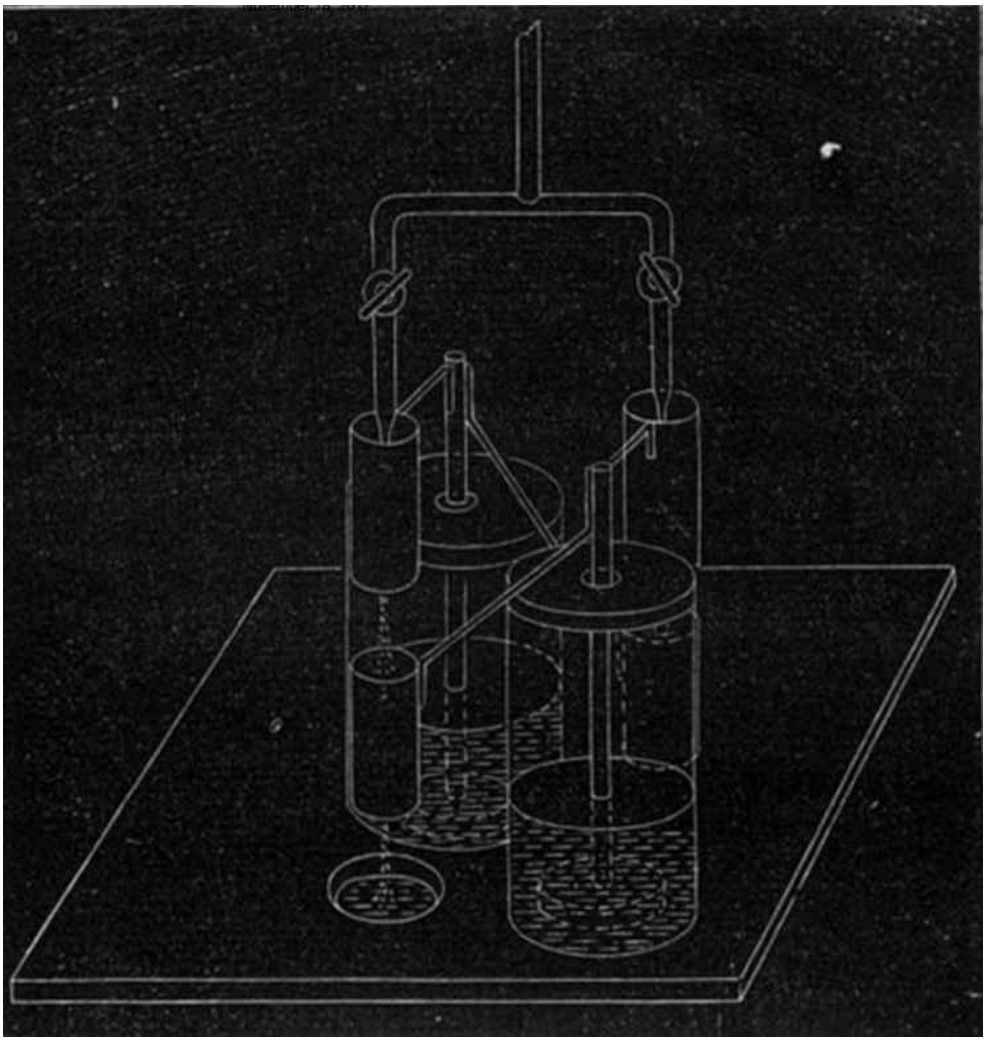

Fig. 3. The first Kelvin water dropper [14].

In his original setup, Kelvin used a water jet with five outlet flows, which passed a metal inductor vertically and were dripped into the funnel (receiver), as shown in Fig. 4. The receiver was insulated by ambient air very well. To keep the charges during or after an experiment, Kelvin designed a glass jar of sulfuric acid, as shown in Fig. 5, and a metal tube was fixed inside the jar and connected to the inductors. Additionally, the lead on the glass jar was not connected to the metal tube due to the discharge of the charges.

Fig. 4. The location of the water jet and inductor and reserves [14].

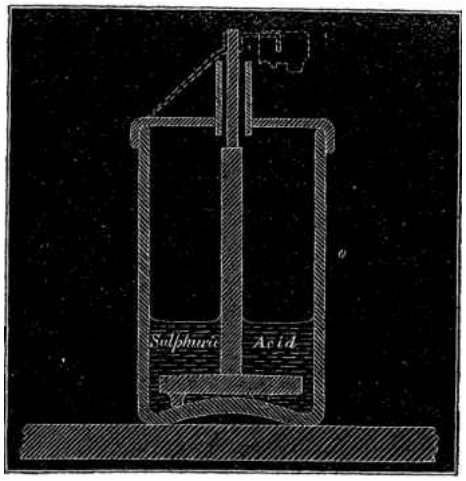

Fig. 5. Charge keeper for Kelvin water dropper [14].

It is important to know about the physics of charges inside the water droplet in the air. Also, many have investigated the weather to understand the concept of the charges in the air based on physics of the Kelvin water dropper. Chree [15] studied the atmospheric electric potential according to his data that were achieved from a Kelvin water dropper electrograph over a period of two years. He used a Kelvin portable electrometer to measure the voltage. As a result, he introduced a factor that showed potential gradient with the unit of volts per meter height. The

amount of factors changed considerably during the time of the day. The voltage changed considerably during 4am to 6am, and between 10am to 10pm it did not give a constant voltage. During the summer (between June to September) and the winter (November to February), the voltage had the highest and lowest value.

Chree *et al.* [16] found the reason that he could not have the stable voltage during the time of the day by the device. There were the several reasons such as freezing the storage water tank, humidity of the ambient air, chocking of the jet, spider, and metrological conditions. Thus, they replaced a radioactive substrate instead of the water jet. Sanford [17] reported the water could be positive while the water contacted with a substrate. In addition, moisture in the air causes the air to have a positive charge. Moreover, Elster and Geitel [18] reported that the charges at a waterfall at the height of 500 meters above the waterfall were negative. Additionally, in the domain of the waterfall where water was sprayed, the charges were mostly negative electrification. The smaller distilled water droplet, which was sprayed vertically, had a more negative charge than positive charge. A small water droplet raised up compared to the big droplet then fell down. Flowing air or gravity on small droplets might lead them to be separated from the larger electropositive drops.

Harrison [19] used a Kelvin water dropper electrograph device for measuring atmospheric electric circuits over a long term. Pollack [20] used the experiment of Kelvin water dropper in a laboratory to model the atmospheric electrical circuit and also explained the atmospheric physics by this device. On a sunny day, the negative charge is always close to the surface of the ground and the positive charges are close to that. As shown in Fig. 6, with an extremely positive charge from the cloud, with the ionosphere created with hot dense plasma gases ions, this unbound charges led to the presence of thunder with highly negative charge[21].

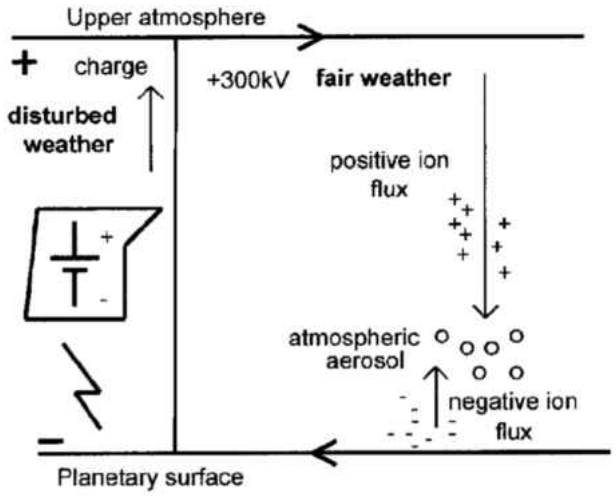

Fig. 6. The schematic of the atmospheric electrical circuit[21].

King [22] modeled that the accumulation of the positive charge by solar wind in ionosphere caused the positive charges to transfer to our atmosphere by cosmic rays. There are several unbalanced charges in the atmosphere as shown in Fig. 7. However, as mentioned before, on the surface of the earth, the charge is negative. While the positive charge in the cloud and negative charge on the earth has a suitable condition, the discharge will happen in the form of thunder.

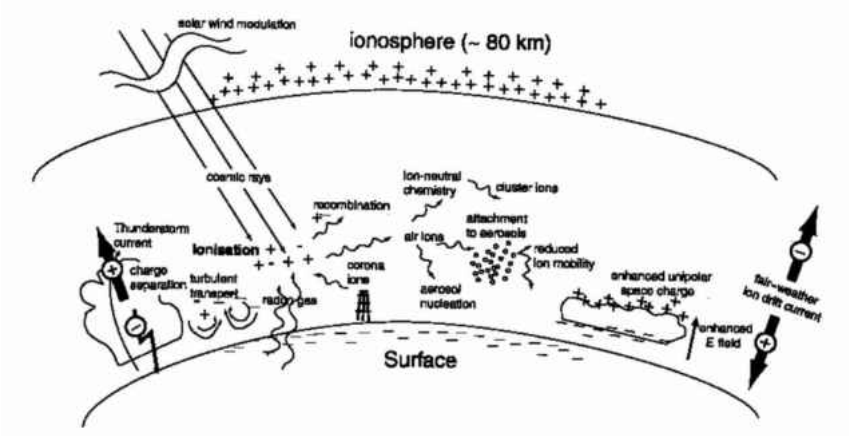

Fig. 7. Discharging charge in the global electrical circuit [22].

Loeb [23] reported that in ambient air, the amount of the positive or negative ions accounted between 1000 and 10000 ions per Cm^3 at the normal condition. As an example, at the condition of 60% relative humidity and at the temperature of 20° C, dry wood with the length of 1m and 1cm discharged a clock type electrostatic voltmeter in the tens of seconds. He also reported that the ionization in the air increased by the use of flames and exhausts from the chemical and industrial process.

Several teachers used a Kelvin water dropper for educational purposes. In 1977, two teachers, Evans and Stevens [24], demonstrated a simple and low cost method by using wasted cans as inductors, which is the same concept of the conventional Kelvin water dropper as shown in Fig. 8. Michael Sady [25] used a Kelvin water dropper for teaching the electrostatic generator in the class for an elementary school to demonstrate how it worked and illustrated to the student the attraction and repelling in electrostatic charge. They added two bottom cans with great insulation and a hole on the bottom of the cans. This structure caused the water to exit from the bottom cans, then the charges were gained from the droplets, but the outlet water was extracted in another wasted water dish.

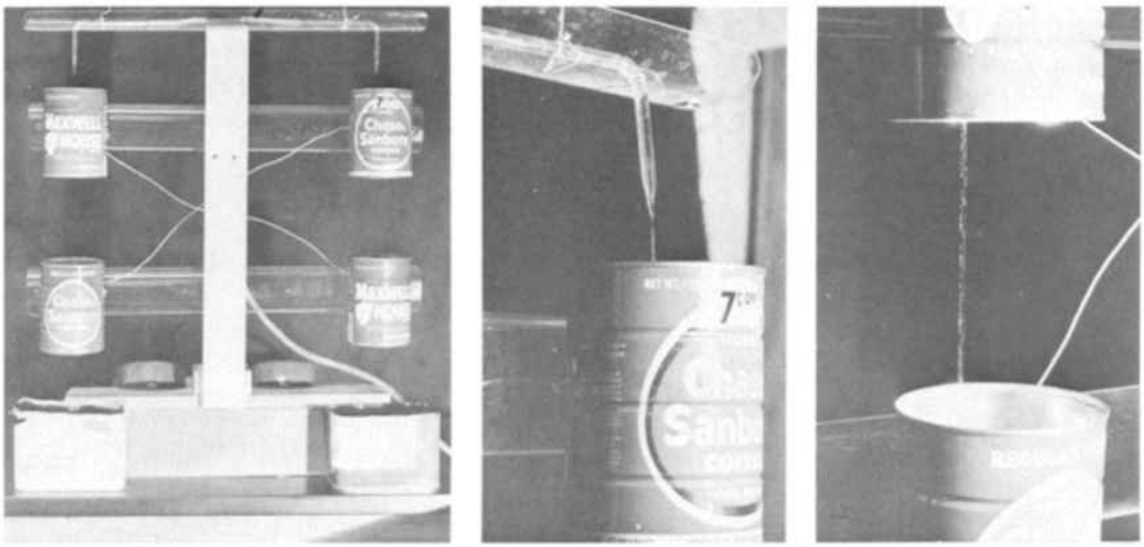

Fig. 8. Kelvin water dropper designed by Evans and JT Stevens [24].

In 1971, Euerle, William C. [26] invented a polyphase AC electrostatic generator configuration. They explained the polyphase generator in different devices such as a cylindrical electrostatic generator (Fig. 9), Van der Graaff generator (Fig. 10), and Kelvin water dropper. By adding N cans in the Kelvin Water dropper, there would be a possibility to increase the phase in the Kelvin water dropper. Each of the connections should be like a positive feedback loop.

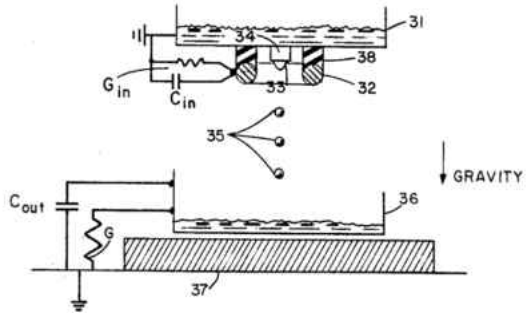

Fig. 9. Cylindrical electrostatic generator [26].

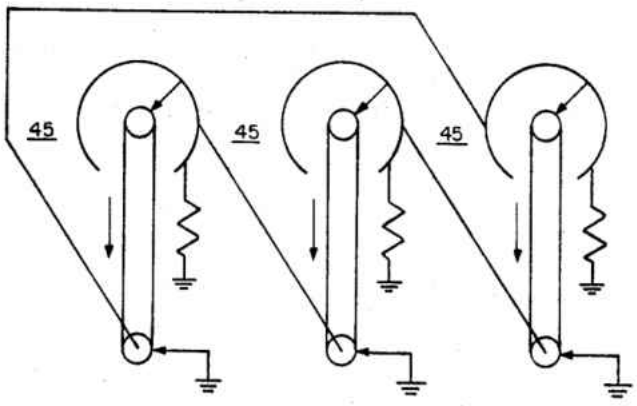

Fig. 10. Three phases Van de Graaff generator [26].

Zahn [27] investigated the self-existed generator by water that generated AC high voltage. He used the series water droplet and the connection was the same as Fig. 11.

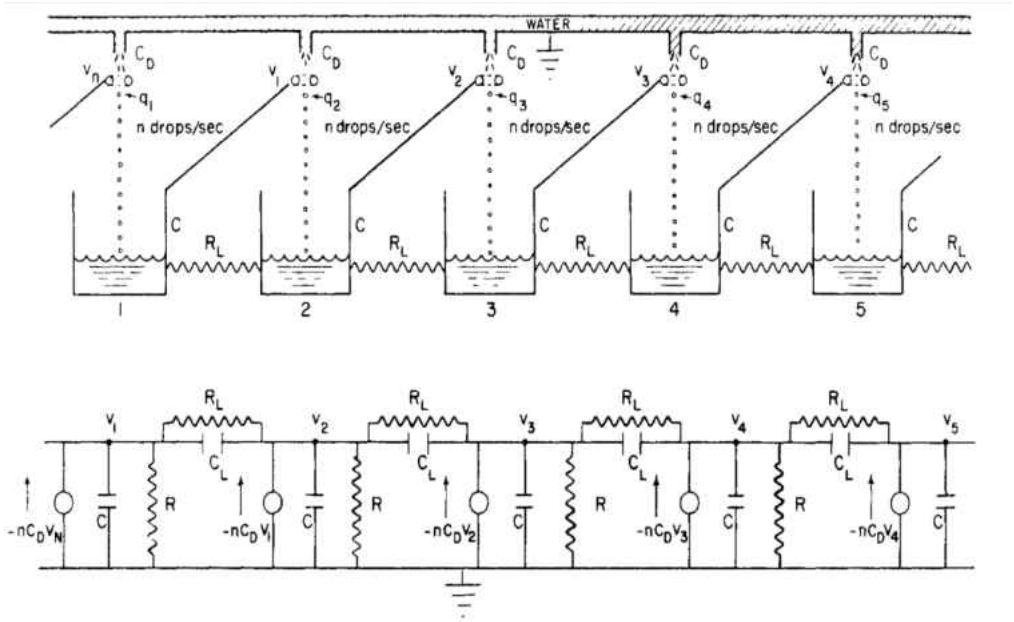

Fig. 11. The tube connection of Kelvin water droplet and the electrical circuit [27].

He considered n as the number of the droplet and simplified the electrical circuit; thus, the voltage could be written as follows:

$$V_i = \frac{R}{(RC\omega + 1)}\left[-nC_D V_{i-1} + \frac{(V_{i-1} - V_i)(R_L C_L \omega + 1)}{R_L} - \frac{(V_i - V_{i+1})(R_L C_L \omega + 1)}{R_L}\right] \quad (1)$$

where V_i, R, C, C_D, R_L, C_L, and ω represent absolute voltage from the collector, leakage resistance ground, the capacitance between the ring and the water droplet, leakage resistance between cans, capacitance between adjacent cans plus the capacitance of a load, and natural frequency, respectively. As shown in Fig. 12, four different cans were used to create DC or AC voltage with several types of phases, for which the frequency of the system can be measured by:

$$\omega_0 = n\frac{C_D}{C} sin(\frac{\pi}{N}) \quad (2)$$

where N is the number of cans.

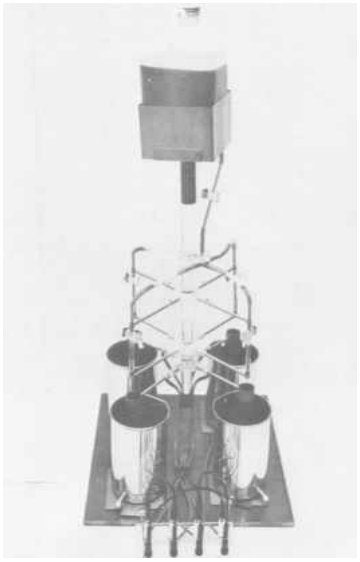

Fig. 12. A Kelvin Water Dropper with the polyphaser ability [27].

In 2000, G Planinšič and T Prosen [28] studied experimentally and numerically on optimizing the Kelvin water dropper. To model the theory, they assumed that both sides of the water droplets had the same number and opposite charges. They considered that two cases including two rings had a constant charge and were connected to a constant potential. In case one, as shown in Fig. 13, the water droplet with the charge density of $\sigma_s(z)$ and charge of q_0 had the distance of radius a. The measurements ρ, p and L are the thickness of the ring wire, the radius of the rod, and length of the rod.

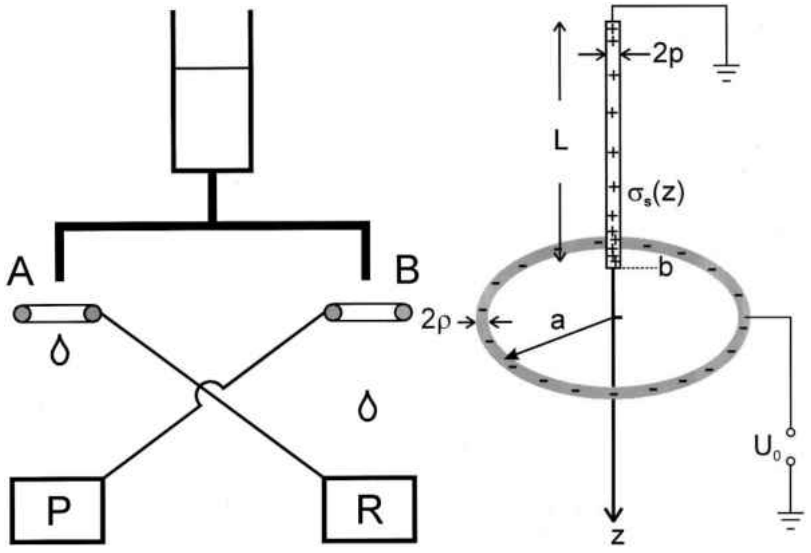

Fig. 13. Kelvin water droplet and the charge description distribution on the rings [28].

the electric field E_0 in the ring can be expressed as follows:

$$E_0(z) = \frac{\sigma_0 z a^2}{4\varepsilon_0 (z^2 + a^2)^{3/2}} \tag{3}$$

where a, z, ε_0 are the radius of the ring, axis, and permittivity, respectively. The maximum amount of $E_0(z)$ is $\sqrt{2}a$, and z is the axis. The amount of charge density was expressed as follows:

$$\sigma_0 = \frac{q_0}{\pi a^2} \tag{4}$$

where q_0 is a charge. They reported that total voltage from the system is:

$$U_{\text{total}}(u) = \frac{\sigma_0 a}{4\varepsilon_0(1+u^2)^{1/2}} + \int_{\beta-\lambda}^{\beta} \frac{a\,\sigma_s(u')\eta\,du'}{2\varepsilon_0(\eta^2+(u-u')^2)^{1/2}} \tag{5}$$

where $u = \frac{z}{a}$ and $\beta = \frac{b}{a}$, $\lambda = \frac{L}{a}$, $\eta = \frac{P}{a}$ (Fig. 13) while the rod is grounded $U_{\text{total}}(u) = 0$, and the right side of the equation can be approximated as follows:

$$\int_{\beta-\lambda}^{\beta} \frac{\sigma_s(u')\eta\,du'}{(\eta^2+(u-u')^2)^{1/2}} \approx \frac{\sigma_0}{2(1+u^2)^{1/2}} \tag{6}$$

where $\beta - \lambda \le u \le \beta$. The surface charge density on the rod can be written:

$$\sigma_s(x) = \frac{\sigma_0}{2\eta}\left[(1+(\beta-\lambda+\lambda x)^2)^{1/2} \times ln\left(\frac{x-1+((\eta/\lambda)^2+(x-1)^2)^{1/2}}{x+((\eta/\lambda)^2+x^2)^{1/2}}\right)\right]^{-1} \tag{7}$$

$$x = \frac{z-(b-L)}{L} = \frac{u-(\beta-\lambda)}{\lambda},\ 0 \le x \le 1$$

The total electric field contains the summation of the electric field in the ring ($E_{r,ring}$) and rod ($E_{r,rod}$)

$$E_{r,ring}(r') = \frac{q_0(\beta)}{4\pi^2\varepsilon_0 a^2}\int_0^{\pi} \frac{(r'-cos\varphi)d\varphi}{((r'-cos\varphi)^2+sin^2\varphi)^{3/2}} \tag{8}$$

where φ will change between from π to 0 and $r' = r/a$. Also, the electric field for the rod is equal:

$$E_{r,rod}(r') = \frac{\eta}{4\varepsilon_0}\int_{\beta-\lambda}^{\beta} \frac{r'\sigma_s(u)du}{(r'^2+\mathrm{u}^2)^{3/2}} \tag{9}$$

where ν is equal to ρ/a. The amount of U_0 can be calculated:

$$U_0 = \frac{q_0(\beta)}{4\pi^2\varepsilon_0 a^2}\int_0^{\pi} \frac{d\varphi}{((1+\nu-cos\varphi)^2+sin^2\varphi)^{1/2}} + \frac{\eta}{4\varepsilon_0}\int_{\beta-\lambda}^{\beta} \frac{\sigma_s(u)du}{((1+\nu)^2+\mathrm{u}^2)^{1/2}} \tag{10}$$

For the experiments that they carried out , the ring radius was much lower than the radius of the ring. Thus, the integral can be regenerated as the following:

$$\mathrm{H}(\nu) = \int_0^{\pi} \frac{d\varphi}{((1+\nu)^2 + +1 - (1+\nu)\cos\varphi)^{1/2}} = \frac{2}{\nu} K\left[\frac{-4}{\nu^2}(1+\nu)\right] \tag{11}$$

K denotes elliptic integral of the first kind. The measurement of ν should be much smaller than 1, and $\mathrm{H}(\nu)$ is estimated by $\ln(8/\nu)$ [29]. Finally, the last governing equation is expressed as the below form:

$$U_0 = \frac{q_0(\beta)}{4\pi^2\varepsilon_0 a^2}\mathrm{H}(\nu) + \frac{a\eta}{4\varepsilon_0}\int_{\beta-\lambda}^{\beta} \frac{\sigma_s(u)du}{(1+\mathrm{u}^2)^{1/2}} \tag{12}$$

The amount of $\sigma_s(u)$ can be detected in the following form:

$$\sigma_s(u) = \tilde{\sigma}_s(u)\sigma_0(\beta) \tag{13}$$

where $\tilde{\sigma}_s(u)$ is the unity charge density. Thus the amount of $\sigma_s(u_j)$ can be indicated as:

$$\sigma_s(u_j) = \tilde{\sigma}_s(u)\frac{2\varepsilon_0 U_0}{a}\left[\frac{\mathrm{H}(\varepsilon)}{2\pi} + \eta\lambda\sum_{i=1}^{N}\frac{\tilde{\sigma}_s(u_i)du}{(\mathrm{N}-1)(1+(\beta-\lambda\frac{i-1}{N-1})^2)^{1/2}}\right]^{-1} \tag{14}$$

In the experiment, they used a setup of a Kelvin water dropper as shown in Fig. 14. A rod at the end of the water reservoir was connected and passed through the ring, then the oscilloscope sensor was fabricated after the droplets of the Kelvin water dropper.

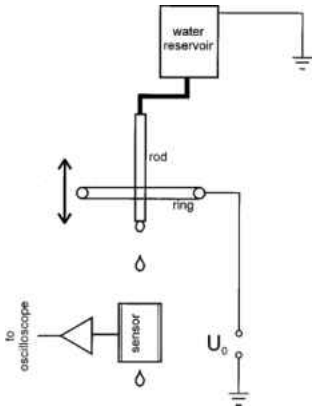

Fig. 14. Kelvin water dropper device setup [28].

The comparison between the experimental and simulation result showed that the charge distribution at the center of the ring and end of the rod had the higher amount. Thus, the performance of the Kelvin water dropper increased while water droplet output was at the center of the ring; the lower diameter of the ring, and diameter size of the tube.

Due to the complexity of charged droplet, Frohn and Roth [30] discussed the charged droplets. The droplet includes ions inside and charge carriers before atomization. Hence, the spray the water was affected by the charge distribution of the droplet. A spark even occurred while droplets carried a high amount of charge. They reported that by increasing the charge droplets, the droplet became unstable. As shown in Fig. 15, two nuzzles (N_1 and N_2) were fixed to the reservoir which was connected to the earth electrically. Two ring electrodes $R_1$and R_2 were connected to collectors $C_1$and C_2 which are electrically insulated. The droplet could be accounted as a spherical capacitance of $4\pi\varepsilon_0 r$ with the amount of permittivity of vacuum of $\varepsilon_0 = 8.842 \times 10^{-12}$Coulomb $Volt^{-1}m^{-1}$. The electrostatic amount corresponding to the charge Q was calculated by [30]:

$$E=\frac{Q^2}{2C} = \frac{Q^2}{8\pi\varepsilon_0 r} \quad (15)$$

and the total energy of the droplet could be calculated by [30]:

$$W_{tot} = \frac{Q^2}{8\pi\varepsilon_0 r} + 8\pi\sigma r^2 \tag{16}$$

The lowest amount of the W_{tot} could be obtained at the radius called Rayleigh radius.

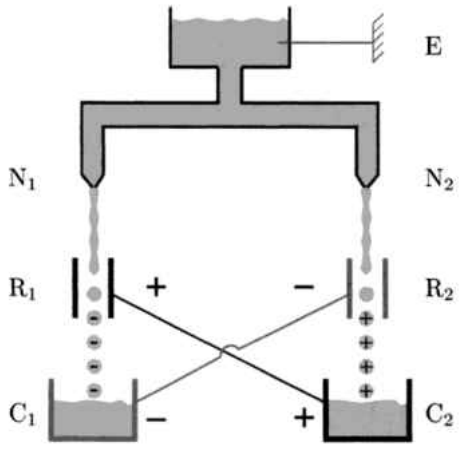

Fig. 15. Schematic of a Kelvin water dropper [30]

$$r = r_{Ray} = \sqrt[3]{\frac{Q^2}{64\,\sigma\varepsilon_0 r}} \tag{17}$$

The amount of charge and total energy in Rayleigh radius was calculated as follows:

$$Q_{Ray} = 8\pi\sqrt{\sigma\varepsilon_0 r^3} \tag{18}$$

$$W_{ges,Ray} = 12\pi\sigma r^2 \tag{19}$$

The charged particle with the velocity of ν in the electric field of E can move with the mobility of b, which the relation could be indicated by:

$$b = \frac{\nu}{E} \tag{20}$$

and the Stokes law could be expressed as the following:

$$Q = \frac{6\pi\eta r v}{E} \tag{21}$$

by substituting equation(21) into equation (20), the new equation was written:

$$b = \frac{Q}{6\pi\eta r} \tag{22}$$

The maximum mobility required for the Rayleigh limit was the same as equation (18). Hence, the mobility could be rewritten as follows:

$$b_{Ray} = \frac{4\sqrt{\sigma\varepsilon_0 r}}{3\eta} \tag{23}$$

The amount of the ratio of charge to mass is an important parameter due to the acceleration and manipulation that happens in a charged droplet under electrostatic fields. Thus, in Rayleigh limit, the ratio is:

$$(\frac{Q}{m})_{Ray} = \frac{6\sqrt{\varepsilon_0\sigma}}{\varrho r^3} \tag{24}$$

The evaporation could not affect the charged droplets while the Rayleigh limit occurred.

Ovchinnikova [31] discussed the possibility of water to store the charges. To demonstrate this issue, they reported that a Kelvin water dropper could be a manifestation in which the charges could maintain each body of pure water. Garg *et al.*[32] built up a conventional Kelvin water dropper in Fig. 16 and measured charges by a novel method called Effective Capacitance method.

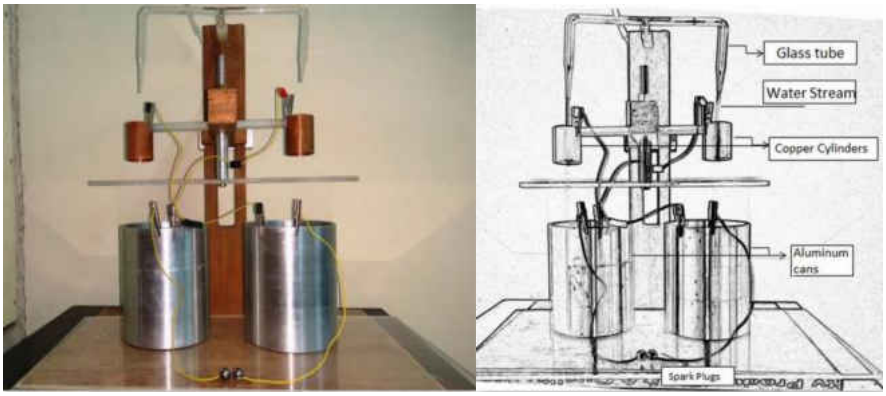

Fig. 16. Experimental setup of a conventional Kelvin water dropper [32].

They use two types of spherical and cylindrical spark plugs (Fig. 17) measured the distance between the plugs and the time of each spark and introduced a linear and quadratic curve fitting equations for the figure of time versus distance of the plugs as following:

$$y = 0.7095x + 1.6504 \quad (25)$$

$$y = 0.0481x^2 + 0.3546x + 2.0833 \quad (26)$$

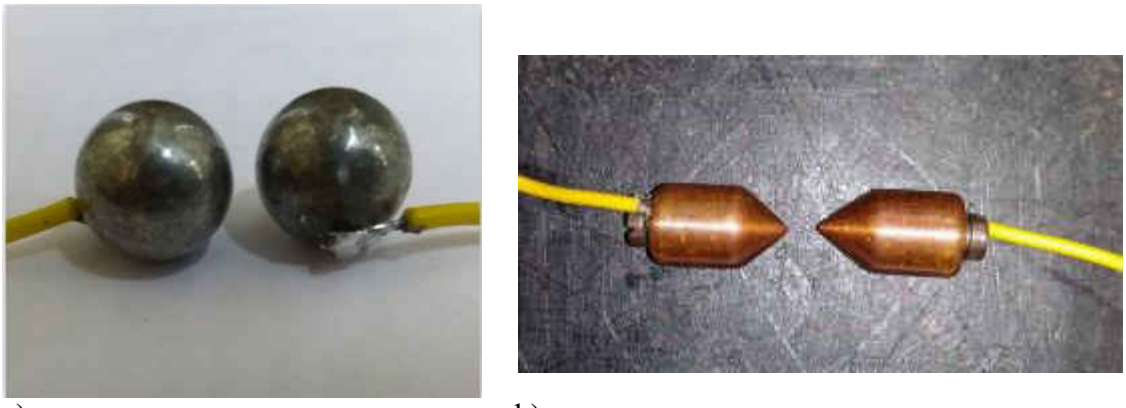

a) b)

Fig. 17. a) spherical metal spark plug b) cylindrical metal spark plug [32]

The effective capacitance in the device contains the summation of capacitance in an aluminum can connecting wires, spark plugs.

$$C_{effective} = C_{can} + C_{wire} + C_{sp} \tag{27}$$

the amount of C_{wire} and C_{can} are negligible to compared with C_{sp}. Hence,

$$C_{effective} \approx C_{sp} \tag{28}$$

$$Q_{ac} = C_{sp}V \tag{29}$$

$$Q_{ac} = C_{sp}E_{air}d \tag{30}$$

where E_{air}, d, and Q_{ac} are electric filed, the distance between the plugs, and charge. They mentioned that the Q_{ac} had equivalence with d. They introduced this device as a great choice for a toy device to explain the charge for educational purposes.

Jonas and Steel [33] detected that a way to prevent any damage to bystanders or persons who are using the nuzzle to extinguish fires is to get rid of any electrostatic shock while the person is using a nuzzle; special nuzzles were designed based on the Kelvin water dropper generator to omit the shock.

The ambient air has a positive ion that is not healthy for the human body [34-36]. Liu *et al.* [34] utilized the Kelvin dropper for the wireless antenna to naturalize the positive charge in the air and also generate a voltage by this method. Fig. 18 refers to ions from the air taught to the aluminum surface. UV light was exposed to the top dielectric and made surface electromagnetic waves and surface Plasmon polarities. These processes expand in a metal and a dielectric. Due to the nature of the aluminum sheet, it was able to capture ultraviolet lights due to the surface plasmatic vibration frequency at the ultraviolet band.

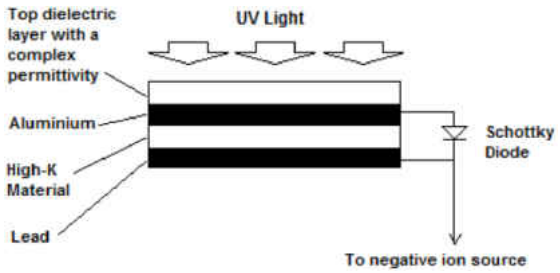

Fig. 18. The schematic of UV antenna [34].

To naturalize the pollutant from the air, the negative side of the Kelvin water dropper was connected to the UV antenna as shown in Fig. 19. This system generated 0.55 V and 0.42 V while the UV light exposed to the surface of the antenna and without light exposure respectively.

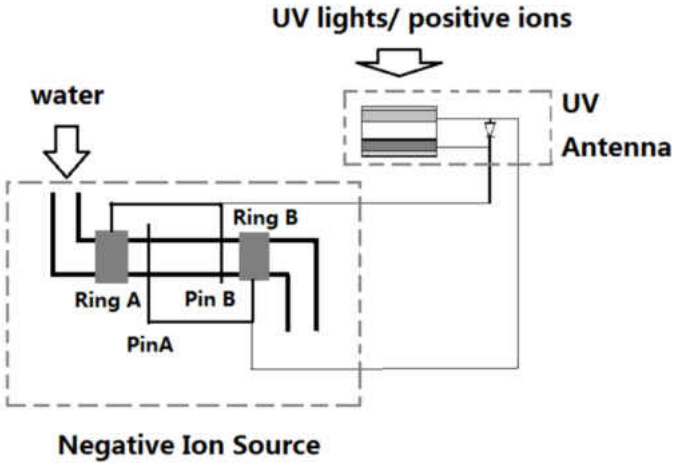

Fig. 19. The schematic of linking Kelvin water dropper with UV antenna [34].

Huang [37] investigated the common Kelvin water dropper as shown in Fig. 20.a. He used two beakers as collectors, water droplet inside the inductor rings, and connection of positive loops between collectors and rings. He modeled the electric circuit of Kelvin water dropper in Fig. 20.b;

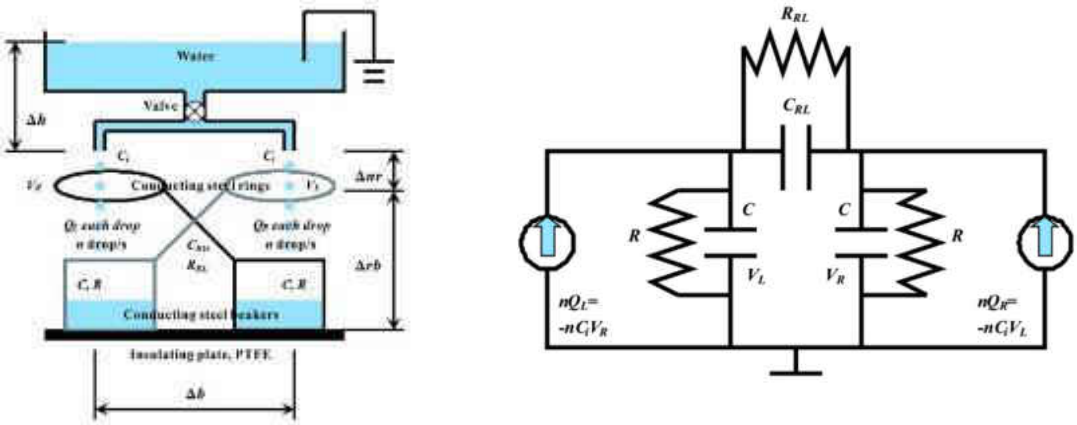

a) b)

c)

Fig. 20. (a) The diagram of the Kelvin Dropper setup b) Electrical circuit of the Kelvin Dropper c) Experimental setup[37]

Then, he simplified the circuit so that the amount of voltage difference could be expressed as follows [38,39]:

$$\Delta V(t) \equiv |V_L - V_R| = 2 * V_0 \exp\left\{\left[\frac{-\left(\frac{2}{R_{RL}}\right) - \left(\frac{1}{R}\right) + nC_i}{C + 2 * C_{RL}}\right] * t\right\} \quad (31)$$

$$C = \frac{\oint_A \varepsilon \bar{E}.d\bar{A}}{\int_l \varepsilon \bar{E}\, d\bar{l}} \alpha \frac{A}{l} \quad (32)$$

where V_0, R_{RL}, C_{RL}, C, A, l, $\bar{E}$, and ε denote constants (based on the initial condition of the droplet generator and the Nth beaker), left and right beakers resistances, left and right beakers capacitance, characteristic capacitance, surface area, the separation distance of interest, and the constant magnitude of the electric field between the arbitrary two bodies, and electric permittivity, respectively. He reported that the charge place depends on the different geometries and the dimensions of the device. They measured higher voltage while higher water flow rates, closer induction rings to the water outlets, and larger rings were carried out.

Eijkel *et al.*[40] built up a device to convert a ballistic energy conversion to generate an electrostatic voltage as shown in Fig. 21.a. The water was pressurized and passed a ring and taught the target.

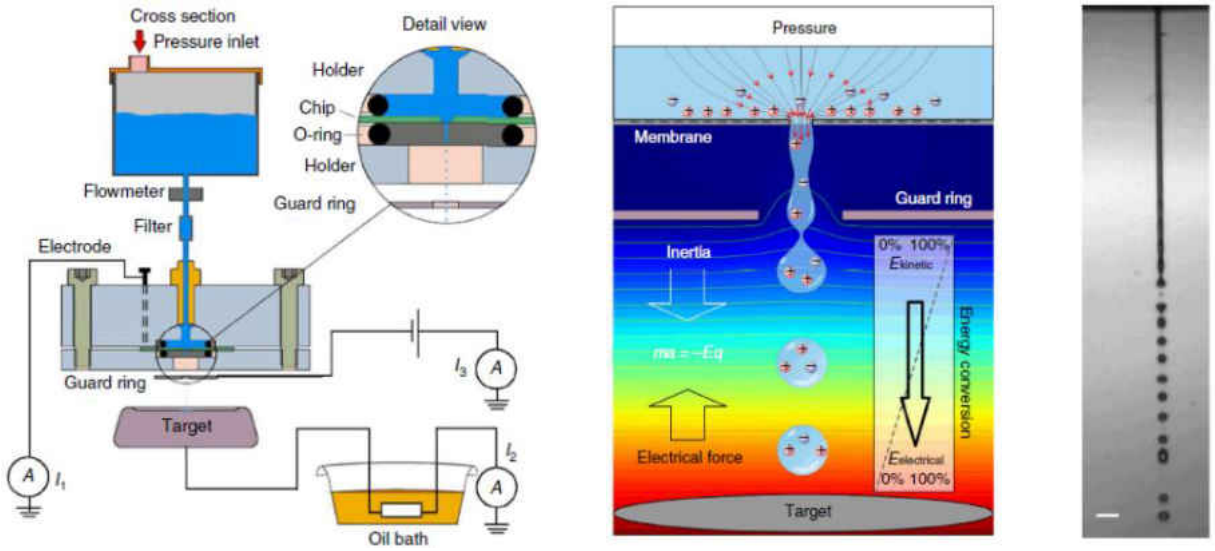

a) b) c)

Fig. 21. a) Experimental setup; b) schematic diagram of the energy conversion c) photomicrograph of the microjet [40]

Regarding the force balance in Fig. 21.b, the force balance was calculated by:

$$m_d g + q_d E + m_d a + F_{fr,d} = 0 \tag{33}$$

where m_d, g, q_d, E, a, and $F_{fr,d}$ represented the droplet mass, the gravity, the droplet charge, the electrical field, the inertial acceleration, and the frictional force of the air on the droplet, respectively. By considering the droplet did not have friction on the channel and flow with a constant velocity, the terms of $m_d a$ and $F_{fr,d}$ were negligible. Hence, amount of energy per droplet could be calculated as follows:

$$W_{d,grav} = q_d U = m_d g h' \tag{34}$$

where h and U were the maximal falling height and the target voltage. As shown in Fig. 22, Rayleigh' limit equation, the charge of droplet could be calculated:

$$q_d = 8\pi(\varepsilon_0 \gamma)^{0.5} a^{1.5} \tag{35}$$

where ε_0, γ, a were represented the permittivity of vacuum, the surface tension, and the droplet radius.

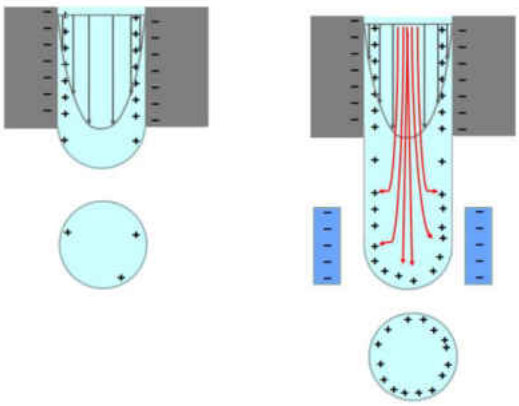

Fig. 22. Charge configuration in charge of the water droplet left) without external induction gate electrode; right) with external induction gate electrode [40].

The volume of the droplet was 50 µl with the radius of 2.3 mm; also, the maximum voltage was 20 kV that the droplet size could be measured by use of equation (35) and gravitational energy as follows:

$$\frac{q_d}{m_d} = \frac{6}{\rho g}\frac{(\varepsilon_0 \gamma)^{0.5}}{a^{1.5}} \tag{36}$$

By this experiment, the efficiency of the system was obtained at 48% at operating voltage of 20 kV whereas the theory prediction was more than 90% at the voltage of less than 100 V.

Thijs Knapen [41] has studied that this device has several components of tubes, induction rings, collectors, and electrical connections. As shown in Fig. 23, the physical mechanism of the device was that the DI water as a working fluid flowed on two different tubes. Then, they passed through two ring inducts; the charges were placed in the device as shown in Fig. 23.a. The induction rings were connected to the collectors created a loop, which is called a positive feedback loop. Ions of OH^- and H^+ can be separated from each other in the collectors and generate a high voltage. In other words, by the configuration of positive feedback loops in the system, the inductance could separate different charges in the device, then the charges are collected by two collectors. When the water flows more in this device, more positive and negative charges are placed on the collectors.

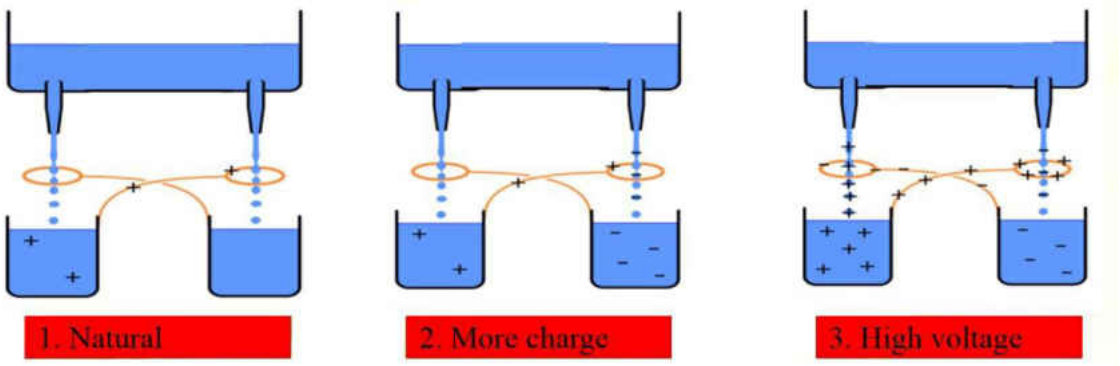

a) b) C

Fig. 23. The configuration of the Kelvin Water Dropper a) Natural situation of the system b) charges are starting to be created [41].

Abdil Ozdemir [5] used a spray (0.15– 15 μL min-1) and gas pressures (0–150 psi) on to the two double layered metal to separate them, with the configuration of the positive feedback loop as shown in Fig. 24. They measured a high voltage of 4 kV by separation of the ions from this device. By this method, ionization of molecules can be used for applications of spectrometry.

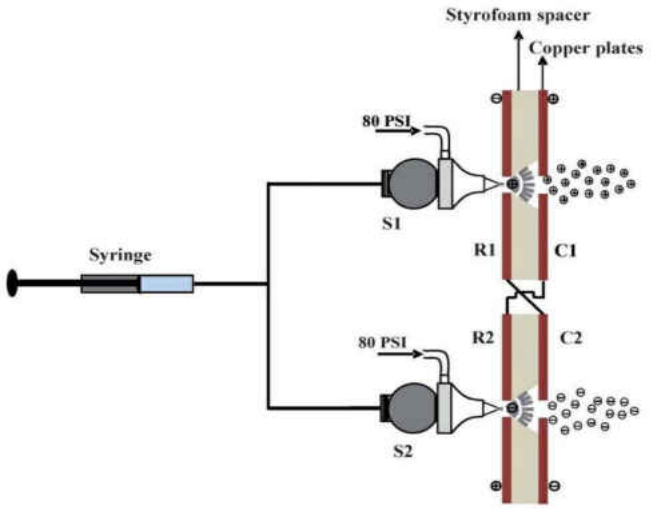

Fig. 24. Kelvin spray ionization source schematic[5].

The problems of the MKWD to generate high voltage included discharging charges in the device, discharging by humidity, controlling the device in high voltage, and the microchannel for the system. Álvaro G. Marín *et al.* [42] designed a Kelvin water dropper device which studied oil and water in microscale as shown in Fig. 25. The oil injection plays the role of air in conventional Kelvin water dropper. The water has a droplet shape after the ring by means of oil injection. The droplet after the ring did allow transfer of the charges from the flow before the ring.

Fig. 25. Schematic of the microfluidic Kelvin water dropper[42].

Yanbo Xie [2] reported that a ballistic Kelvin's water dropper as shown in Fig. 26 has low power with a high voltage and low current with low frequency.

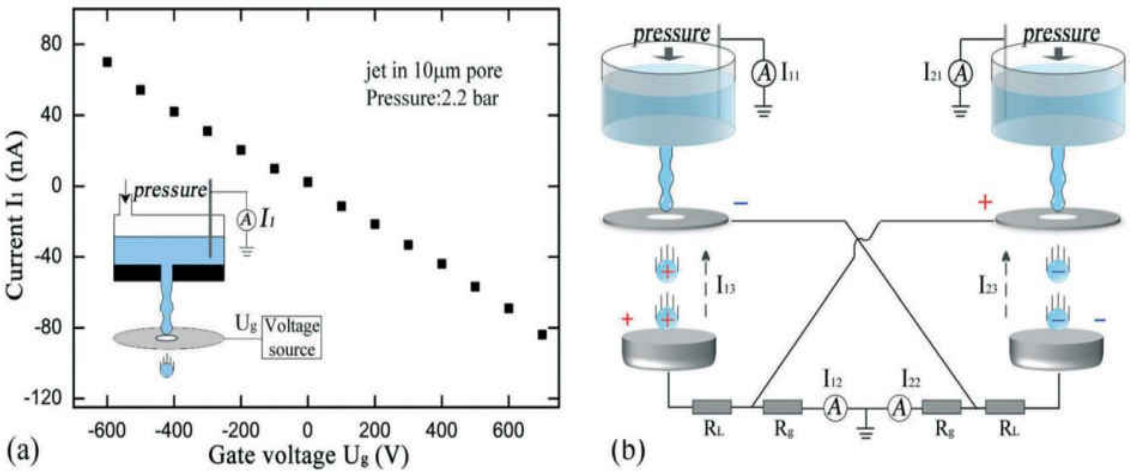

Fig. 26. a) Current by gate induction b) self-excited ballistic energy system [2]

In addition, the other application for the microfluidic water Kelvin dropper can be addressed by flow cytometry [43], electrostatic charging [3], and electrophoresis [44,45]. Regarding the limitation of the system, electrowetting can be selected as an application of MKWD; this is discussed further in the next section.

For most proposed Kelvin water droppers, the output power is quite low. Thus, Kelvin water dropper output power has high voltage with low current. In the present project, it is important to choose a specific application for MKWD due to high voltage with low current**.** The purpose of the present project is to generate high voltage by means of the water and air as working fluids in a microfluidic Kelvin water dropper. Due to the output of MKWD having low current and high voltage, one of the applications for the MKWD can be addressed by electrowetting. To further explore Kelvin water droppers in small-scale applications, researchers have investigated the control parameters that can improve the performance of MKWDs. An important application using the ultra-high voltage produced by MKWDs is electrowetting.

1.2 Contact Electrowetting

Electrowetting has been an interest for microfluidic devices as a means of the controlling the shape of the droplet by electrical signal [46-49]. In 1875, Gabriel Lipmann [50] for the first time achieved electrocapillarity. Several researchers had tried to improve this technique for liquid actuation in smaller scale [51,52] to build a micromachine [48]. Electrowetting is a technique used to manipulate the wetting properties of a substrate under an external electric field. A typical electrowetting device can make a water droplet deform on the top of a substrate. The device consists of a metal substrate, dielectric, electrode, and the top electrode. The metal substrate is coated by a dielectric. The water droplet is on the top of the dielectric; on the top of the water droplet is an electrode [53-55].

Mugele [56] discussed accumulation of charges at the right corner of the droplet under the electric field that leads to an increase in the wettability of the substrate as shown in Fig. 27. The shape of a droplet on a surface can be controlled by manipulating the electric field strength going across it, resulting in various extents of surface wetting.

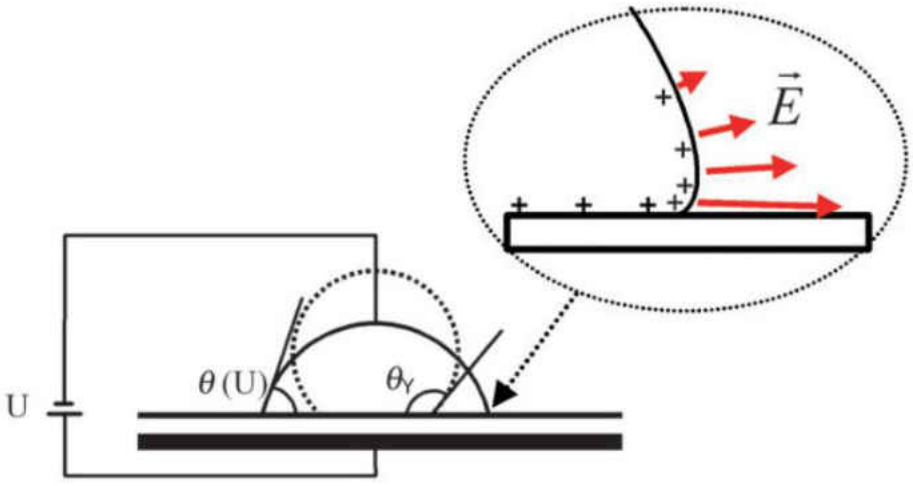

Fig. 27 .Schematic of electrowetting and water deformation [56].

Caputo [57] explained conventional electrowetting, which contains several components such as a dielectric layer, electrode, and substrate. As shown in Fig. 28, on the substrate, one electrode, which is coated by a dielectric layer, is attached. In the natural situation (not applying a voltage to the droplet), three surfaces were exited including surface tension solid-liquid, solid-gas, and liquid-gas. By applying the voltage, the amount of the tension solid-liquid was affected by the electric field. Hence, the contact angle changed while tension changed.

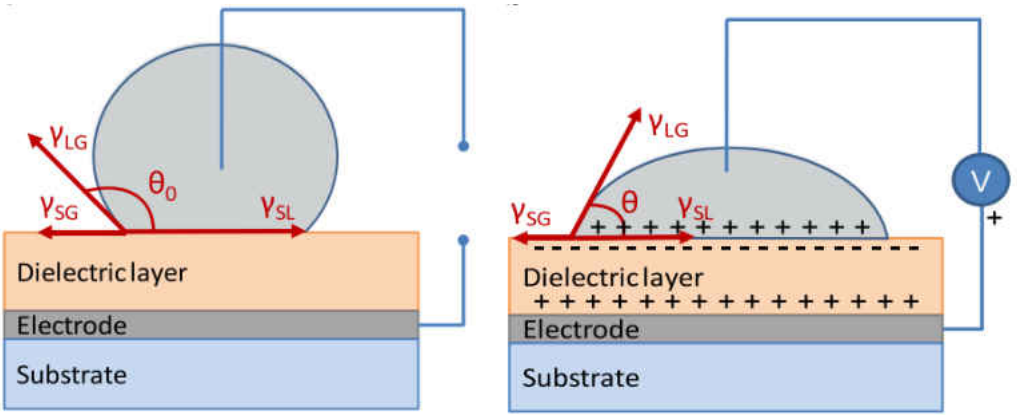

Fig. 28. The schematic of the components of the electrowetting before and after applying voltage [57].

Electrowetting has been widely used in lab-on-a-chip devices for biomedical analysis and diagnostics [58]; droplets could manipulate on a sample chip and it could be used for tissue engineering, airborne chemical detection, clinical diagnostics, and gene sequencing. The droplet is sandwiched between the Teflon AF; the two electrode materials on the top and bottom are shown in

Fig. 29. By applying the voltage, the droplet can actuate.

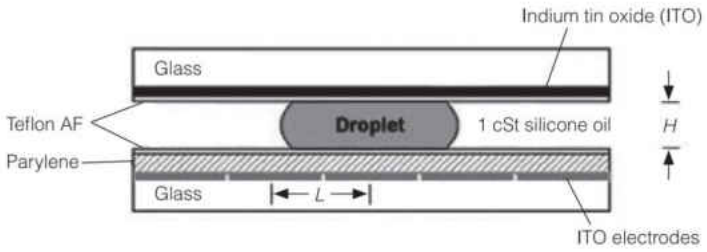

Fig. 29. Electrowetting effect on a digital-microfluidic platform [58].

Electrowetting also can be used in electronic display (e-paper) [59-62]. As shown in Fig. 30, Hayes and Feenstra [59] used the principle of the electrowetting. The colored oil on the hydrophobic insulator was at the bottom of the water. By applying the voltage between the bottom electrode and water, the oil moves to the corner and pushes to the corner of the pixel. Finally, the form of the colored oil creates a different color on a screen.

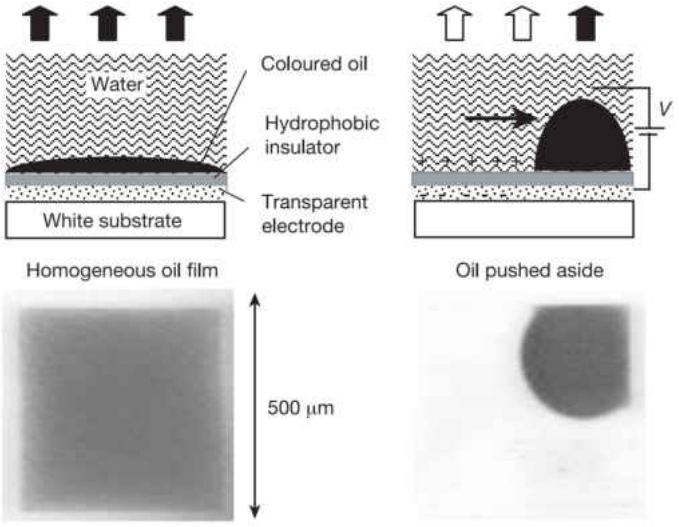

Fig. 30. Schematic electrowetting display [59].

Another application of electrowetting is optical application [63]. Kuiper *et al.* [64] studied the change of contact angle in the lens in Fig. 31 to change the focus action. A 6 mm diameter cylindrical transparent chamber was coated with hydrophobic material on the top and side walls. The conducting fluid and insulating fluid were an aqueous salt solution and oil viscosity of 7cSt (due to the lower viscosity), respectively. Two electrodes were insulated well on the side walls and the bottom of the device. By applying the voltage, the contact angle was expressed as follows:

$$cos\theta(V) = cos\theta_0 + \frac{\varepsilon V^2}{2\gamma_{LV} d} \tag{37}$$

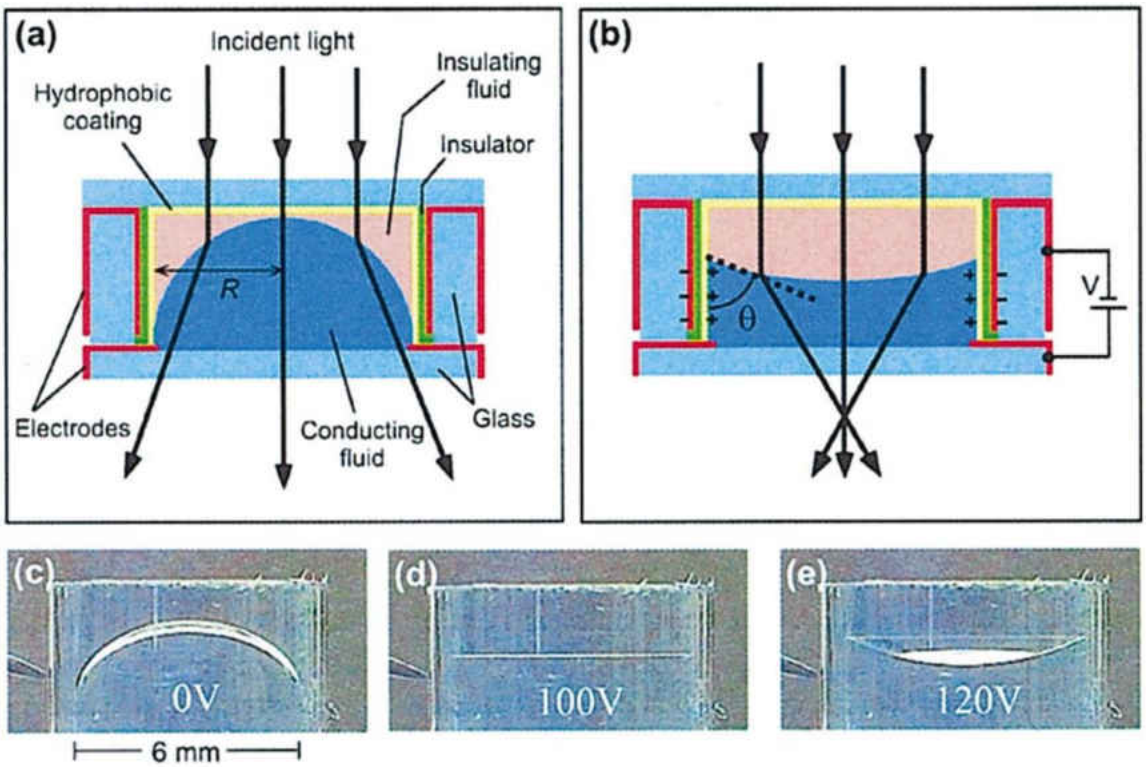

Fig. 31. The schematic of electrowetting lenses under a)no voltage b) voltage applied c) experimental result with no voltage applied, d) experimental result while 100V applied e) experimental result while 250V applied [64].

Researchers have been interested in contact electrowetting in microfluidic manipulation [49,65,66], and the use of tunable microlens [67,68]. The water droplet as shown in Fig. 32 was on the top of the transparent dielectric substrate the center of the electrode called V_0. The substrate did not contact with the electrodes with V_1, V_2, V_3, and V_4. By plugging in each of these voltages, the water was able to change the position and curvature.

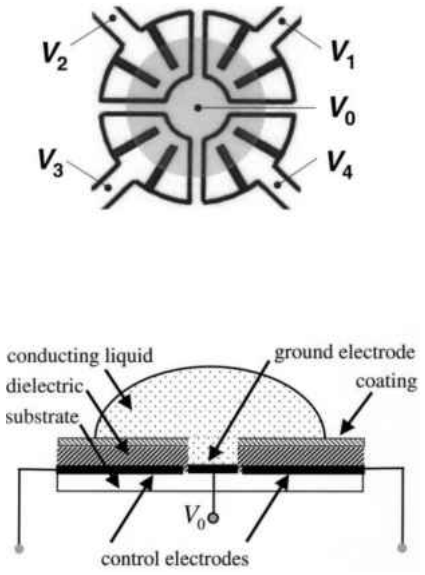

Fig. 32. Schematic of the tunable liquid microlens [67].

The other applications for electrowetting are biochemistry [69-71], mirrors [72], electrical microswitch [73], rheometer [74] thermal microswitch [75], Tensiometer [76].

In a normal situation, the water electrolysis occurs while the positive and negative electrodes in the water create 1.23 V from the standard electrode potential table [77]. However, in the electrowetting, the aim is not splitting the water. Hence, by adding the dielectric on the bottom

electrode, it will be prevented. The accumulation of charge inside the water changes the contact angle a shown in Fig. 33 [78]

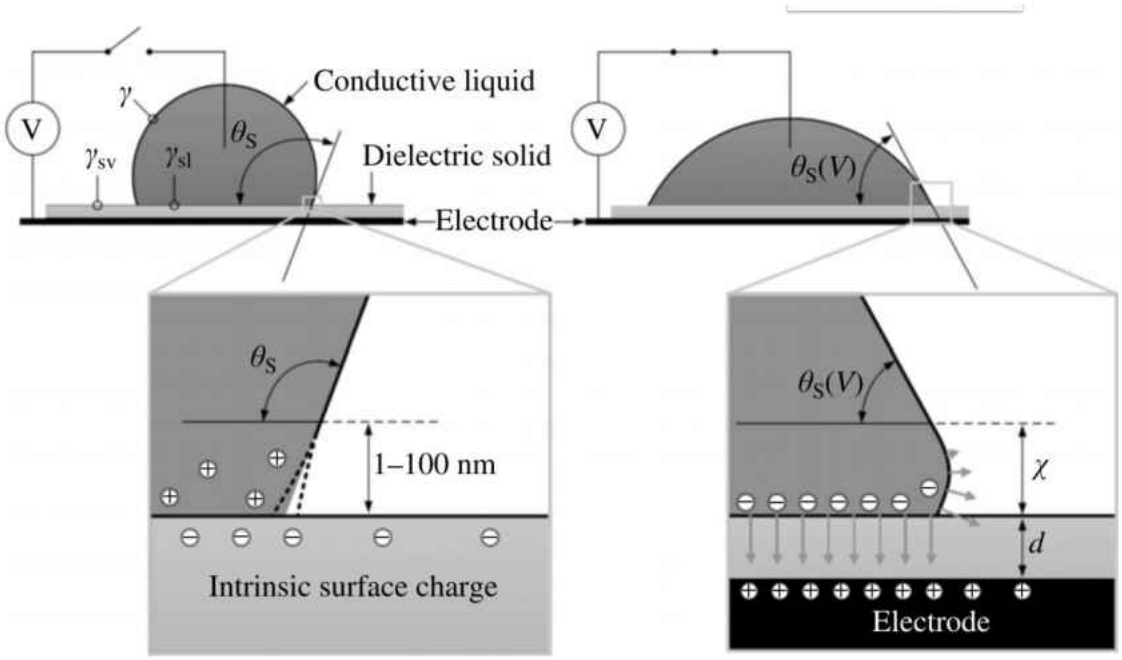

Fig. 33. The behavior of the contact angle under the electric field [78].

Jones [79] reported that total force per unit length of contact angle could be obtained with $\frac{C_d V^2}{2}$ which was an electrochemical derivation of the electrowetting equation. Kang [80] used electrostatic voltage and illustrated mathematically that thickness of the electrode affected the contact line by the use of Maxwell stress; this will be discussed in the following section.

Jones [81] investigated the effect the frequency voltage on the electrowetting. The model presented in Fig. 34. They used two cases low and high-frequency voltage. The model was tested while the pressure changed, and the electric field was measured. For the AC voltage (less than around 100V-rms), the pressure had a great agreement to the square-law of the model. However, in high voltage, that validation was not confirmed with the model.

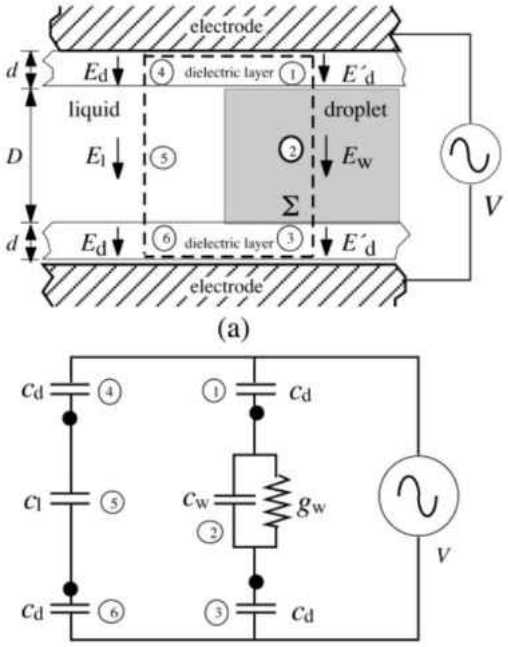

Fig. 34. Surface integration of the Maxwell stress tensor based on the pressure of the droplet. b)Electrical circuit model of the device[81].

Wang and Zhao [82] studied electrowetting on the dielectric (EWOD) on convex and concave surfaces as shown in Fig. 35. The governing equation of the summation of the force carve surface was expressed by:

$$dF = \gamma_{sl}dA - \gamma_{sv}dA + \gamma_{LV}dAcos\theta + dU - dW_b \tag{38}$$

where γ_{sl}, γ_{sv}, γ_{LV}, U, W_b, and A were donated solid-liquid surface tension, solid-vapor surface tension, liquid-vapor surface tension electric energy, work that the voltage source performs, and droplet base area, respectively.

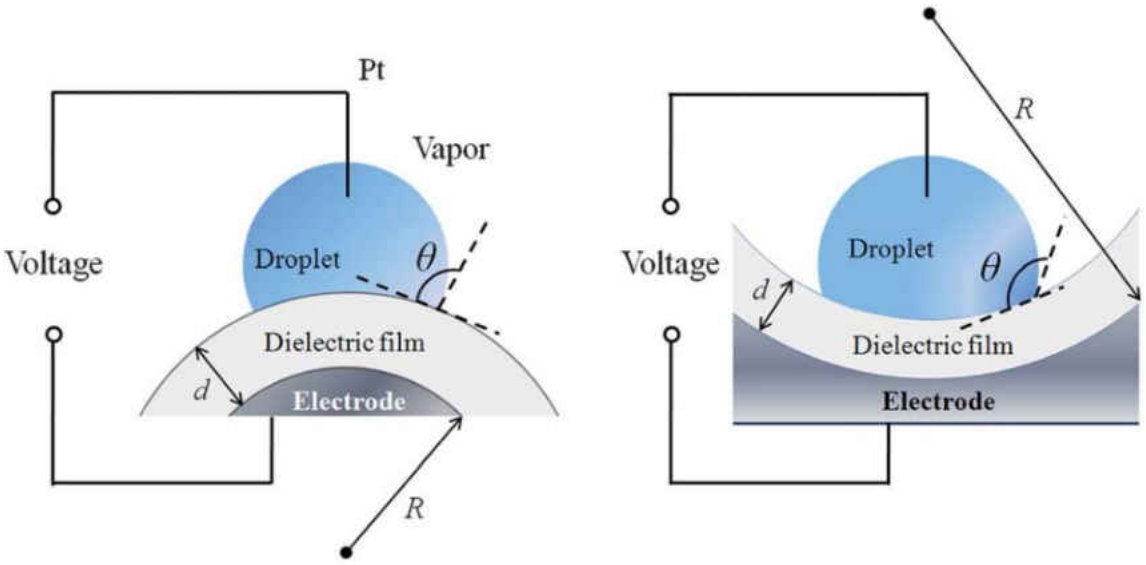

a) b)

Fig. 35. Schematic of EWOD on a) convex surface and b) concave surface [82].

The free energy is assumed to be zero due to the droplet remaining stable. Thus, equation (38) could be simplified as follows:

$$\gamma_{sl} - \gamma_{sv} + \gamma_{LV}\, cos\theta + \frac{dU}{dA} - \frac{dW_b}{dA} = 0 \tag{39}$$

After solving (39), the amount of the contact angle for the spherical surface was written in the form of:

$$cos\theta(V) = cos\theta_0 + \frac{\varepsilon V^2}{2\gamma_{LV} d} \cdot \frac{1}{1 \mp \alpha} \tag{40}$$

where $\alpha = d/R$ and d, R presented the thickness of the dielectric and radius of the electrode. The amount of $\frac{1}{1\mp\alpha}$ in equation (40) related to the convex surface and concave surface where for the convex surface, the term is $\frac{1}{1+\alpha}$ and for the concave surface, the term is $\frac{1}{1-\alpha}$.

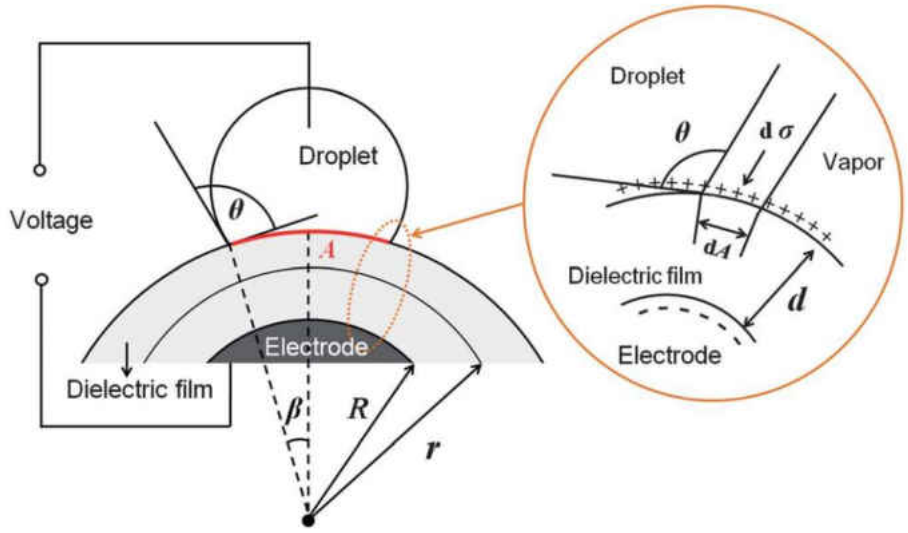

Fig. 36. Model for calculating the droplet on the convex [82]

For the solution for the droplet contact angle in the cylindrical surface, the contact angle was equal to:

$$cos\theta(V) = cos\theta_0 + \frac{\varepsilon V^2}{2\gamma_{LV} d} \cdot \frac{\alpha}{(1 \mp \alpha)\ln(1 \mp \alpha)} \tag{41}$$

In convex cylindrical surface and concave cylindrical surface, the term $\frac{\alpha}{(1+\alpha)\ln(1+\alpha)}$ and $\frac{\alpha}{(1-\alpha)\ln(1-\alpha)}$ should be considered.

The amount of spherical capacitance and the cylindrical per unit of the area was expressed by:

$$c = \frac{\varepsilon}{d(1 \mp \alpha)} \tag{42}$$

$$C = \frac{\varepsilon\alpha}{d(1 \mp \alpha)\ln(1 \mp \alpha)} \tag{43}$$

Hence, the general equation can be generalized as follows:

$$\cos\theta = \cos\theta_0 + \frac{1}{\gamma_{LG}}\frac{1}{2}cV^2 \tag{44}$$

In the theoretical chapter, the theory behind the droplet on a flat surface under the electric field will be discussed further.

Regarding equation (44), there are several parameters that can affect the contact angle such as the amount of the θ_0, γ_{LG}, d, ε_r, and V. The amount of the θ_0 depends on the amount the hydrophobic property of the material. Blake [83] studied the compression with hydrodynamic and atomistic. As shown in Fig. 37a, the microscopic contact angle θ_m was considered by small range intermolecular forces; that U made $\theta_m$was specified and kept the static value of contact angle in a static situation (θ_s). Fig. 37.b refers to the moving contact angle being affected by the dynamic friction in a channel, which had relation with contact angle line. In molecular-kinetic case, the amount of θ_D was equal to θ_m.

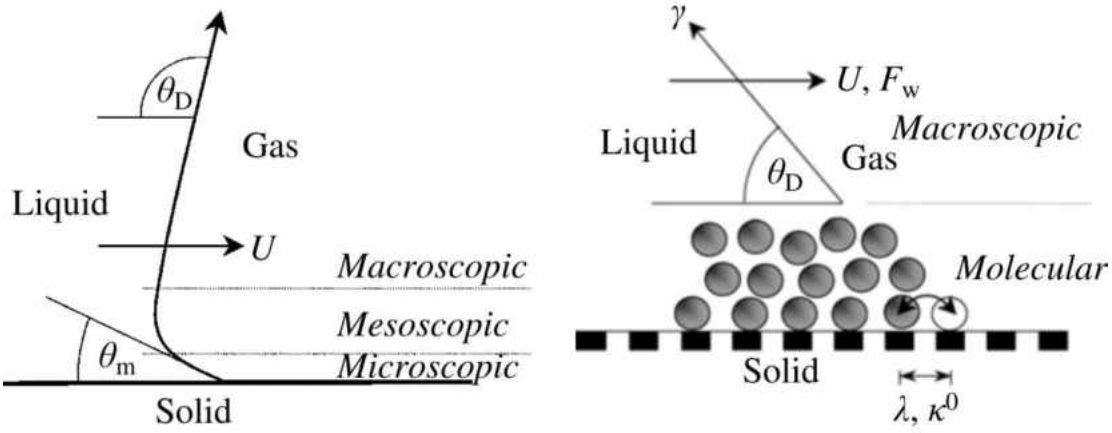

a) b)

Fig. 37. Wettability a) for an advancing meniscus bent on the mesoscale and b) regarding the molecular-kinetic theory [83].

In Table 1, regarding the molecular-kinetic theory, there are several electrolytes on the various hydrophobic material provided. The surface tension force was calculated:

$$F_w = \gamma(cos\theta_s - cos\theta_D) \tag{45}$$

On the solid surface, the distance adsorption sites were called λ; moreover, the wetting velocity was:

$$U = 2k^0\lambda\sinh[\gamma(cos\theta_s - cos\theta_D)\lambda^2/2K_B\mathrm{T}] \tag{46}$$

where K_B and T donated the Boltzmann constant and the absolute temperature, respectively. The amount of k^0 was expressed:

$$k^0 = (\frac{K_B}{h})\exp(\frac{-\Delta G_w}{NK_BT}) \tag{47}$$

where ΔG_w, h, and N are activation free energy of wetting, Planck constant and Avogadro number, respectively. The ζ in Table 1 is Eyring for dynamic viscosity ($\zeta\sim(\frac{v_m}{\lambda^3}\exp(Wa))$) where v_m is the molecular flow volume and work of adhesion liquid-solid.

Table 1. Experimental data from molecular-kinetic theory for the various system [83,84].

Liquid–solid system	**η (Pa s)**	**γ(mNm^{-1})**	**θ_s (◦)**	**λ (nm)**	**k^0 (s^{-1})**	**ζ (Pa s)**
Water on PET	0.001	72.4	82	0.36	8.6×10^9	0.01
16% glycerol/water on PET	0.0015	69.7	72.5	0.46	3.6×10^9	0.012
86% glycerol/water on PET	0.104	65.8	65	0.46	3.5×10^7	1.2
Di-n-butyl phthalate on PET	0.196	34.3	<5	1.8	1.1×10^5	6.4
Silicone oil on glass [85]	0.958	21.3	0	0.8	2.3×10^5	35.9
Silicone oil on glass [85]	98.8	21.7	0	0.8	2.3×10^5	3580

Moon used [86] several materials such as an Amorphous fluoropolymer (~Teflon®, AF, Dupont) as shown in Fig. 38, silicon dioxide (SiO_2), and parylene for electrowetting was discussed as the breakdown voltage as a dielectric. Due to the choice of the better dielectric, the voltage and permittivity of the material are important and should be considered.

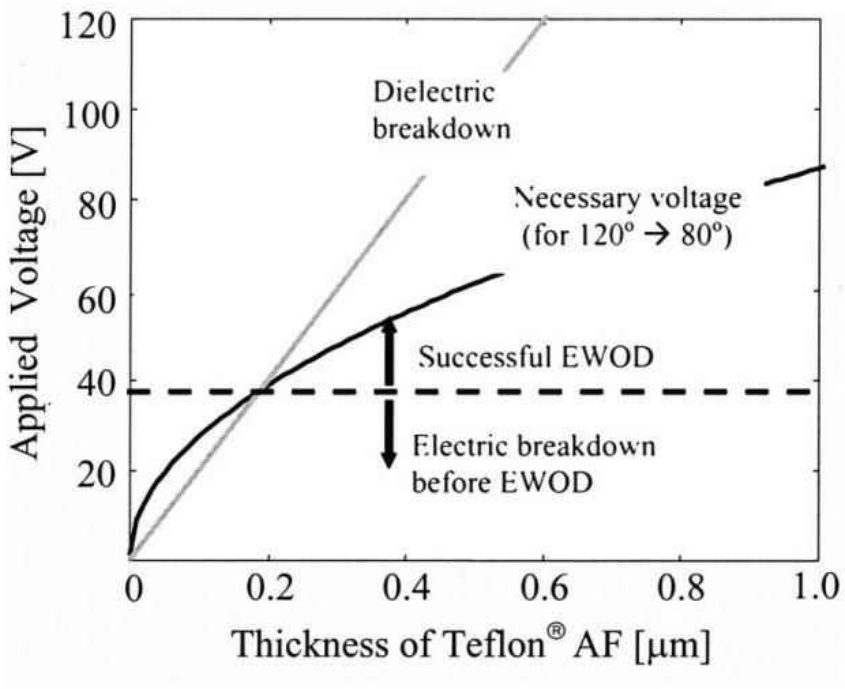

Fig. 38. The thickness of the Teflon® AF, Dupont versus voltage required while the contact angle changed from 120° to 80° the breakdown voltage base on the voltage was defined [86].

Several researchers used Polydimethylsiloxane (PDMS) [87,88] for electrowetting. Gerratt [89] mentioned that the breakdown voltage for the PDMS with the 2 to 14 μm between the silicon electrodes. The range of the breakdown was between 250 to 635 V μm^{-1}.

Various types of electrolytes in electrowetting have been used in biomechanical analysis such as saliva, urine, blood and buffer solutions [90,91]. Banerjee *et al.*[92] investigated different

biological solutions (sodium phosphate solution, sodium acetate solution, sodium chloride solution, sodium acetate electrolyte solution at pH 6, 7 and 8) for electrowetting as shown in

Fig. 39. In the experiment, the voltage was chosen from the previous researchers[93,94]; the contact angle in the experiment and the theory of Young-Lippmann equation [50] followed each other in most solutions while the voltage was lower than saturation point.

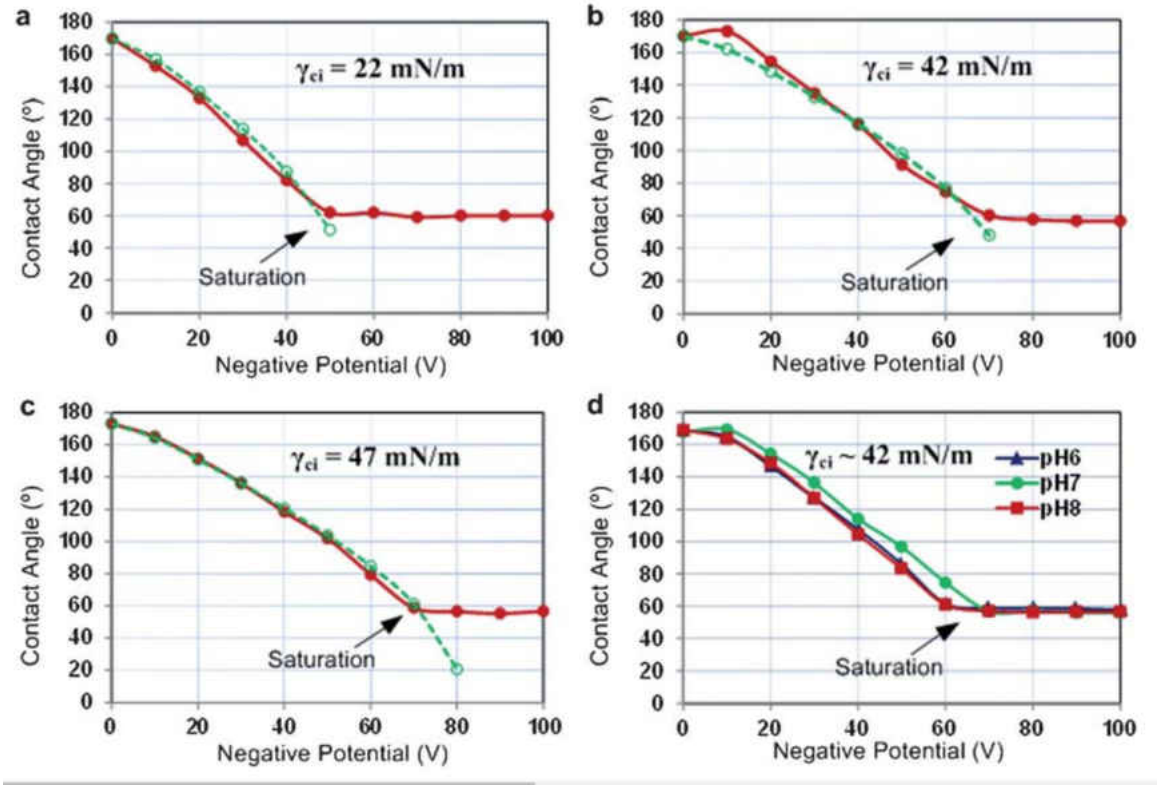

Fig. 39. Electrowetting characterization while various dielectric was used (a) sodium phosphate solution, (b) sodium acetate solution, (c) sodium chloride solution, and (d) sodium acetate electrolyte solution at pH 6, 7 and 8 where the dashed line and solid line represented Young-Lippmann equation theoretical result and experimental result [92].

Saeki et al.[95] illustrated that the breakdown voltage was increased while the thickness increased regarding Fig. 40. They could find out the low threshold voltage of around 6 V which was 133 Å (1 Angstrom is 10^{-10}m) Teflon layer as shown in

Table 2, and, they provided the result that wettability was reversible with the wettability of a surface. The saturation point was obtained while a high voltage applied and the contact angle was 60°. They also reported that the surface roughness and heterogeneity could impact on the contact angles.

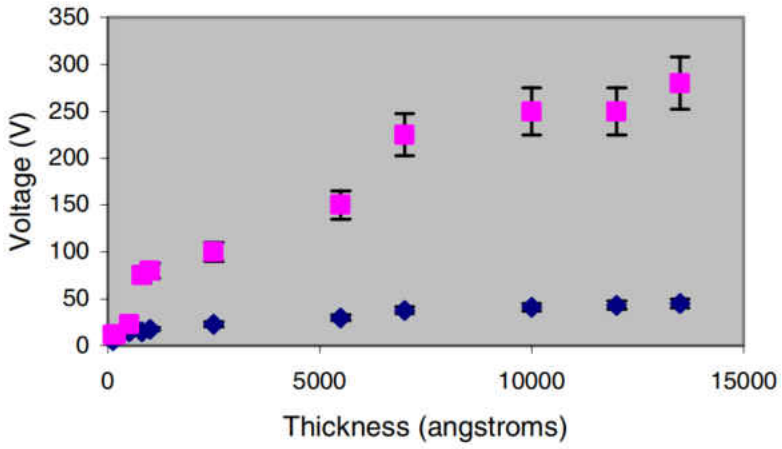

Fig. 40. Voltage thickness in the electrode [95]

Table 2. Experimental result of the electrowetting with the dielectric of Teflon layer thickness [95].

Concentration (wt.%)	**Thickness (Å)**	**Threshold voltage (V)**	**Breakdown voltage (V)**
6.0	16500	46	>300
5.5	13500	45	280
5	12000	43.5	250
4.5	10000	41	250
4	7000	38	225
3	5500	30	120
2	2500	23	100
1.5	1000	18	80
1	800	15	75
0.6	500	15	23
0.2	200	9.5	12
0.1	130	5.9	12

1.3 Contactless Electrowetting

In contactless electrowetting, the top electrode does not have contact with the water droplet[96]. Castaner and *et al.* [97] studied increasing the wettability on the dielectric substrate by the use of corona charge. As shown in Fig. 41, the source of charge supplied the charges, and the corona probe applied the charges in a very short time at the top of the water. The high voltage V_{th} from the power sources break down the molecule of the air with the electrical resistance of R_{th}, and the charges transferred to the water droplet and caused the contact angle of the droplet to

be impacted by the charges. Nevertheless, the water could be considered as a capacitor due to being as an energy saver.

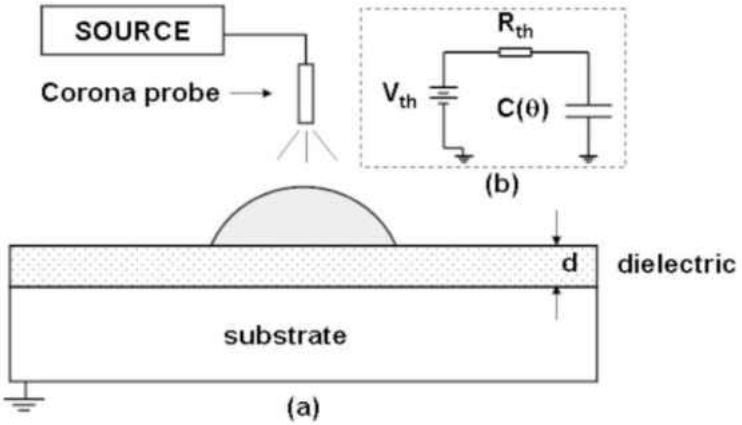

Fig. 41. a) contactless corona electrowetting b) electrical circuit of the contactless electrowetting [97].

Basaran et al. [98] designed and modeled a sessile droplet under the electric field. The distance from the top electrode to bottom coated electrode was H. The shape of the droplet (f(θ)) was the function of the contact angle as shown in Fig. 42.

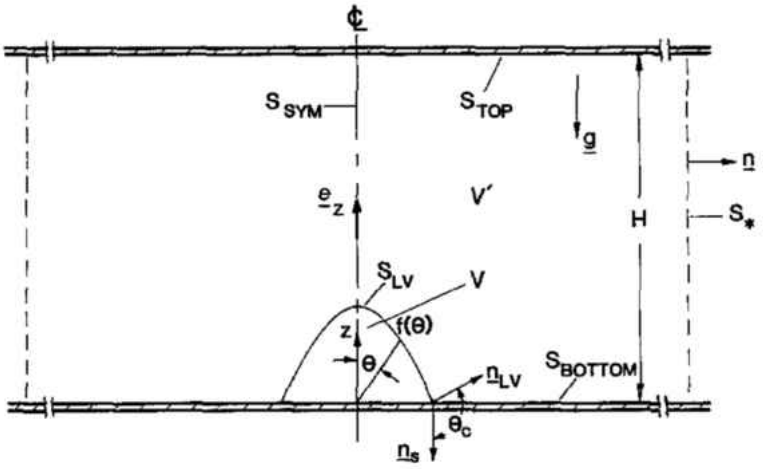

Fig. 42. Schematic of axisymmetric droplet under the electric field [98].

They reported that the physics of changing the droplet shape under the electrostatic field increased the accumulation of charge on the top of the droplet; that led to the droplet rising up as shown in Fig. 43.

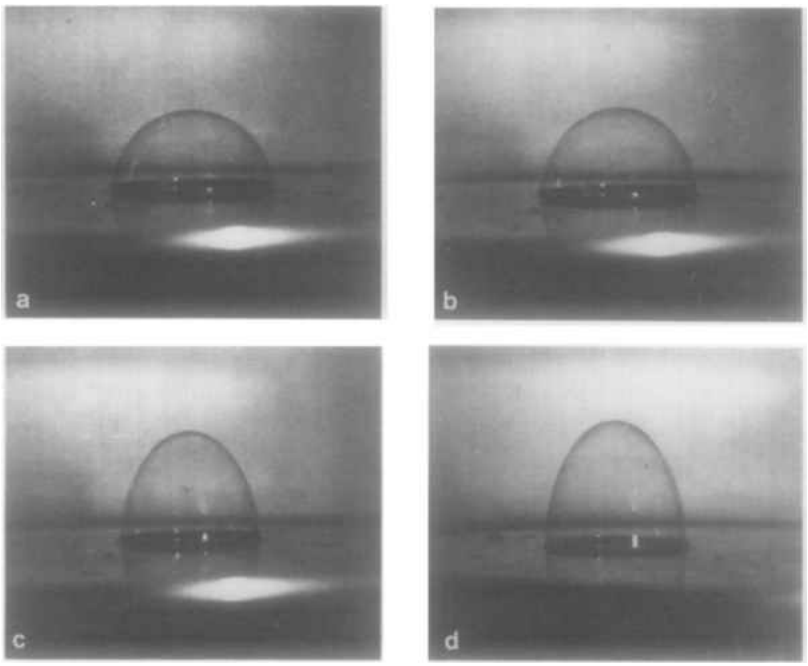

Fig. 43. Deformation of the droplet between the electrostatic field [98].

Several researchers worked on the effect of the electric field on the contact angle and surface tension of droplets [99-101]. Bateni *et al*. [99] investigated experimentally and analytically by Automated Polynomial Fitting (APF) to find out the change of the water droplet shape. They considered teflon as a hydrophobic material as shown Fig. 44. To keep the droplet at the center

and not to move on the substrate, a needle was fixed at the center. The top electrode was connected to high voltage; the bottom electrode was connected to the ground to create a strong electric field. As a result of their investigation, when polar liquids such as alcohol were used, contact angles of the droplet increased in the electric field by one or two percent. A liquid with longer molecules determined that the change of the contact angle was stronger.

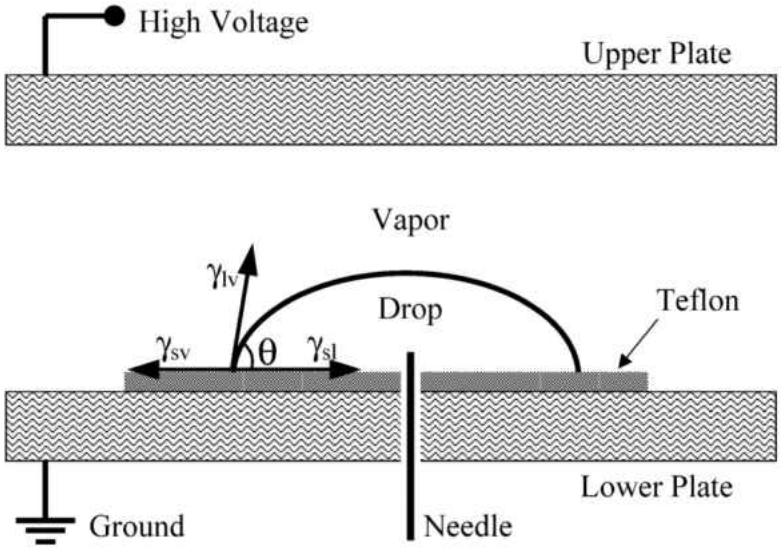

Fig. 44. The schematic of experimental setup [99].

There are several investigations that were carried on the physical dynamic of droplets such as wettability, the evaporation of the droplet, and increasing the rate of the evaporation [102-106]. The surface tension of the droplet under the electric field depends on the amount of the electric field, different types of electrolytes, liquid polarity, the size of molecules of water, and change of effective area under electric filed [99,107-109]. Vancauwenberghe [110] divided the change of the droplets under electric fields into three groups. These groups consisted of the impact the electric

field on the wetting angle, the effect the electric field on drop shape, and the influence the electric field on the rate of the evaporation.

In the first case, the wetting angle under the electric field distribution was the same as the conventional electrowetting. In the second case, the droplet formed as shown in Fig. 45 [111]. The profile of the droplet was based on the force of electric field of 13.3kV/cm as shown in Fig. 45.

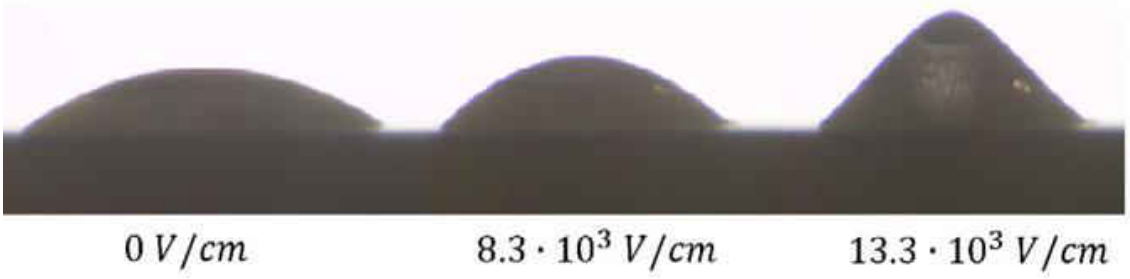

Fig. 45. Ethanol droplet under the various electric fields [111].

In the experiment, the adhesion and internal pressure forces increased by the electric field of 13.3 kV/cm, as shown in Fig. 46, in which the theoretical solution was the solid line in the picture. Moreover, the adhesion force and weight force reduced by increasing the electric field.

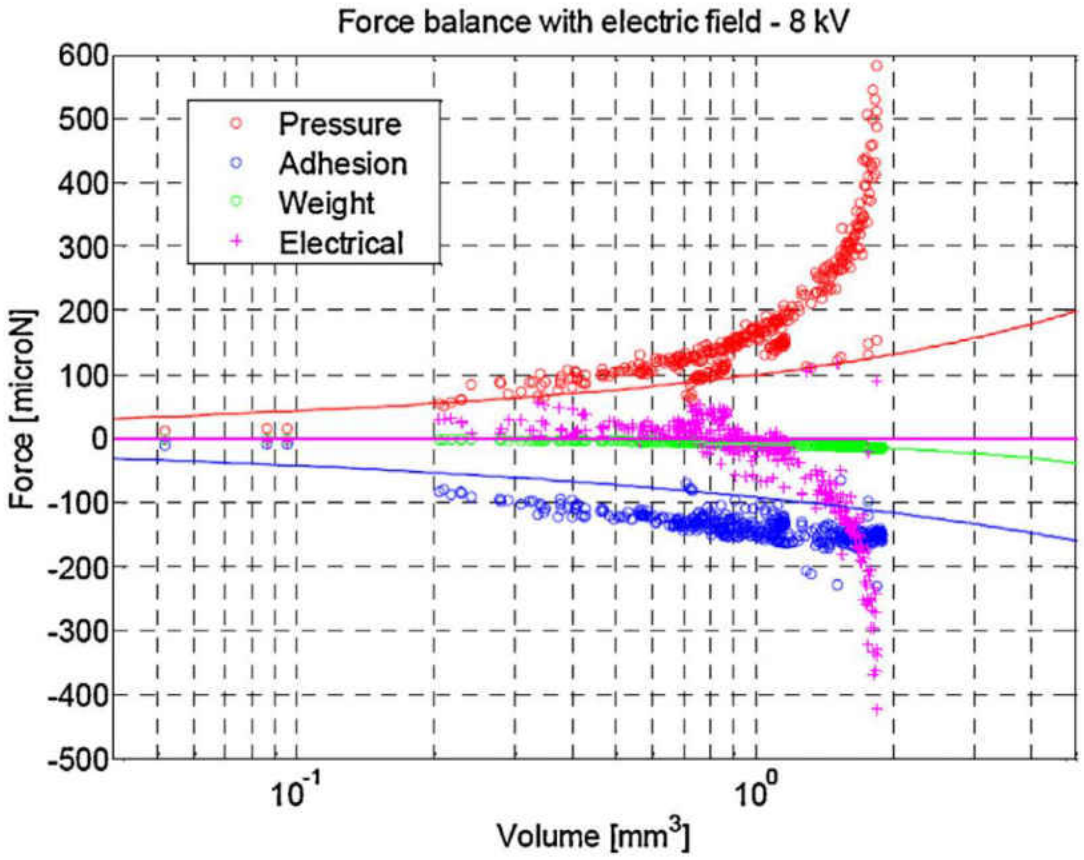

Fig. 46. Experimental values of the forces for an applied voltage of 8 kV [111].

The forces that were evaluated by FEM were -175μN; in the experiment, this amount was -165 μN. The error between the simulation and experiment was less than 6 percent and had a great agreement. Moreover, the amount of the electric contour was higher on the white block and close to the surface of the droplet.

In the third case, the evaporation of the droplet is really important due to industry application of the use of electrospraying, a cooling process, heat exchange between the droplet and environment, and drying the droplet from a surface. Several scientists have researched evaporation of a droplet by corona charge [112-115] and the model of the device[113]. Rouaud *et al.* [116] used an electric wind by a corona discharge to increase the heat transfer and dry the droplet faster

as shown in Fig. 47. The result showed that the efficiency is lower when the velocity of air was high.

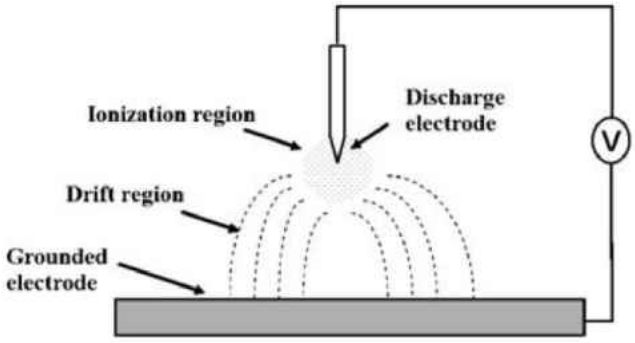

Fig. 47. Corona discharge setup device [116].

The electric field between the water droplet leads to an effect on the surface tension of the water droplet and rises up the water droplet; then, water droplet collapses to the end of the top electrode connect with the water droplet.

CHAPTER 2

METHODOLOGY

2.1 Microfluidic Kelvin Water Dropper

The schematic diagram of the electrowetting system using a MKWD is shown in Fig. 52. The MKWD mainly consists of a syringe pump, two microfluidic channels, two inductors, and two collectors. DI water is injected by a syringe pump (Harvard Apparatus PHD 2000) into two microfluidic channels made of polydimethylsiloxane (PDMS). To fabricate the PDMS, the elastomer is mixed with the curing agent with 10:1 ratio. A layer of the PDMS is put inside the petri dish and it was left 1.5 hours in the ambient air to omit any bubbles inside the solution. After leaving it 8 hours on the hot plate with the temperature of 80 °C, the layer will be solid. Then, two tubes with two different diameters of 254 μm and 508 μm are placed inside the solid layer, and another PDMS solution are put inside that. Next, the petri dish with all items is left for 1.5 hours then put on the hot plate for 8 hours at the temperature of 80° C. Finally, the tube should be taken out of the PDMS. To add the rings as an electrode, the channel is cut, then the rings are insulated electrically very well by electric insulator spray. All connections and tubes are connected with flexible plastic tubes. Next, they are connected with the syringe with the volume of 100 ml. To increase the volume of the fluid and increase the duration of the experiment, two syringe pumps are used. With the syringe pump, it is possible to adjust basic information such as the volume of the syringe and also the flow rate.

By starting the syringe pump in the specific range of the flow rate, the water jets break into droplets after passing through the induction rings, which are made of copper and well insulated by liquid electrical tape. The water droplets with electrostatic charges are collected by the aluminum foil placed at the bottom of the beakers. The inductors and collectors are cross-linked so that a

positive feedback system is formed to generate a high potential difference between electrodes. Initially, there is a slight potential difference between two collectors by nature. Once water starts flowing, the inductors (either slightly positive or negative) attract the ions with opposite charge, whereas it expels those that are the same. Therefore, the more water droplets are collected, the higher potentials the collectors can reach. That will result in the higher potentials of the inductors, which in turn further enhance separation of the charges in water. Ultimately, the output potentials will reach a dynamically steady state where the leakage current counters the generated charges.

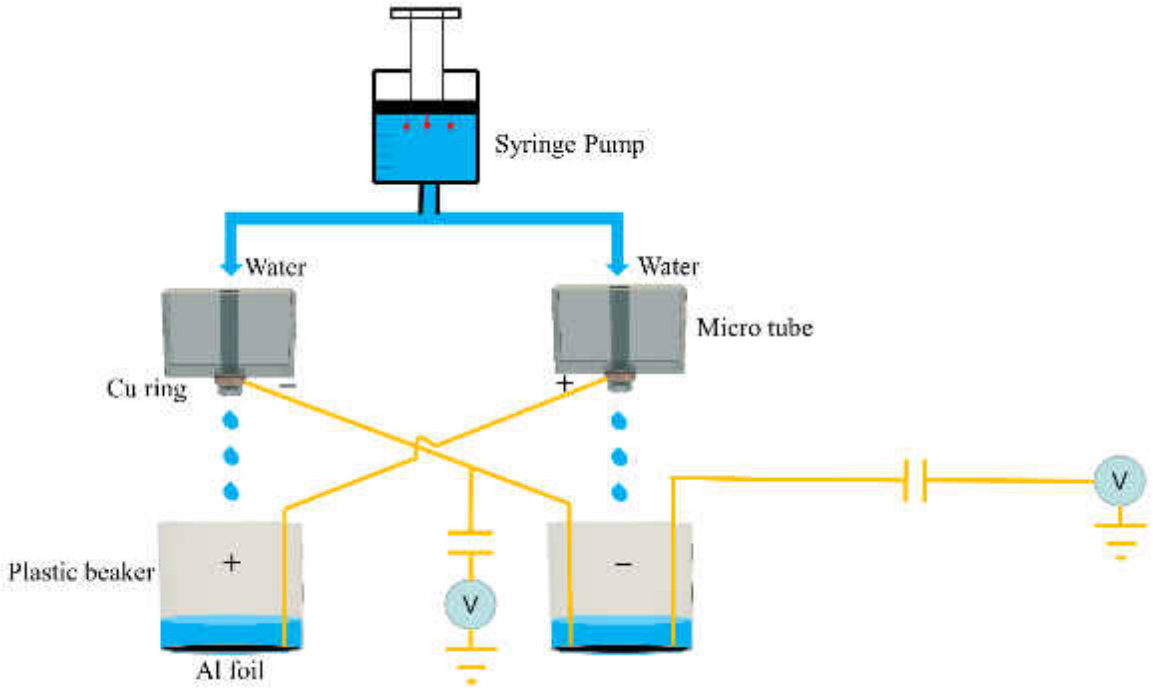

Fig. 48. The schematic of the microfluidic Kelvin water dropper

2.2 Contact Electrowetting by Microfluidic Kelvin Water Dropper

2.2.1 Simulation for Contact Electrowetting

In this present work, an analytical model was built to simulate the time-dependent deformation of a water droplet during electrowetting using MKWDs. COMSOL (version 5.1) was used to carry out the simulation. The simulation results were compared to the experimental observation side by side, as to validate the model. Fig. 49 illustrates the model adopted in the simulation, in which an axisymmetric configuration was used, assuming the shape of the droplet is a perfect hemisphere [117]. The initial diameter of the water droplet in the model was set at 2.44mm, in alignment with the actual size used in the experiment for comparison. The droplet was fixed on a dielectric PDMS substrate with a thickness around 50μm, at which no dielectric breakdown occurs in the present experiments[89]. Zero prescribed z displacement was applied as the boundary conditions to the top and bottom edges. Additionally, zero prescribed r displacement was applied as the boundary conditions to the left and right edges. Navier slip was applied to the bottom boundary due to the hydrophobic property of the dielectric substrate (i.e. PDMS) and the associated frictional force can be expressed:

$$F_{fr}=-\mu\frac{u}{\beta} \tag{48}$$

where μ, u, and β denote viscosity of the fluid, fluid velocity, and slip length, respectively. In addition, non-slip was applied to both the right and the top boundaries, within which air is confined. Finally, a liquid interface was set as the boundary between the water droplet and air. The contact angle is defined as the angle formed between the tangent of inside the water droplet and the bottom substrate [118,119].

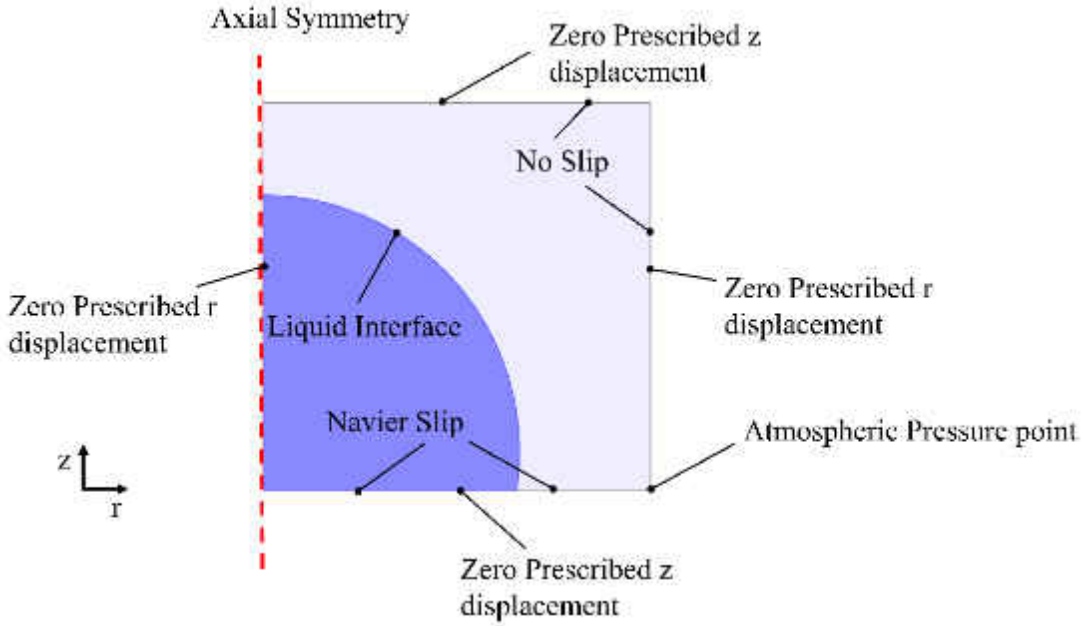

Fig. 49. Simulation model of the droplet deformation on a PDMS substrate during electrowetting.

To solve this problem analytically, the two-phase compressible flow Navier-Stokes equation was adapted [120,121]. Hence, Laminar Tow-Phase Flow Moving Mesh in COMSOL was selected [97]:

$$\rho\frac{\partial \mathbf{u}}{\partial t}+\rho(\mathbf{u}\cdot\nabla)\mathbf{u}=\nabla\left[-p\mathbf{I}+\mu(\nabla\mathbf{u}+(\nabla\mathbf{u})^{T})-\frac{3}{2}\mu(\nabla\cdot\mathbf{u})\mathbf{I}\right]+\mathbf{F}_{s}+\mathbf{F}_{b} \tag{49}$$

$$\rho\frac{\partial \mathbf{u}}{\partial t}+\nabla(\rho\mathbf{u})=0 \tag{50}$$

where u, ρ, μ, p, $\mathbf{F}_s$, and $\mathbf{F}_b$ denote velocity field, mass density, dynamic viscosity, pressure, surface force per unit volume, and body force per unit volume, respectively. $\mathbf{F}_s$ can be expressed as [119]:

$$\mathbf{F}_{s}=\nabla\cdot\sigma(\mathbf{I}-(\mathbf{nn})^{T})\delta \tag{51}$$

where I, σ, n and δ represent identity matrix, co-efficient of surface tension, interface normal direction, and direct delta function, respectively. The direct delta function can be defined as:

$$\delta = \begin{cases} \dfrac{(1+\cos(2\pi\emptyset))}{3h} & if\ |\emptyset| \le 1.5h \\ 0 & otherwise \end{cases} \tag{52}$$

where h and ∅ are the grid spacing and level set function. The level set function is a function of the lowest distance from the center of the droplet to the interface and time as determined below:

$$\emptyset(x,t) = \begin{cases} > 0 & outside\ of\ the\ interface \\ = 0 & at\ the\ interface \\ < 0 & inside\ of\ the\ interface \end{cases} \tag{53}$$

$\mathbf{F_b}$ in the present scenario is only attributed to the electric forces, whereas gravity is neglected. Thus $\mathbf{F_b}$ can be written as following [97]:

$$\mathbf{F_b} = \nabla \cdot \widetilde{\mathbf{T}} \tag{54}$$

$$\widetilde{\mathbf{T}} = \mathbf{E}\mathbf{D}^{\mathrm{T}} - \frac{1}{2}(\mathbf{E}\cdot\mathbf{D})\mathbf{I} \tag{55}$$

$$\mathbf{E} = -\nabla \mathrm{V} \tag{56}$$

$$\mathbf{D} = \varepsilon_0 \varepsilon_{\mathrm{r}} \mathbf{E} \tag{57}$$

where **E**, $\widetilde{\mathbf{T}}$, **V**, and **D** denote electric field, Maxwell stress tensor, electrostatic voltage, and electric displacement field, respectively. Moon *et al.* [86] reported that the surface tension of interface in electrowetting was affected by both electrical and chemical segments. Those segments were created by the potential difference between the water droplet and the substrate, which can be described using Lippmann's equation [86]. The electric segment was introduced as a capacitor, whereas the chemical segment was defined as the natural surface tension of the droplet on the interface. Additionally, Lipmann's equation was derived from Gibbsian interfacial thermodynamic analysis of the interface. Hence, this equation was implemented into the present simulation due to

the similarities in our experiment setup. As mentioned before, the electric field on the solid-liquid interface affects the amount of the charged counter ions in the water droplet, and their relationship can be explained by equation (58) [122]:

$$\gamma_{SL} = -\rho_{sl}\, dV = -\int_{v_p}^{v} \rho_{sl}\, dV \tag{58}$$

$$\rho_{sl} = \int_{v_p}^{v} c\, dV \tag{59}$$

where γ_{SL}, ρ_{sl}, V, v_p, and c are the surface tension of solid-liquid interfaces, the surface charge density of counter-ions, the applied voltage, the voltage of trapped charge and the capacitance across the interface, respectively. By substituting equation (59) into (58), γ_{SL} can be expressed as [86] :

$$\gamma_{SL} = \iint_{v_p}^{v} c dV\, dV = \gamma_0 - \frac{1}{2} cV^2 \tag{60}$$

where γ_0 is the surface tension of solid-liquid interface at the potential zero charge. In Lippman's equation (as shown below), the contact angle is affected by the surface tensions of interfaces, including liquid-gas (γ_{LG}), solid-gas (γ_{SG}), and solid-liquid (γ_{SL}).

$$\gamma_{LG}\, cos\theta = \gamma_{SG} - \gamma_{SL} \tag{61}$$

where θ is the contact angle. By combining (58) and (60), Lipmann's equation can be written as [86]:

$$\cos\theta = \cos\theta_0 + \frac{1}{\gamma_{LG}} \frac{1}{2} cV^2 \tag{62}$$

where θ_0 is the initial contact angle of the liquid-solid interface prior to applying an electric field. The above equation indicates that the contact angle depends on several parameters, including the original state, the surface tension of liquid-gas (γ_{LG}) which refers to water and air in the present case, applied voltage (V) on the water droplet, and the interface capacitance (c) per unit area, which is expressed below [86]:

$$c = \frac{\varepsilon_0 \varepsilon_r}{d} \tag{63}$$

where ε_r, ε_0, and d are relative permittivity, vacuum permittivity, and thickness of the dielectric, respectively. The expression of the contact angle can be derived from Equations (62) and (63)as shown below:

$$\theta = \arccos(\cos\theta_0 + \frac{1}{\gamma_{LG}} \frac{1}{2} \frac{\varepsilon_0 \varepsilon_r}{d} V^2) \tag{64}$$

In simulation, θ_0 was set at 90° in alignment with the initial angle observed in the experiments. Other parameters, including γ_{LG}, ε_r, and d were set at 0.072 N/m [123], 2.56 [124], and 0.05 mm, respectively. The time dependent voltage used in the simulation was obtained from the curve fitting of the voltage curve logged during the experiments.

2.2.2 Experiment for Contact Electrowetting

The electrowetting setup consists of a working electrode, a dielectric substrate, and a counter electrode. The working electrode made of a steel needle with the diameter of 0.31 mm was inserted into the droplet. Ideally, the needle should be placed exactly at the center of the water droplet to prevent any movement of the water droplet due to charge imbalance. An electric field obtained from the output of the MKWD was applied through the needle. The counter electrode was made of a 0.9 mm thick titanium (Ti) pellet (Fig. 50).

Fig. 50. The Titanium pellet 2cm*2.5cm used as an electrode.

The Ti pellet was coated with a thin layer of PDMS, which serves as a dielectric substrate. All the surface voltage (i.e. electrostatic voltage) measurements were performed via an electrostatic voltmeter (AlphaLab, Model SVMII) as shown in Fig. 51.

Fig. 51. Surface DC Voltmeter Model SVM2 using in the experiment.

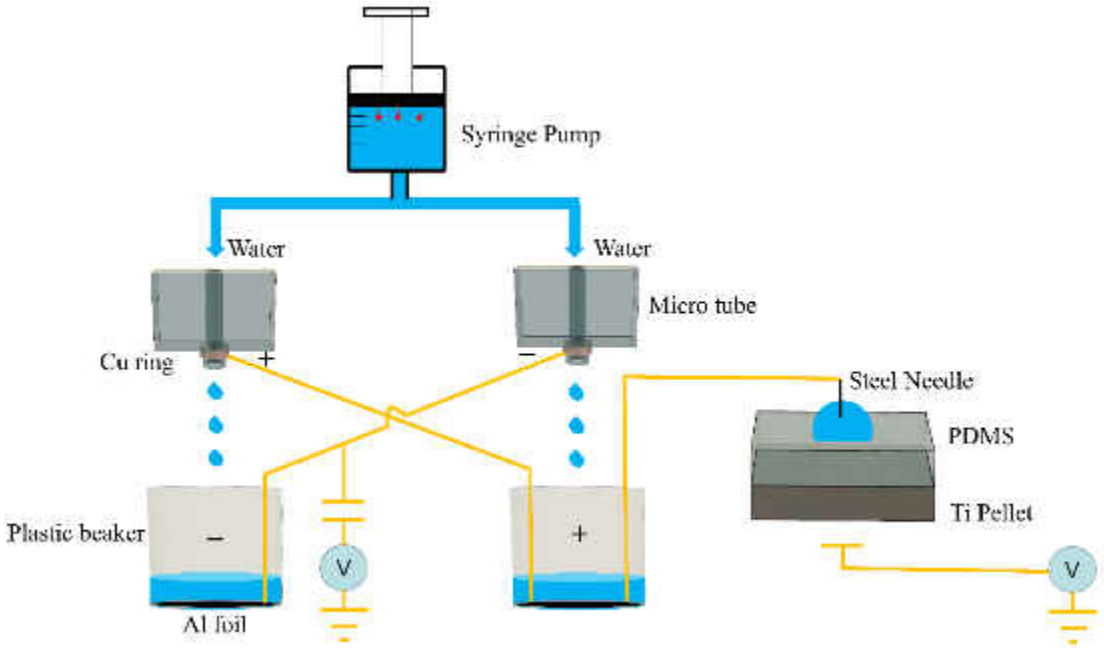

Fig. 52. Schematic diagram of the electrowetting system using the MKWD.

The micro-channels of MKWDs were fabricated through a molding process, in which two long steel needles were embedded into a PDMS substrate. The PDMS substrates were cured for 8 hours on a hot plate at 80 °C. Thereafter, the needles were removed to create the micro-channels. The needles with different diameters (254 µm and 508 µm) were used in order to investigate the sizing effect on the output of MKWDs. To fabricate the electrowetting setup, a Ti pellet was coated by PDMS to form a hydrophobic dielectric layer using a spin coater MTI Corp. Model VTC-100 at the speed of 500 revolutions per minute (rpm) for 4 seconds. Then, the coated Ti pellet was air dried for 8 hours on a hot plate at 80°C.

Prior to PDMS preparation, the Ti pellet was cleaned in an ultrasonic bath using ethyl alcohol for 15 min. Then to fabricate PDMS, the elastomer was mixed with the curing agent with 10:1 ratio. After mixing, the PDMS was settled in ambient air for one and half hours so that air bubbles could be expelled out. To fabricate the electrowetting setup, PDMS was deposited on the

Ti pellet to form a hydrophobic dielectric layer using a spin coater (MTI Corp. Model VTC-100) at 500 revolutions per minute (rpm) for four seconds. Finally, the setup was air dried at 80°C for 8 hours on a hot plate

The reason that PDMS coated on the Ti can be mentioned that PDMS is a common material for microfluidics devices [125]. Ti pellet has been chosen due to its physiochemical stability under the high voltage [126] and has been unutilized in electrowetting devices due to its capability of the reflective property [127].

Fig. 53. Spin coater MTI Corp. Model VTC-100.

Performance characterizations of the fabricated MKWDs were carried out, in order to identify the optimized operating parameters of MKWDs for electrowetting. High voltage generation, fast response time, and stable output were used as the criteria for selecting the

appropriate operating parameters. The output of two MKWDs with different tube inner diameters (IDs) (254 µm and 508 µm) were investigated under different flow rates.

Table 3 lists the operating conditions of the MKWDs investigated. The experiment sets A1 and A2 represent the operating parameters associated with two MKWDs with different IDs. After the performance characterization, the best performing MKWD with the optimized flow rate was used to carry out experiments on electrowetting (experiment B), with the operating parameters also listed in

Table 3. In all the experiments, the distance between the center of right and left inductors, the distance between the end of the microfluidics tubes and the center of two collectors are 60 cm, 40 cm, and 60 cm, respectively.

Table 3. Operating conditions of the MKWDs

	Channel ID (µm)	Water Flow Rate (ml/min)	Water Flow Speed (m/s)	Ambient Humidity (%)	Ambient temperature °C
		30	**2.517**		
A1	**508**	**40**	**3.356**	**48±3**	**22**
		50	**4.195**		
		7.5	**2.517**		
A2	**254**	**10**	**3.356**	**48±3**	**22**
		12.5	**4.195**		
B	**254**	**12.5**	**4.195**	**48±3**	**22**

2.3 Contactless Electrowetting by Microfluidic Kelvin Water Dropper

2.3.1 Simulation for Contactless Electrowetting

According to Vito Di Virgilio, to solve the CFD analytically, two-phase flow Navier-Stokes equation is considered due to fluid deformation on the substrate[96]:

$$\rho\frac{\partial \mathbf{u}}{\partial t}+\rho(\mathbf{u}\cdot\nabla)\mathbf{u}=\nabla\left[-p\mathbf{I}+\mu(\nabla\mathbf{u}+(\nabla\mathbf{u})^{T})-\frac{3}{2}\mu(\nabla\cdot\mathbf{u})\mathbf{I}\right]+\mathbf{F}_{s}+\mathbf{F}_{b} \tag{65}$$

$$\rho\frac{\partial \mathbf{u}}{\partial t}+\nabla.(\rho\mathbf{u})=0 \tag{66}$$

where ρ, t, u ,μ, p, $\mathbf{F}_{s}$, and $\mathbf{F}_{b}$ represent the density, time, velocity field, dynamic viscosity, pressure, surface tension force per unit volume, various forces such as gravity, magnetic fields, and electric fields per unit volume, respectively. Surface tension forces can be written as below in equation [119]:

$$\mathbf{F}_{s}=\nabla.\sigma(\mathbf{I}-(\mathbf{nn})^{T})\delta \tag{67}$$

where I, σ, δ, and n express identity matrix, coefficient of surface tension, direct delta function, and interface normal respectively. Direct delta function can be written as follows:

$$\delta=\begin{cases}\dfrac{(1+\cos(2\pi\phi))}{3h} & if\ |\phi|\le 1.5h\\ 0 & otherwise\end{cases} \tag{68}$$

where h and ϕ denote the grid spacing and level set function, which depends on the lowest distance from time and the center of the droplet to the interface, and is defined as:

$$\phi(x,t)=\begin{cases}>0 & outside\ of\ the\ interface\\ =0 & at\ the\ interface\\ <0 & inside\ of\ the\ interface\end{cases} \tag{69}$$

In the present simulation, gravitational force is negligible, and only body force, which can make an impact on the water droplet, is an electrical force. The electrostatics interface follows equation (70) for the electric potential V from poison equation:

$$-\nabla.(\varepsilon_0\varepsilon_r\nabla\mathbf{V}) = \rho_f \tag{70}$$

where ε_r, ε_0, and ρ_f denote the relative permittivity, the permittivity of vacuum, and free charge density, respectively. To solve the problem, two physics of Two-Phase Flow interface and electric force should be coupled. The divergence of the electric force is as follows [96]:

$$\mathbf{F_b} = \nabla \cdot \tilde{\mathbf{T}} \tag{71}$$

where $\tilde{\mathbf{T}}$ is Maxwell stress tensor. The Maxwell stress tensor is expressed as:

$$\tilde{\mathbf{T}} = \mathbf{E}\mathbf{D}^{\mathrm{T}} - \frac{1}{2}(\mathbf{E}.\mathbf{D})\mathbf{I} \tag{72}$$

$$\mathbf{E} = -\nabla\mathrm{V} \tag{73}$$

$$\mathbf{D} = \varepsilon_0\varepsilon_{\mathrm{r}}\mathbf{E} \tag{74}$$

where E and D are the electric fields and the electric displacement field, respectively. The amount of the relative permittivity is:

$$\varepsilon_{\mathrm{r}} = \mathrm{V_{f1}}\,\varepsilon_{\mathrm{r1}} + \mathrm{V_{f2}}\,\varepsilon_{\mathrm{r2}} \tag{75}$$

where $\varepsilon_{\mathrm{r1}}$ and $\varepsilon_{\mathrm{r2}}$ are absolute permittivity of water and air, respectively. The amounts of $\mathrm{V_{f1}}$ and $\mathrm{V_{f2}}$ are volume fraction for air and water respectively. The previous discussion about the simulation of the droplet is accomplished by COMSOL 5.1. As shown in Fig. 54, for the simulation, the geometry of the device is axisymmetric that the water droplet is the same size (volume 0.4 ml) with the experiment.

The boundary condition of the contactless electrode with water droplet has two phases with different boundaries as shown in Fig. 54. The electric field causes that top electrode to absorb opposite charges from the water droplet; then, the high voltage ionizes the air and charges will be

transferred into the water droplet. Thus, the physics in COMSOL for the device during the first phase are defined by electrostatics and laminar two-phase flow, moving mesh. Electrical potential on top of the geometry changed with the time-dependent voltage, which was gained from MKWD. The bottom substrate is grounded in an experiment, which is zero electrical potential. Also, the right side of the geometry and bottom PDMS are assumed zero-charge (Q=0) in the device due to not having charge in the ambient. The right and left sides of the geometry are zero prescribed r displacement because mesh in the r direction does not change. Also, the mesh on top and bottom of the geometry does not change in the z-direction. Therefore, the top and bottom are defined as a zero prescribed z displacement. The border between the water droplet and the air is defined as the liquid interface. The right and top geometry are no-slip because of ambient air. The bottom of the substrate is considered Navier slip ($F_{fr} = -\mu\frac{\mathbf{u}}{\boldsymbol{\beta}}$ where μ, u, and β donate viscosity of the fluid, and the slip length) because of being a hydrophobic property of PDMS.

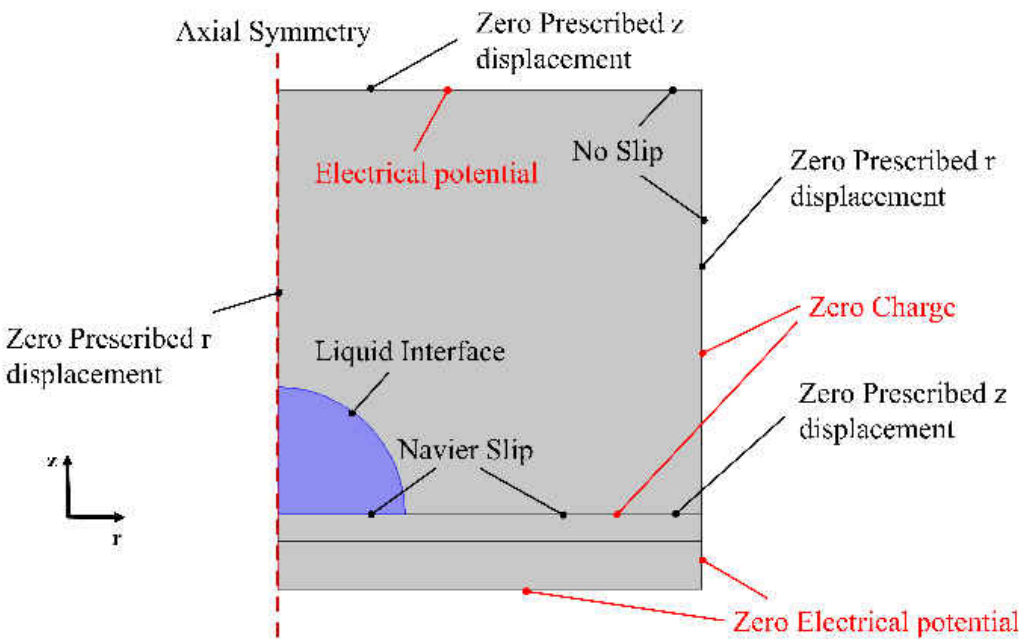

a)

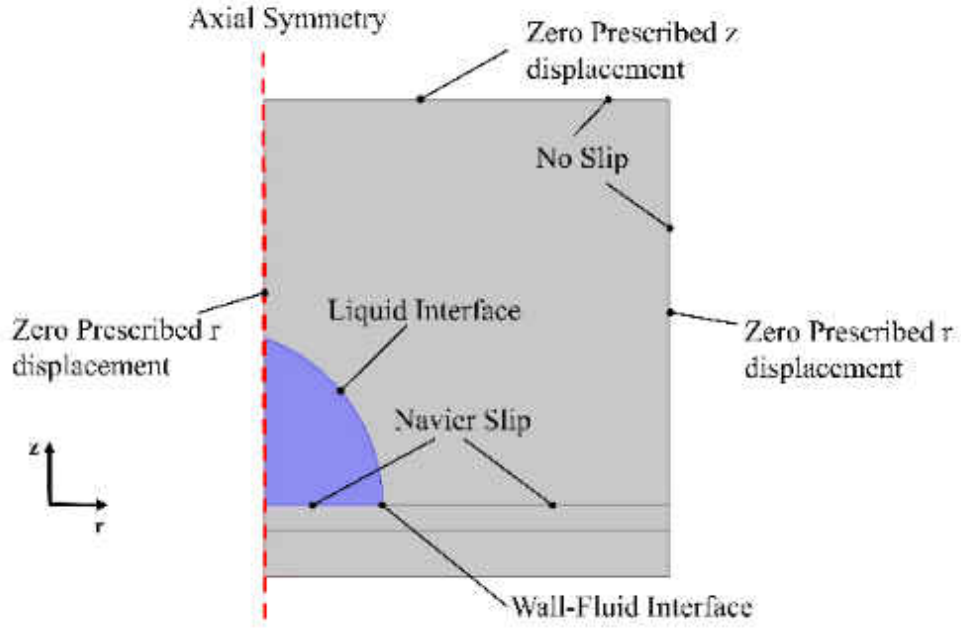

b)

Fig. 54. a) step one: boundary conditions in the COMSOL simulation for electrostatic and laminar two-phase flow, moving mesh. b) step two: boundary conditions in the COMSOL simulation for laminar two-phase flow, moving mesh.

The second phase, Naiver stock equation of the laminar two-phase flow, is considered for the simulation. The solid-liquid interface of the water droplet and air can be impacted by an electric field. The relationship of the amount of the charged counter-ions in water droplet can be expressed as follows [122]:

$$\gamma_{SL} = -\rho_{sl}\, dV = -\int_{v_p}^{v} \rho_{sl}\, dV \tag{76}$$

$$\rho_{sl} = \int_{v_p}^{v} c\, dV \tag{77}$$

where γ_{SL}, ρ_{sl}, V, v_p, and c denote the surface tension of solid-liquid interfaces, the surface charge density of counter-ions, the applied voltage, the capacitance across the interface, and the voltage of trapped charge, respectively. By substituting equation (77) into (76), γ_{SL} can be explained as [86] :

$$\gamma_{SL} = \iint_{v_p}^{v} cdV\, dV = \gamma_0 - \frac{1}{2} cV^2 \tag{78}$$

where γ_0 is the surface tension of solid-liquid interfaces at the potential zero charge. In Lippman's equation (as shown below), the contact angle is affected by the surface tensions of interfaces, including liquid-gas (γ_{LG}), solid-gas (γ_{SG}), and solid-liquid (γ_{SL}).

$$\gamma_{LG}\, cos\theta = \gamma_{SG} - \gamma_{SL} \tag{79}$$

The parameter θ is named the contact angle. By combining equation (78) and (79), Lipmann's equation can be written as [86]:

$$\cos\theta = \cos\theta_0 + \frac{1}{\gamma_{LG}} \frac{1}{2} cV^2 \tag{80}$$

where θ_0 is the initial contact angle of the liquid-solid interface prior to applying an electric field. The above equation indicates that the contact angle depends on several parameters, including the

original state, the surface tension of liquid-gas (γ_{LG}), which refers to water and air in the present case, applied voltage (V) on the water droplet, and the interface capacitance (c) per unit area which is expressed below [86] :

$$c = \frac{\varepsilon_0 \varepsilon_r}{d} \tag{81}$$

$$Q_A = CV \tag{82}$$

where ε_r, ε_0, d, and Q_A are relative permittivity, vacuum permittivity, the thickness of the dielectric, and charge per unit area, respectively. The expression of the contact angle can be derived from equations (81) and (80) as follows:

$$\theta = \arccos(\cos\theta_0 + \frac{{dQ_A}^2}{2\gamma_{LG}\varepsilon_0\varepsilon_r}) \tag{83}$$

In simulation, θ_0 was adopted at 90° in alignment with the initial angle observed in the experiments. In the step two, one physic of laminar two-phase flow, moving mesh is considered. The boundary condition is the same as laminar two-phase flow, moving mesh in fist step but by considering the highest raised droplet, the contact angle from (80) is added to the boundary condition at the wall-fluid interface.

2.3.2 Experiment Contactless Electrowetting

The present work studies contactless electrowetting by the use of MKWD. The system of the MKWD and the electrowetting components are demonstrated by Fig. 56. In the MKWD device, the DI water injects from the Harvard Apparatus PHD 2000 syringe pump (Fig. 55) on two microtubes then the droplet sprays on the collectors.

Fig. 55. Harvard Apparatus PHD 2000 syringe pump.

Two copper rings as inductors with a diameter of 10 mm are insulated by electric spray to prevent transfer charges from the outside to the system or vice versa. The electrodes are connected to two different Al foils as the collector inside the plastic dishes. In the electrowetting, a bottom Ti pellet as a substrate is coated with Polydimethylsiloxane (PDMS) with the thickness of thickness of 80 μm due to having a hydrophobic property to repel the water. A water droplet is on the coated substrate; also, a Ti plate as an electrode, which is fixed on the top of the droplet without contacting it, connected to one side of the MKWD collector. The electric field can be created between the electrode and substrate when the MKWD supplies the electrostatic voltage, which is measured by Surface DC Voltmeter Model SVMII. The deformation of the droplet shape is captured by AmScope Microscope with the camera of OMAX A3590U.

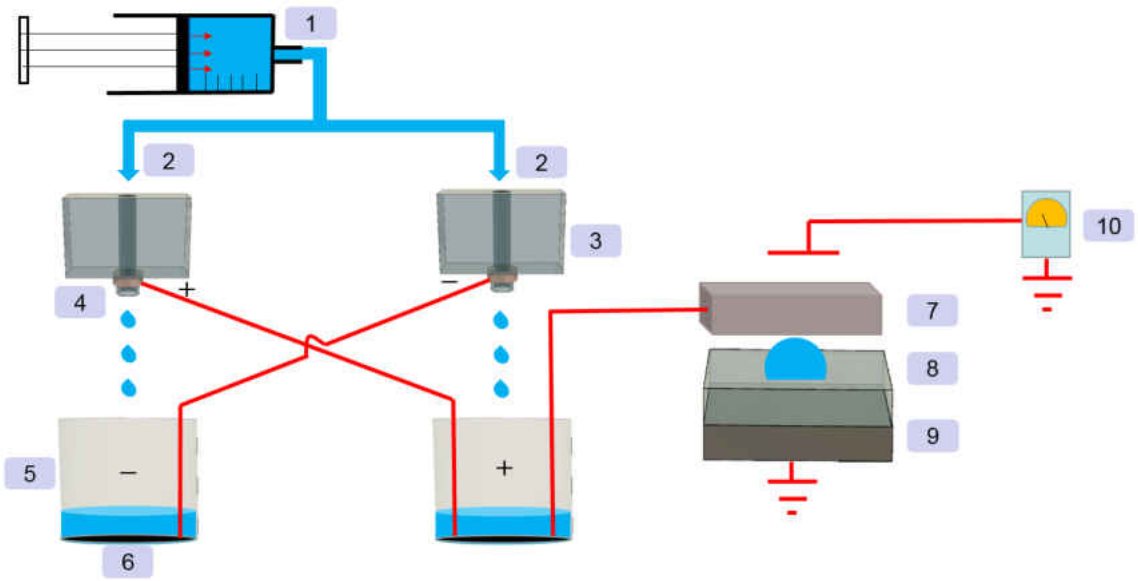

1	2	3	4	5	6	7	8	9	10
Syringe Pump	Water	Microtube	Cu ring	Plastic beaker	Al foil	Ti Pellet	PDMS	Ti Pellet	Electrostatic voltmeter

Fig. 56. Schematic diagram of contactless electrowetting using the MKWD.

CHAPTER 3

RESULTS

3.1 Performance Evaluation of the MKWDs

The performance of the MKWDs was evaluated to identify the optimized operating conditions with the highest voltage for use in electrowetting. Fig. 57 shows the outputs of the MKWDs with two different tube diameters using various flow rates. The duration of each experiment depends on the volumetric capacity of the syringe pump and the flow rate. Higher flow rate drains the syringe much faster. In practice, the output can be sustained using a recycle pump. The current study, however, aims only to evaluate the feasibility of electrowetting by MKWD for next step. Fig. 57 only shows the data collected from the negative electrodes of MKWDs. Two phenomena were observed from the experiments.

First, for both MKWDs, the output voltages increased as the flow rate increased. The charge collectors in the MKWD can be considered as a capacitor. Therefore, in the experiments, higher flow rate led to larger charging current and faster charging rate. As a result, higher voltage gain and shorter charging time were achieved. Second, the output voltages plateaued at certain voltage levels. As voltage goes up, charge leakage becomes more and more significant. The output voltage can only reach a point where the leaking current counters the charging current. It means that the net gain of charges vanishes and therefore the output voltage remains constant. The highest output voltages from both MKWDs were obtained with the highest flow rates at 12.5 ml/min and 50 ml/min, respectively. The maximum voltage recorded was around -7700V, which was obtained from the MKWD with smaller ID (254 μm) at 12.5ml/min. Since, the number of the water droplet depends on the size of the diameter of the tube [128]. Moreover, each droplet contains charges. Thus, a smaller size of diameter can generate higher voltage than a bigger tube. Another reason

can be mentioned that for electrostatic sprays, larger flow rate results in much larger droplet size, and thus may cause less amount of charge carriers [129].

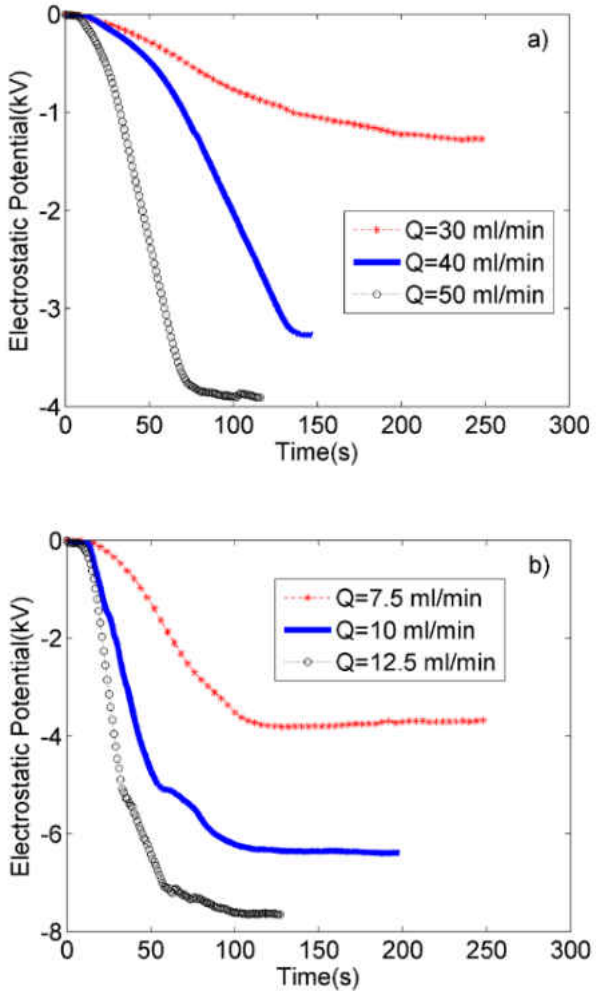

Fig. 57. Output voltages of the negative electrodes of two MKWDs over a period up to 250 seconds. a) and b) represent the results from the MKWDs that have tube IDs of 508 μm and 254 μm, respectively. The calculated flow speeds were 2.517 (red), 3.356 (blue), and 4.195 (black) m/s, respectively for both MKWDs.

It is seen that charge leakage becomes a dominating factor that limits the ultimate output voltage of the MKWD. Ambient humid air and the insulating materials are the main reasons for

charge leakage. Water vapor in the air has a tendency to remove charges from objects. Higher humidity means higher water content in the air, which results in an increase of its electrical conductivity, making discharging easier [130]. This is why, for example, people usually observe electrostatic sparks or shocks in winter, because the humidity reaches its lowest level in winter, which enables more charge buildup. The insulating materials and their thickness also affect the voltage output. Although the Ohmic resistance of an insulator is high, the leaking current may become significant if the voltage increases to a great level. In addition, if the dielectric breakdown of the insulator occurs, it may cause a catastrophic failure of insulation and thus generate an unsteady voltage output. Therefore, in order to obtain a high voltage and stable output, humidity control and appropriate electrical insulation are critical. Specifically, in our experiments, humidity was maintained using an electrical fan and monitored by a humidity meter. Thick layers of liquid electrical tape were used to provide good electrical insulation.

3.2 Contact Electrowetting using the MKWD

After performance evaluation, the MKWD with the smaller microfluidic channel (ID = 254 μm) was selected to supply voltage for conducting electrowetting of DI water droplets on a PDMS substrate. Water droplets on a dielectric substrate will deform under an electric field applied upon. The deformed shape is attributed to several factors, including the strength of electric field, the thickness of the dielectric substrate, the placement of electrodes, and ambient environment that may cause discharge. In the present research, note that the voltage measurements were conducted beneath the counter electrode (Ti pellet) instead of the working electrode (steel needle), where accurately measuring voltage became difficult.

Fig. 58 shows the voltage data (blue line) recorded from the counter electrode during a typical electrowetting test. The dotted line was obtained from curve fitting of the experimental

data to obtain a time-dependent function of voltage for simulation. Eight checkpoints were selected to compare the experimental versus simulation results of the droplet deformation during the electrowetting test.

The left halves of the images in Fig. 59 show the time-lapse images of the electrowetting experiment, corresponding to the eight checkpoints selected. The images were obtained from the frames of a video recorded during the test by AmScope (OMAX A3560U). It is observed that the droplet remained almost unchanged until time passing by point b, after which the deformation became more and more obvious. That was the reason why more checkpoints were selected towards the end. Physically, electrowetting begins when the electric repulsion force starts overcoming the initial surface tension between water and the PDMS substrate. The MWKD was used to charge the water droplet continuously through the steel needle, resulting in a hike of electric repulsion force. The net outcome was that the water droplet kept wetting the PDMS substrate. Another phenomenon observed in most experiments was that the electrowetting process only lasted up to 60 seconds, after which the droplet was ejected out like a bullet (shown in the supplemental video). That was because the cumulative charge imbalance overcame the overall attraction from the PDMS substrate. Even though the needle was carefully placed into the center of the droplet, ejection could hardly be prevented. In real applications, constraints such as a retention wall can be fabricated around the desired wetting area to retain the wetting liquid.

The right halves of the images in Fig. 59 show the CFD simulation results of those eight selected times (shown in Fig. 58). Because the applied voltage for electrowetting was obtained from the MWKD, a time-dependent voltage function was adapted in the simulation, unlike other research using constant voltage values [117]. It is seen that the simulation results closely match the experimental observations. The slight discrepancy between two images at point b was believed

to be caused by the initial tension between the needle and water, which was not considered in the model. In general, the present model well predicted the behaviors of the droplet during electrowetting.

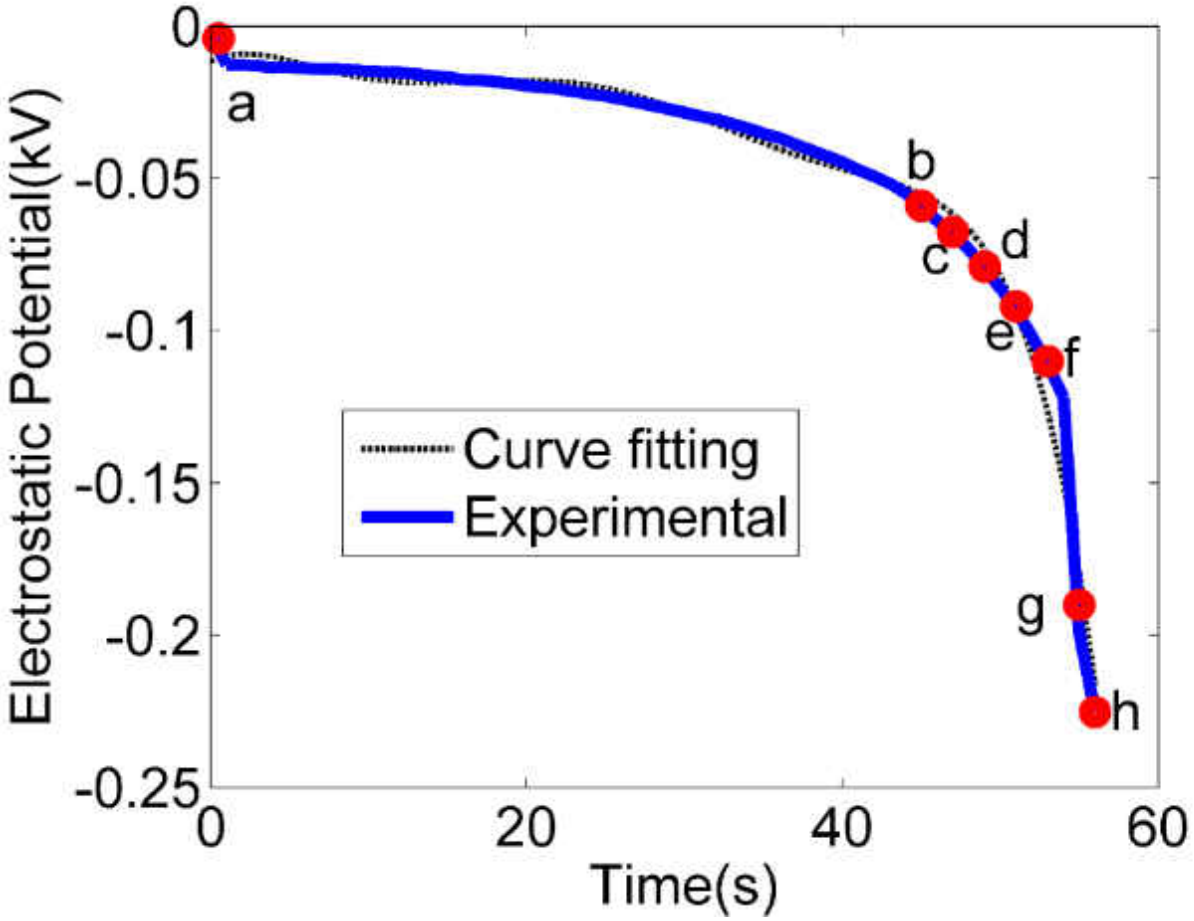

Fig. 58. Voltage measurements (solid blue line) during electrowetting and a curve (dotted black line) that fits the experimental data.

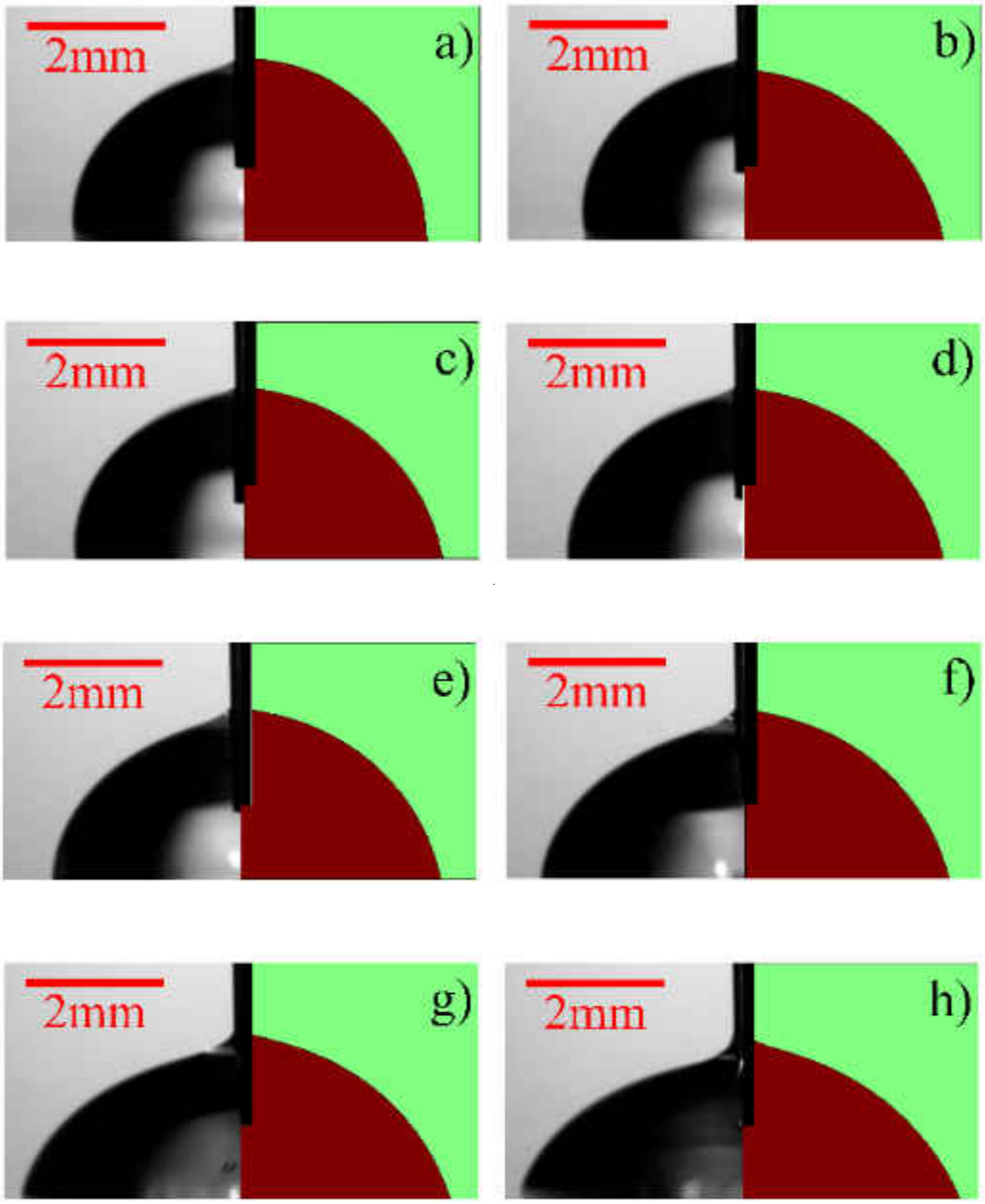

Fig. 59. Comparison of the experimental results (left halves) with the simulated water droplet deformation (right halves) during the electrowetting test shown in Fig. 58.

3.3 Contactless Electrowetting using the MKWD

The MKWD generates the electrostatic voltage as shown in A curve fitting in experiment data (dash line) is estimated by Matlab to use for voltage variation respect to time in the simulation in COMSOL 5.1. The voltage increase with injecting the DI water with the flow rate of 12.5 ml/min by the syringe pump. At the beginning of the flow, the voltage is zero because of no existence of ions on the collectors. By injecting more DI water, more ions are obtained via the configuration of the MKWD system, which is a positive feedback loop; therefore, more voltage will be generated. The injection in MKED is stopped when the amount of voltage is the water droplet collapses suddenly in electrowetting as shown in zoom in Fig. 60.

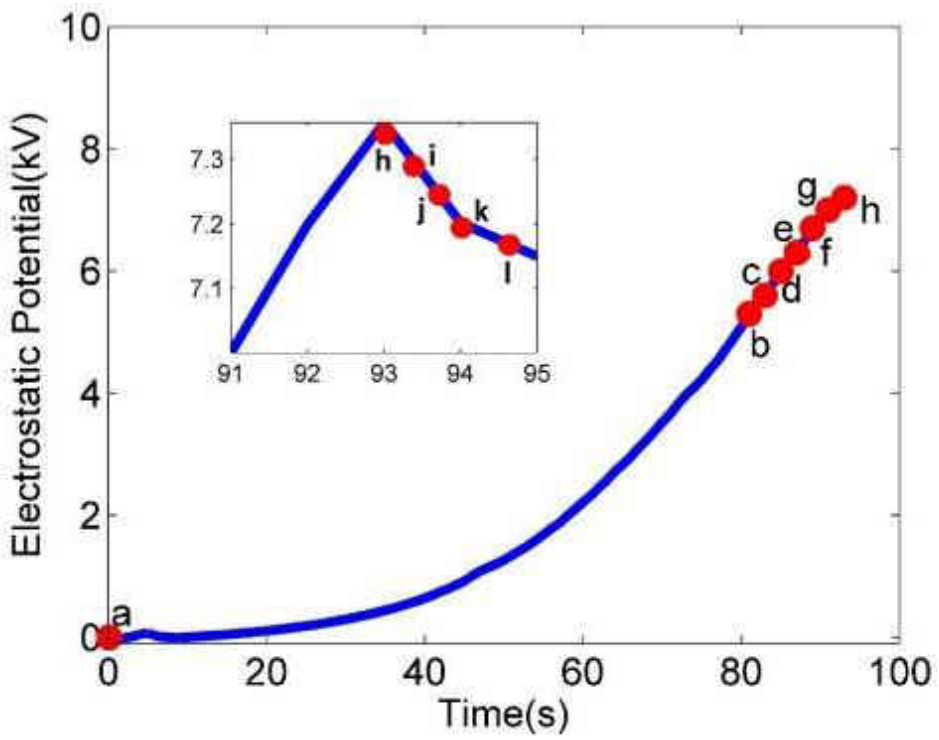

Fig. 60. Voltage variation in MKWD with the flow rate of 12.5 ml/min in the experiment.

To show the effect of the voltage that MKWD generated, eight points from point a to h are considered as a first step with 4 points from i to l as a second step (zoomed in the diagram in Fig. 60); then, different shapes of the droplets in these twelve points of electrowetting are defined as shown in Fig. 60. As shown in Fig. 61, in the first step, when the voltage is zero, the shape of the droplet is stable. When the voltage reaches around 5000V, the shape of the droplet in electrowetting begins to change; increasing the voltage from point a to point b can affect a change on the droplet because the amount of surface tension of liquid-gas is enough to start deforming the droplet. Between point b and point c, the shape of the water droplet reforms gradually. Then, the shape of the droplet deforms until point h; at point h, the water droplet deforms to the highest degree. The high degree of deformation can have a great improvement in MEMS applications, especially in an optical application [131]. In the second step, high enough voltage leads to ionization of the air around the water droplet; then, the charges go inside of the droplet. Therefore, the contact angle of water droplet can be affected by charges inside the water droplet in a short time. This scenario causes the droplet to collapse in a short period of time. Charges start transferring inside the droplet between the points h and i; then, the droplet collapses at point j. At point k, the droplet has the minimum collapse; between point k and l, the water droplet will have a stable size.

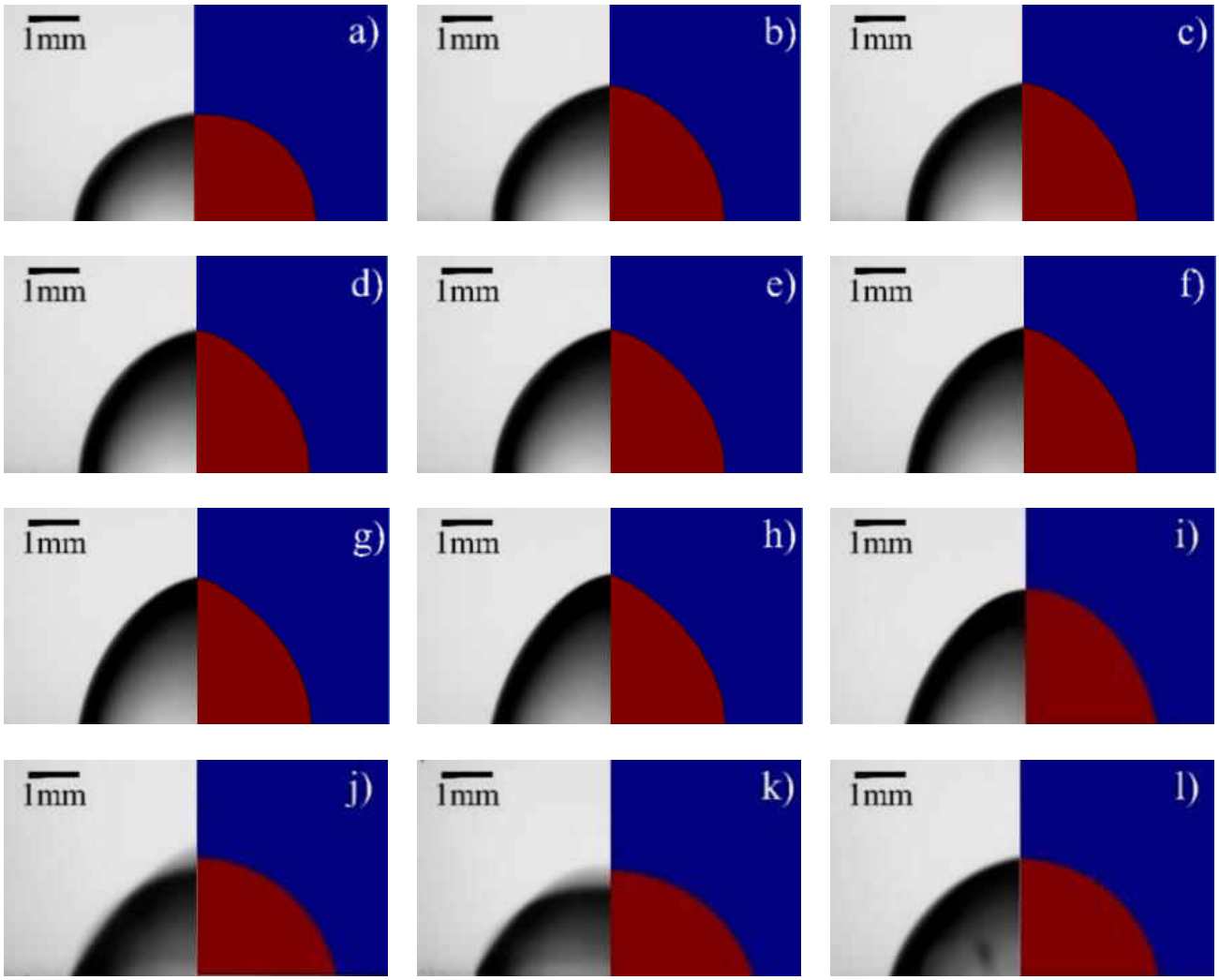

Fig. 61. Affecting high voltage on the deformation of the droplet without contacting the electrode with water droplet at electrowetting.

Regarding the strong agreement between simulation and experimental results, the amount of deformation of the water droplet with different electrical thickness is investigated. The different thicknesses can demonstrate that the thickness of the dielectrics can be introduced as a parameter to control the water droplet deformation. The amount of deformation depends on the thickness of the dielectric, which is shown in Fig. 62. The deformation of the droplet while the same voltage is applied for various thickness of the dielectric of PDMS. This amount is not high; however, the

deformation in the graph refers that the amount of deformation is controlled by the thickness of the dielectric.

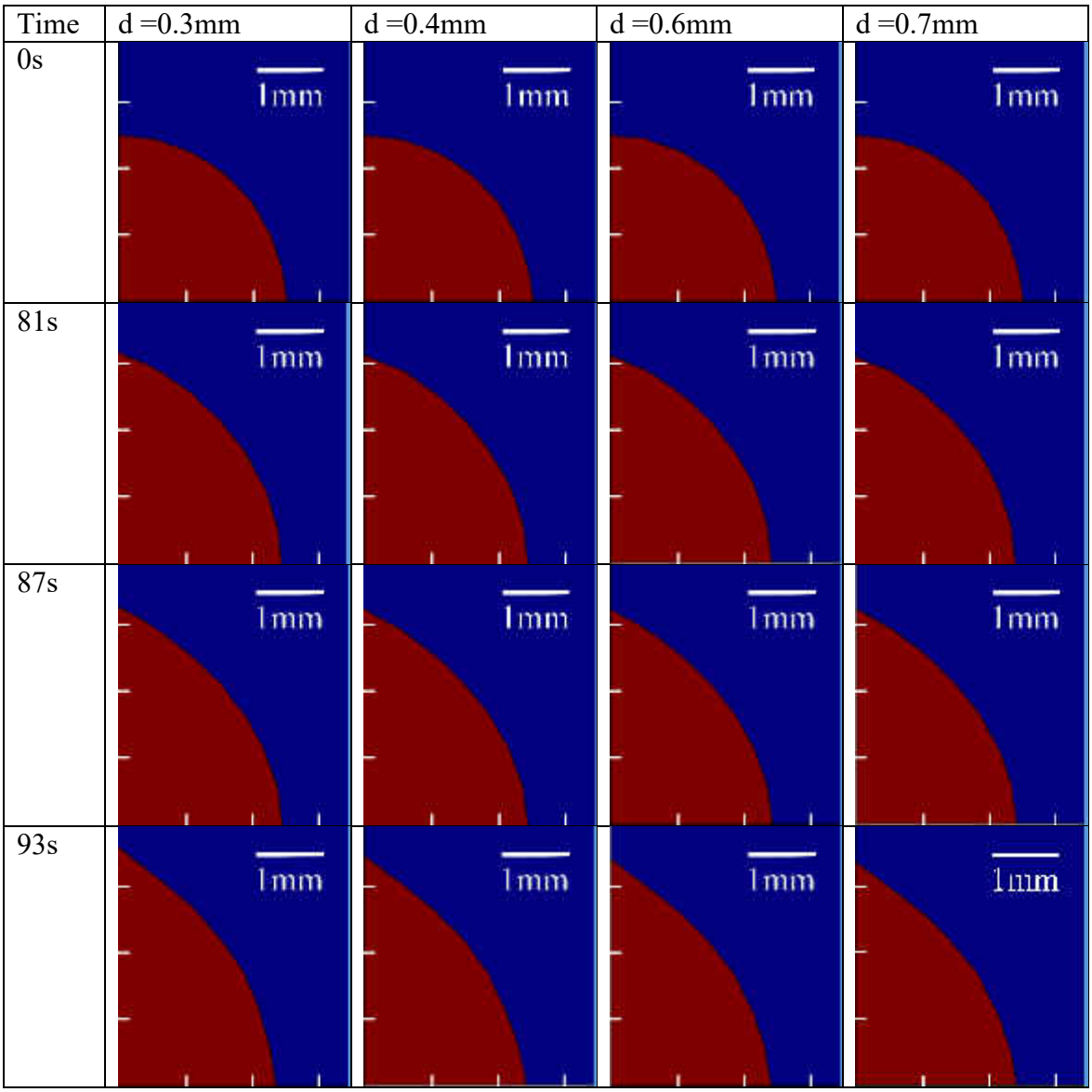

Fig. 62. The deformation of the droplet while the same voltage is applied for various thickness of the dielectric of PDMS.

To find out the possibility of controlling the wettability of the surface without contacting the electrode with the water droplet by the flow rate of MKWD, three various flow rates of the MKWD

are considered. The experiment carried out at the temperature of the ambient temperature of 24 °C and humidity of 65±3. In Fig. 63, the flow rate of 12.5 ml/min from MKWD is considered, and at the point a, the voltage is applied to the contactless electrowetting. The amount of charge that is transferred inside the voltage is calculated by the difference in the amount of the voltages between point c and point a. The distance between the top and bottom electrodes are 3.4mm, and the DI water droplet volume was 10 μlit. Additionally, the bottom electrode is connected to the earth. The amount of the voltage applied causes that the droplet to rise up under the influence of the created electric filed. At the point of b, the air will be ionized. The charge goes into the droplet and increases the amount of charge inside the droplet and affects the contact angle. The wettability of the water droplet at point b will be increase by this method.

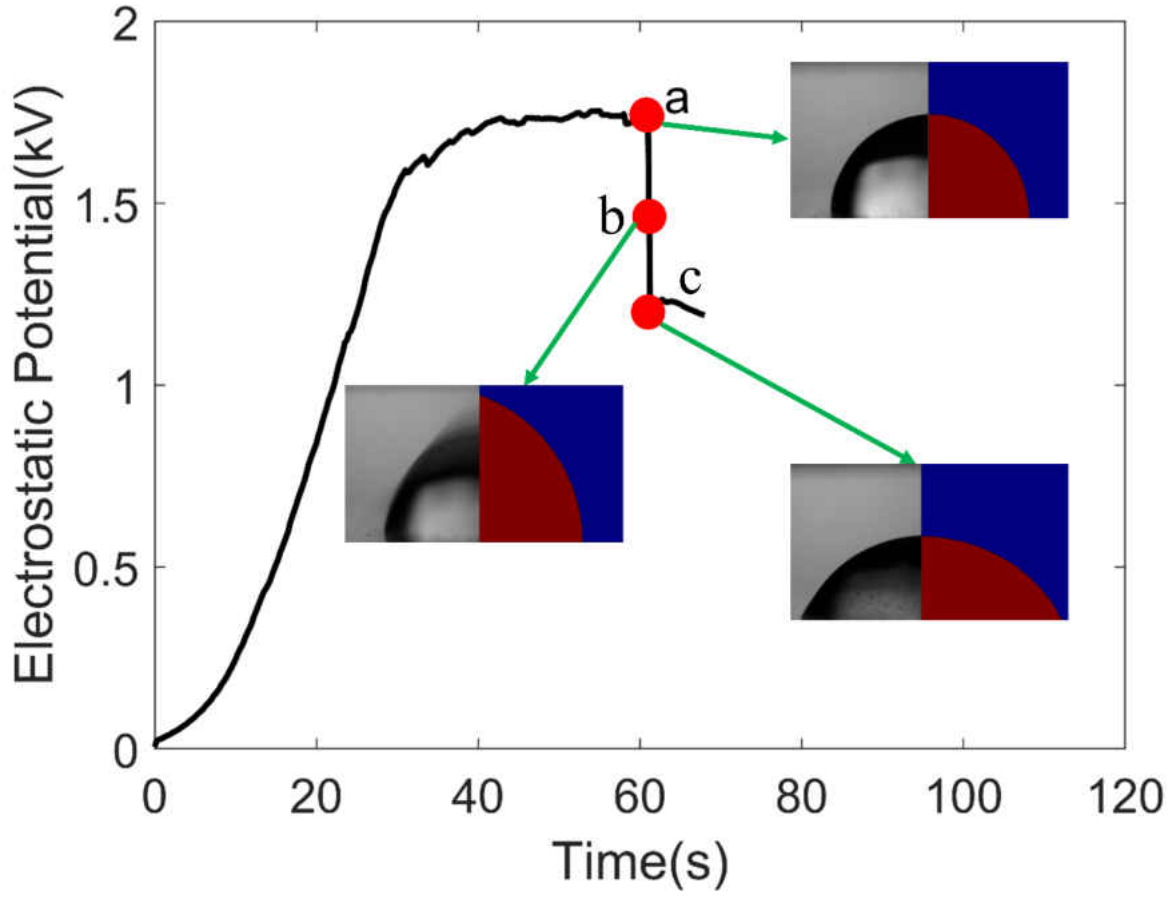

Fig. 63. Contactless electrowetting by the use of the flow rate of 12.5 ml/min in MKWD and applying voltage at the point a and wettability at the point b.

As shown in Fig. 64, the same condition of an experiment by the different flow rate (10 ml/min) of MKWD is carried out to show the controlling the amount of contact angle. The amount of contact angle at the end is less than the electrowetting at the flow rate of 12.5 ml/min in MKWD. The reason is due to the number of charges that are transferred to the droplet.

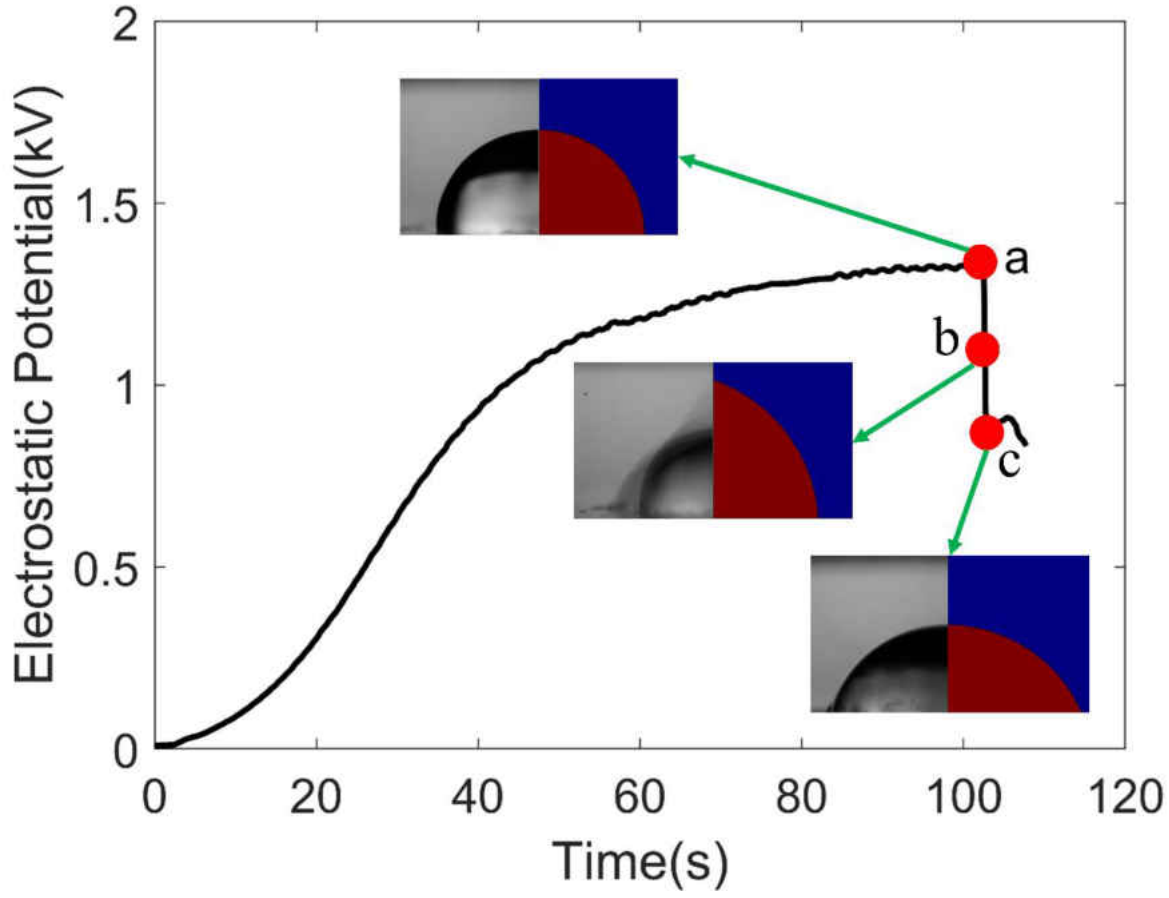

Fig. 64. Contactless electrowetting by the use of the flow rate of 10 ml/min in MKWD and applying voltage at the point a and wettability at the point b.

The amount of voltage that was generated by the MKWD at the flow rate of 7.5 ml/min in Fig. 65 is less than 10 and 12.5 ml/min due to the number of droplets that MKWD created and also the size of the droplets that are created. The amount of contact angle is lower than the MKWD flow rates of 12 and 10. Hence, we can conclude the contact angle depends on the flow rates of the MKWD because in lower voltage is generated by lower flow rate.

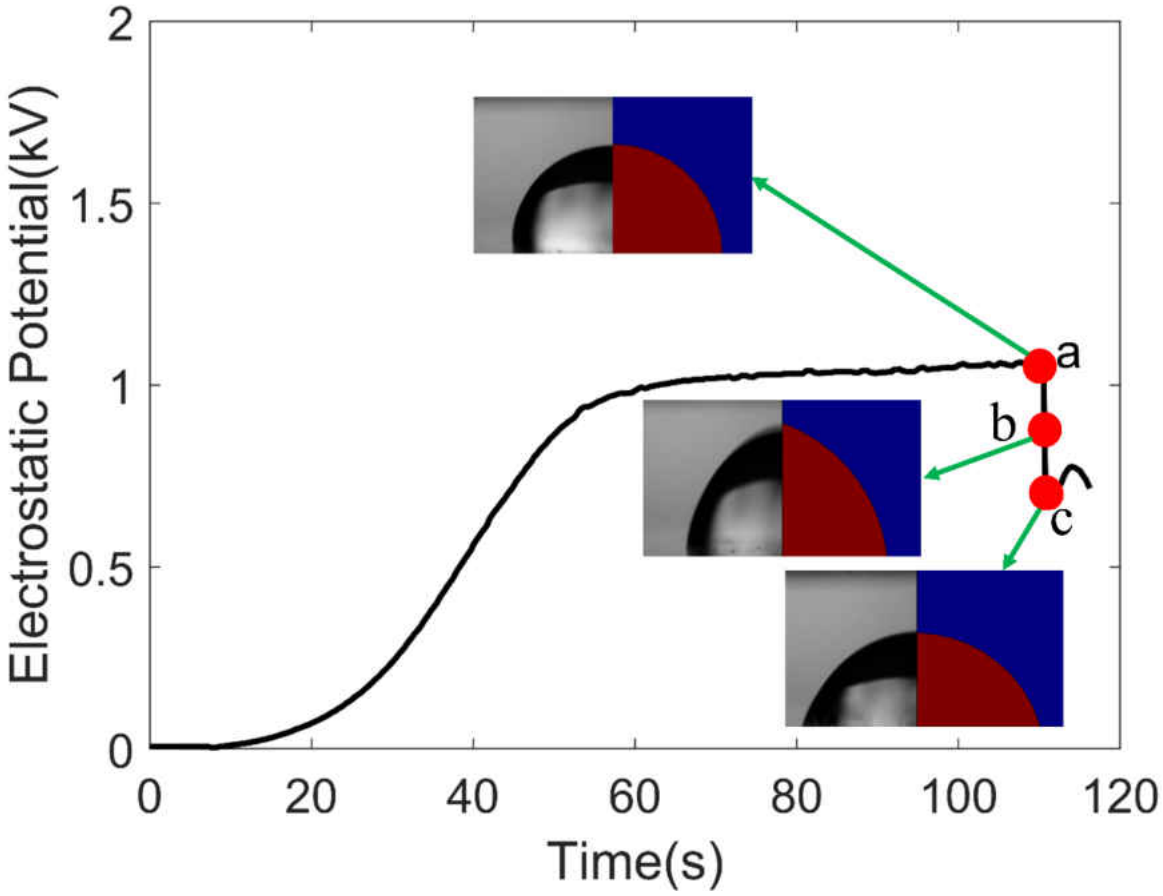

Fig. 65. Contactless electrowetting by the use of the flow rate of 7.5 ml/min in MKWD and applying voltage at the point a and wettability at the point b.

CHAPTER 4

CONCLUSIONS AND FUTURE RESEARCH

4.1 Microfluidic Kelvin Water Dropper

A Microfluidic Kelvin water dropper was built in a lab to evaluate its feasibility to use in electrowetting. Stable voltage outputs were obtained from the homemade MKWDs. The highest voltage recorded was 7700 V, which was obtained from the negative electrode of one MKWD that has two 254μm ID microchannels. The best performing MKWD was then used to conduct electrowetting tests. The future research can be mentioned controlling more on the voltage based on the flow rates.

4.2 MKWD for Contact electrowetting

A combined analytical and experimental investigation was performed to characterize the droplet deformation during electrowetting. It was demonstrated that MWKD is indeed a feasible and low-cost electrowetting method. Furthermore, the experimental observations were well predicted by the numerical model presented in this paper. For future applications, electrowetting using MKWDs can be further optimized by environmental control (e.g. humidity, temperature), microfluidic flow management, and voltage output control.

4.3 MKWD for Contactless electrowetting

The investigation of a practical Microfluidic Kelvin Dropper, which generates a voltage to create an electric field for water droplet in electrowetting, has been demonstrated experimentally and analytically in this work. Linking the electrowetting and high voltage generated in Microfluidic Kelvin Water Dropper is widespread range of applications that affect new technology. In the first experiment, the result shows that the effect of the voltage generated by

microfluidic Kelvin dropper on the contactless electrodes with a water droplet in the electrowetting; then electric field generated can effect on charge inside the droplet and impact on the surface tension of the droplet. The change of the droplet shape in the experimental part during exposure to an electric field matches with the simulation. When the voltage generated by MKWD increases, the shape of the droplet will rise up; then, after being close enough to the top electrode, the air will be ionized that charges transfer to the water droplet. Charges inside the water droplet lead to sudden collapse. In the simulation, by considering the lower thickness of dielectric in the contactless electrowetting, the droplet raised more due to the electric field created by same voltage. In the second experiment, the voltage from the MKWD is applied to the contactless while it is stable. The amount of the contact angle for the water droplet with the volume of 10 μlit was constant then decreased immediately; the MKWD generated electrostatic charge by the flow rate of 12.5, and the lowest amount is 7.5 ml/min.

REFERENCES

1.Ehrenberg, W.; Spear, W. An electrostatic focusing system and its application to a fine focus x-ray tube. *Proceedings of the Physical Society. Section B* **1951**, *64*, 67.

2.Leiyun, H.W.W. Application study on high-voltage electrostatic field in food sterilization [j]. *Food and Machinery* **2001**, *4*, 003.

3.Tuve, M.; Hafstad, L.; Dahl, O. High voltage technique for nuclear physics studies. *Physical Review* **1935**, *48*, 315.

4.Møller, S.P. Elisa, and electrostatic storage ring for atomic physics. *Nuclear Instruments and Methods in Physics Research Section A: Accelerators, Spectrometers, Detectors and Associated Equipment* **1997**, *394*, 281-286.

5.Layland, M. In *Generalised electrostatic-machine theory*, Proceedings of the Institution of Electrical Engineers, 1969; IET: pp 403-405.

6.Holtz, W. Ueber eine neue elektrisirmaschine. *Annalen der Physik* **1865**, *202*, 157-171.

7.Gaćanović, M. In *Electrostatic application principles*, Proceeding of the International PhD Seminar on Computational electromagnetics and optimization in electrical engineering CEMOEE, 2010; pp 10-13.

8.Van de Graaff, R.; Trump, J.; Buechner, W. Electrostatic generators for the acceleration of charged particles. *Reports on Progress in Physics* **1948**, *11*, 1.

9.Fan, F.-R.; Tian, Z.-Q.; Wang, Z.L. Flexible triboelectric generator. *Nano Energy* **2012**, *1*, 328-334.

10. Fan, F.-R.; Lin, L.; Zhu, G.; Wu, W.; Zhang, R.; Wang, Z.L. Transparent triboelectric nanogenerators and self-powered pressure sensors based on micropatterned plastic films. *Nano letters* **2012**, *12*, 3109-3114.

11. Wang, Z.L. Triboelectric nanogenerators as new energy technology for self-powered systems and as active mechanical and chemical sensors. *ACS nano* **2013**, *7*, 9533-9557.

12. Wang, S.; Lin, L.; Wang, Z.L. Nanoscale triboelectric-effect-enabled energy conversion for sustainably powering portable electronics. *Nano letters* **2012**, *12*, 6339-6346.

13. Yang, J.; Chen, J.; Yang, Y.; Zhang, H.; Yang, W.; Bai, P.; Su, Y.; Wang, Z.L. Broadband vibrational energy harvesting based on a triboelectric nanogenerator. *Advanced Energy Materials* **2014**, *4*.

14. Thomson, W. Xvi. On a self-acting apparatus for multiplying and maintaining electric charges, with applications to illustrate the voltaic theory. *Proceedings of the Royal Society of London* **1868**, *16*, 67-72.

15. Chree, C. Atmospheric electricity in egypt. *Nature* **1910**, *82*, 379-379.

16. Chree, C. Water-droppers and radium collectors. *Nature* **1904**, *70*, 630.

17. Sanford, F. On the formation of negatively electrified rain drops. *Physical Review* **1918**, *11*, 445.

18. Elster, J.; Geitel, H. 0ber die existenz elektrischer ionen in der atmosphar. *Phys. Z* **1899**, *1*, 245.

19. Harrison, R.G. Long-term measurements of the global atmospheric electric circuit at eskdalemuir, scotland, 1911–1981. *Atmospheric Research* **2004**, *70*, 1-19.

20. Pollack, G.H. Water, energy and life: Fresh views from the water's edge. *International Journal of Design & Nature and Ecodynamics: A transdisciplinary Journal Relating to Nature, Science and th eHumanities* **2010**, *5*, 27.

21. Harrison, R. Twentieth-century atmospheric electrical measurements at the observatories of kew, eskdalemuir and lerwick. *Weather* **2003**, *58*, 11-19.

22. King, S.A. Investigation of climate effects on the global atmospheric electrical circuit using surface potential gradient data. **2004**.

23. Loeb, L.B. The generation of static charges by processes involving ionization of gases. In *Static Electrification*, Springer: 1958; pp 201-224.

24. Evans, L.; Stevens, J.T. Kelvin water dropper revisited. *The Physics Teacher* **1977**, *15*, 548-549.

25. Sady, M. The kelvin water dropper: An elementary experience. *The Physics Teacher* **1984**, *22*, 516-516.

26. Euerle, W.C. Polyphase alternating current generator. Google Patents: 1971.

27. Zahn, M. Self-excited ac high voltage generation using water droplets. *American Journal of Physics* **1973**, *41*, 196-202.

28. Planinšič, G.; Prosen, T. Conducting rod on the axis of a charged ring: The kelvin water drop generator. *American Journal of Physics* **2000**, *68*, 1084-1089.

29. Milne-Thomson, L.M.; Abramowitz, M.; Stegun, I. Handbook of mathematical functions. *Handbook of Mathematical Functions* **1972**.

30. Frohn, A.; Roth, N. *Dynamics of droplets*. Springer Science & Business Media: 2000.

31. Ovchinnikova, K.; Pollack, G.H. Can water store charge? *Langmuir* **2008**, *25*, 542-547.

32. Garg, S.; Shastri, R.; Sivasankaran, B.; Rani, L.; Kaila, B.K.; Singh, N. The kelvin water dropper: Converting a physics toy into an educational device. *arXiv preprint arXiv:1707.06861* **2017**.

33. Jonas, L.A.; Steel, J.S. *Energy fields for fire extinguishment*; Hughes Associates, Inc: Wheaton, MD: **1990**.

34. Liu, L.W.; Chen, Y.; Zhang, Q. In *Wireless energy harvesting using a negatively charged uv antenna*, Applied Computational Electromagnetics Society Symposium (ACES), 2017 International, 2017; IEEE: pp 1-2.

35. Liu, L.W.Y. Harvesting atmospheric ions using surface electromagnetic wave technologies. *Advances in Technology Innovation* **2017**, *2*, 99-104.

36. Rahi, G. Positive ion poisoning.

37. Huang, H.-F. Voltage build-up time responses of kelvin's water droplet generator: Variations due to different geometric configurations. *Journal of Electrostatics* **2014**, *72*, 447-456.

38. Zahn, M. Electromagnetic field theory: A problem solving approach. **1979**.

39. Woodson, H.H.; Melcher, J.R. Electromechanical dynamics, part i: Discrete systems, part ii: Field, forces and motion, part iii: Elastic and fluid media. John Wiley and Sons: 1968.

40. Eijkel, J.C.; Van Den Berg, A.; Xie, Y. In *Ballistic energy conversion*, Solid-State Sensors, Actuators and Microsystems (TRANSDUCERS), 2017 19th International Conference on, 2017; IEEE: pp 110-114.

41. Knapen, T. Analyzing and optimally controlling the kelvin water dropper. University of Twente, 2015.

42. Marín, Á.G.; van Hoeve, W.; García-Sánchez, P.; Shui, L.; Xie, Y.; Fontelos, M.A.; Eijkel, J.C.; van den Berg, A.; Lohse, D. The microfluidic kelvin water dropper. *Lab on a chip* **2013**, *13*, 4503-4506.

43. Cardott, J.N.; Duckett, L.D.; Stewart, C.C. Electrostatic deceleration system for flow cytometer. Google Patents: 2001.

44. Lin, Y.-H.; Lee, G.-B.; Li, C.-W.; Huang, G.-R.; Chen, S.-H. Flow-through sampling for electrophoresis-based microfluidic chips using hydrodynamic pumping. *Journal of Chromatography A* **2001**, *937*, 115-125.

45. Dorfman, K.D. DNA electrophoresis in microfluidic post arrays under moderate electric fields. *Physical Review E* **2006**, *73*, 061922.

46. Lee, J.; Moon, H.; Fowler, J.; Schoellhammer, T.; Kim, C.-J. Electrowetting and electrowetting-on-dielectric for microscale liquid handling. *Sensors and Actuators A: Physical* **2002**, *95*, 259-268.

47. Berge, B. Electrocapillarity and wetting of insulator films by water. *Comptes Rendus De L Academie Des Sciences Serie Ii* **1993**, *317*, 157-163.

48. Lee, J.; Kim, C.-J. Surface-tension-driven microactuation based on continuous electrowetting. *Journal of Microelectromechanical Systems* **2000**, *9*, 171-180.

49. Pollack, M.G.; Fair, R.B.; Shenderov, A.D. Electrowetting-based actuation of liquid droplets for microfluidic applications. *Applied Physics Letters* **2000**, *77*, 1725-1726.

50. Lippmann, G. Relations entre les phénomènes électriques et capillaires. Gauthier-Villars, 1875.

51. Beni, G.; Hackwood, S.; Jackel, J. Continuous electrowetting effect. *Applied physics letters* **1982**, *40*, 912-914.

52. Beni, G.; Hackwood, S. Electro-wetting displays. *Applied Physics Letters* **1981**, *38*, 207-209.

53. Nelson, W.C.; Kim, C.-J.C. Droplet actuation by electrowetting-on-dielectric (ewod): A review. *Journal of Adhesion Science and Technology* **2012**, *26*, 1747-1771.

54. Zhao, Y. and Wang, Y. Fundamentals and applications of electrowetting: A critical review. **2013**.

55. Zhao, Y.-P.; Wang, Y. Fundamentals and applications of electrowetting. *Reviews of Adhesion and Adhesives* **2013**, *1*, 114-174.

56. Mugele, F. Fundamental challenges in electrowetting: From equilibrium shapes to contact angle saturation and drop dynamics. *Soft Matter* **2009**, *5*, 3377-3384.

57. Caputo, D.; de Cesare, G.; Vecchio, N.L.; Nascetti, A.; Parisi, E.; Scipinotti, R. Polydimethylsiloxane material as hydrophobic and insulating layer in electrowetting-on-dielectric systems. *Microelectronics Journal* **2014**, *45*, 1684-1690.

58. Fair, R.B.; Khlystov, A.; Tailor, T.D.; Ivanov, V.; Evans, R.D.; Srinivasan, V.; Pamula, V.K.; Pollack, M.G.; Griffin, P.B.; Zhou, J. Chemical and biological applications of digital-microfluidic devices. *IEEE Design & Test of Computers* **2007**, *24*.

59. Hayes, R.A.; Feenstra, B.J. Video-speed electronic paper based on electrowetting. *Nature* **2003**, *425*, 383.

60. You, H.; Steckl, A. Three-color electrowetting display device for electronic paper. *Applied physics letters* **2010**, *97*, 023514.

61. Kim, D.Y.; Steckl, A.J. Electrowetting on paper for electronic paper display. *ACS applied materials & interfaces* **2010**, *2*, 3318-3323.

62. Jacobson, J.M.; Whitesides, T.H.; McCreary, M.D.; Paolini Jr, R.J. Electro-wetting displays. Google Patents: 2008.

63. Hendriks, B.; Kuiper, S.; As, M.V.; Renders, C.; Tukker, T. Electrowetting-based variable-focus lens for miniature systems. *Optical review* **2005**, *12*, 255-259.

64. Kuiper, S.; Hendriks, B. Variable-focus liquid lens for miniature cameras. *Applied physics letters* **2004**, *85*, 1128-1130.

65. Preston, D.J.; Anders, A.; Barabadi, B.; Tio, E.; Zhu, Y.; Dai, D.A.; Wang, E.N. In *Electrowetting-on-dielectric actuation of a spatial and angular manipulation mems stage*,

Micro Electro Mechanical Systems (MEMS), 2017 IEEE 30th International Conference on, 2017; IEEE: pp 769-772.

66. Cho, S.K.; Moon, H.; Kim, C.-J. Creating, transporting, cutting, and merging liquid droplets by electrowetting-based actuation for digital microfluidic circuits. *Journal of microelectromechanical systems* **2003**, *12*, 70-80.

67. Krupenkin, T.; Yang, S.; Mach, P. Tunable liquid microlens. *Applied Physics Letters* **2003**, *82*, 316-318.

68. Kroupenkine, T.N.; Yang, S. Tunable liquid microlens. Google Patents: 2003.

69. Hua, Z.; Rouse, J.L.; Eckhardt, A.E.; Srinivasan, V.; Pamula, V.K.; Schell, W.A.; Benton, J.L.; Mitchell, T.G.; Pollack, M.G. Multiplexed real-time polymerase chain reaction on a digital microfluidic platform. *Analytical chemistry* **2010**, *82*, 2310-2316.

70. Sista, R.; Hua, Z.; Thwar, P.; Sudarsan, A.; Srinivasan, V.; Eckhardt, A.; Pollack, M.; Pamula, V. Development of a digital microfluidic platform for point of care testing. *Lab on a Chip* **2008**, *8*, 2091-2104.

71. Luk, V.N.; Wheeler, A.R. A digital microfluidic approach to proteomic sample processing. *Analytical chemistry* **2009**, *81*, 4524-4530.

72. Dhull, R.K. *A two degrees-of-freedom (dof) scanning micromirror using thermocapillary effect in microdroplets*. Rochester Institute of Technology: 2010.

73. Sen, P.; Kim, C.-J. A fast liquid-metal droplet microswitch using ewod-driven contact-line sliding. *Journal of Microelectromechanical Systems* **2009**, *18*, 174-185.

74. Nelson, W.C.; Kavehpour, H.P. A miniature capillary breakup extensional rheometer by electrostatically assisted generation of liquid filaments. *Lab on a Chip* **2011**, *11*, 2424-2431.

75. Gong, J.; Cha, G.; Ju, Y.S. In *Thermal switches based on coplanar ewod for satellite thermal control*, Micro Electro Mechanical Systems, 2008. MEMS 2008. IEEE 21st International Conference on, 2008; IEEE: pp 848-851.

76. Banpurkar, A.G.; Nichols, K.P.; Mugele, F. Electrowetting-based microdrop tensiometer. *Langmuir* **2008**, *24*, 10549-10551.

77. Bratsch, S.G. Standard electrode potentials and temperature coefficients in water at 298.15 k. *Journal of Physical and Chemical Reference Data* **1989**, *18*, 1-21.

78. Baret, J.-C.; Mugele, F. Electrical discharge in capillary breakup: Controlling the charge of a droplet. *Physical review letters* **2006**, *96*, 016106.

79. Jones, T.B. On the relationship of dielectrophoresis and electrowetting. *Langmuir* **2002**, *18*, 4437-4443.

80. Kang, K.H. How electrostatic fields change contact angle in electrowetting. *Langmuir* **2002**, *18*, 10318-10322.

81. Jones, T.B.; Fowler, J.D.; Chang, Y.S.; Kim, C.-J. Frequency-based relationship of electrowetting and dielectrophoretic liquid microactuation. *Langmuir* **2003**, *19*, 7646-7651.

82. Wang, Y.; Zhao, Y.-P. Electrowetting on curved surfaces. *Soft Matter* **2012**, *8*, 2599-2606.

83. Blake, T.D. The physics of moving wetting lines. *Journal of colloid and interface science* **2006**, *299*, 1-13.

84. De Ruijter, M.J.; De Coninck, J.; Blake, T.; Clarke, A.; Rankin, A. Contact angle relaxation during the spreading of partially wetting drops. *Langmuir* **1997**, *13*, 7293-7298.

85. Hoffman, R.L. A study of the advancing interface. I. Interface shape in liquid—gas systems. *Journal of colloid and interface science* **1975**, *50*, 228-241.

86. Moon, H.; Cho, S.K.; Garrell, R.L.; Kim, C.-J.C. Low voltage electrowetting-on-dielectric. *Journal of applied physics* **2002**, *92*, 4080-4087.

87. Dai, W.; Zhao, Y.-P. The nonlinear phenomena of thin polydimethylsiloxane (pdms) films in electrowetting. *International Journal of Nonlinear Sciences and Numerical Simulation* **2007**, *8*, 519-526.

88. Moghaddam, M.S.; Latifi, H.; Shahraki, H.; Cheri, M.S. Simulation, fabrication, and characterization of a tunable electrowetting-based lens with a wedge-shaped pdms dielectric layer. *Applied optics* **2015**, *54*, 3010-3017.

89. Gerratt, A.P.; Bergbreiter, S. Dielectric breakdown of pdms thin films. *Journal of Micromechanics and Microengineering* **2013**, *23*, 067001.

90. Srinivasan, V.; Pamula, V.K.; Fair, R.B. Droplet-based microfluidic lab-on-a-chip for glucose detection. *Analytica Chimica Acta* **2004**, *507*, 145-150.

91. Srinivasan, V.; Pamula, V.K.; Fair, R.B. An integrated digital microfluidic lab-on-a-chip for clinical diagnostics on human physiological fluids. *Lab on a Chip* **2004**, *4*, 310-315.

92. Banerjee, A.; Kreit, E.; Liu, Y.; Heikenfeld, J.; Papautsky, I. Reconfigurable virtual electrowetting channels. *Lab on a Chip* **2012**, *12*, 758-764.

93. Mugele, F.; Buehrle, J. Equilibrium drop surface profiles in electric fields. *Journal of Physics: Condensed Matter* **2007**, *19*, 375112.

94. Gupta, R.; Olivier, G.K.; Frechette, J. Invariance of the solid− liquid interfacial energy in electrowetting probed via capillary condensation. *Langmuir* **2010**, *26*, 11946-11950.

95. Saeki, F.; Baum, J.; Moon, H.; Yoon, J.-Y.; Kim, C.; Garrell, R. Electrowetting on dielectrics (ewod): Reducing voltage requirements for microfluidics. *Polym. Mater. Sci. Eng* **2001**, *85*, 12-13.

96. Virgilio, V.D. Contactless electrowetting. **2015**.

97. Castañer, L.; Di Virgilio, V.; Bermejo, S. Charge-coupled transient model for electrowetting. *Langmuir* **2010**, *26*, 16178-16185.

98. Basaran, O.A.; Scriven, L. Axisymmetric shapes and stability of pendant and sessile drops in an electric field. *Journal of colloid and interface science* **1990**, *140*, 10-30.

99. Bateni, A.; Laughton, S.; Tavana, H.; Susnar, S.; Amirfazli, A.; Neumann, A. Effect of electric fields on contact angle and surface tension of drops. *Journal of colloid and interface science* **2005**, *283*, 215-222.

100. Daub, C.D.; Bratko, D.; Leung, K.; Luzar, A. Electrowetting at the nanoscale. *The Journal of Physical Chemistry C* **2007**, *111*, 505-509.

101. Daub, C.D.; Bratko, D.; Luzar, A. Electric control of wetting by salty nanodrops: Molecular dynamics simulations. *The Journal of Physical Chemistry C* **2011**, *115*, 22393-22399.

102. Picknett, R.; Bexon, R. The evaporation of sessile or pendant drops in still air. *Journal of Colloid and Interface Science* **1977**, *61*, 336-350.

103. Sobac, B.; Brutin, D. Triple-line behavior and wettability controlled by nanocoated substrates: Influence on sessile drop evaporation. *Langmuir* **2011**, *27*, 14999-15007.

104. Semenov, S.; Starov, V.; Rubio, R.; Agogo, H.; Velarde, M. Evaporation of sessile water droplets: Universal behaviour in presence of contact angle hysteresis. *Colloids and Surfaces A: Physicochemical and Engineering Aspects* **2011**, *391*, 135-144.

105. David, S.; Sefiane, K.; Shanahan, M.E. In *On the dynamics of wetting of water-methanol volatile sessile drops on smooth substrates*, Defect and Diffusion Forum, 2006; Trans Tech Publ: pp 469-473.

106. David, S.; Sefiane, K.; Tadrist, L. Experimental investigation of the effect of thermal properties of the substrate in the wetting and evaporation of sessile drops. *Colloids and Surfaces A: Physicochemical and Engineering Aspects* **2007**, *298*, 108-114.

107. Bateni, A.; Susnar, S.; Amirfazli, A.; Neumann, A. Development of a new methodology to study drop shape and surface tension in electric fields. *Langmuir* **2004**, *20*, 7589-7597.

108. Bateni, A.; Amirfazli, A.; Neumann, A. Effects of an electric field on the surface tension of conducting drops. *Colloids and Surfaces A: Physicochemical and Engineering Aspects* **2006**, *289*, 25-38.

109. Bateni, A.; Ababneh, A.; Elliott, J.; Neumann, A.; Amirfazli, A. Effect of gravity and electric field on shape and surface tension of drops. *Advances in Space Research* **2005**, *36*, 64-69.

110. Vancauwenberghe, V.; Di Marco, P.; Brutin, D. Wetting and evaporation of a sessile drop under an external electrical field: A review. *Colloids and Surfaces A: Physicochemical and Engineering Aspects* **2013**, *432*, 50-56.

111. Di Marco, P.; Pedretti, F.; Saccone, G. In *Effect of an external electric field on the shape of a dielectric sessile drop*, 8th World Conference on Experimental Heat Transfer, Fluid Mechanics, and Thermodynamics, 2013; PRT: pp 1-5.

112. Zhao, L.; Adamiak, K. Ehd flow in air produced by electric corona discharge in pin–plate configuration. *Journal of electrostatics* **2005**, *63*, 337-350.

113. Oussalah, N.; Zebboudj, Y. Finite-element analysis of positive and negative corona discharge in wire-to-plane system. *The European Physical Journal-Applied Physics* **2006**, *34*, 215-223.

114. Lai, F.; Huang, M.; Wong, D. Ehd-enhanced water evaporation. *Drying Technology* **2004**, *22*, 597-608.

115. Kasayapanand, N.; Kiatsiriroat, T. Numerical modeling of the electrohydrodynamic effect to natural convection in vertical channels. *International communications in heat and mass transfer* **2007**, *34*, 162-175.

116. Rouaud, O.; Havet, M. Assessment of the electrohydrodynamic drying process. *Food and Bioprocess Technology* **2009**, *2*, 240-247.

117. Lu, Y.; Sur, A.; Pascente, C.; Annapragada, S.R.; Ruchhoeft, P.; Liu, D. Dynamics of droplet motion induced by electrowetting. *International Journal of Heat and Mass Transfer* **2017**, *106*, 920-931.

118. Satyanarayana, T.; Ajay, G.; Reddy, K.; Rajesh, V. Design and simulation of micro electro wetting liquid lens for miniature cameras. *International Journal of Science and Research* **2013**, *2*, 5.

119. Nahar, M.M.; Bindiganavane, G.S.; Nikapitiya, J.; Moon, H. In *Numerical modeling of 3d electrowetting droplet actuation and cooling of a hotspot*, COMSOL CONFERENCE, 2015; pp 1-7.

120. Guan, Y. A numerical study of microfluidic droplet motions in parallel-plate electrowetting-on-dielectric (ewod) devices. PhD dissertation, The University of Texas at Arlington Texas, USA, May 2015.

121. Ai, Y.; Joo, S.W.; Jiang, Y.; Xuan, X.; Qian, S. Transient electrophoretic motion of a charged particle through a converging–diverging microchannel: Effect of direct current-dielectrophoretic force. *Electrophoresis* **2009**, *30*, 2499-2506.

122. Verheijen, H.; Prins, M. Reversible electrowetting and trapping of charge: Model and experiments. *Langmuir* **1999**, *15*, 6616-6620.

123. Pallas, N.; Harrison, Y. Colloids surfaces, 43 (1990) 169. S. H&d, y. Hamnerius and 0. Nilsson. *J. Appl. Phys* **1976**, *47*, 2433.

124. Virgilio, V.d. Contactless electrowetting. PhD, Universitat Politècnica de Catalunya, Barcelona, Spain, October 2015.

125. Kuo, J.S.; Spicar-Mihalic, P.; Rodriguez, I.; Chiu, D.T. Electrowetting-induced droplet movement in an immiscible medium. *Langmuir* **2003**, *19*, 250-255.

126. Khodayari, M.; Hahne, B.; Crane, N.B. Long life electrochemical diodes for continuous electrowetting. *Journal of The Electrochemical Society* **2014**, *161*, E105-E111.

127. Gupta, R.; Goddard, N. In *Integration of leaky waveguide detection with electrowetting on dielectric digital microfluidic devices*, Journal of Physics: Conference Series, 2013; IOP Publishing: p 012005.

128. Andreas, J.; Hauser, E.; Tucker, W. Boundary tension by pendant drops1. *The Journal of Physical Chemistry* **1938**, *42*, 1001-1019.

129. Gomez, A.; Tang, K. Charge and fission of droplets in electrostatic sprays. *Physics of Fluids* **1994**, *6*, 404-414.

130. Biegaj, K.W.; Rowland, M.G.; Lukas, T.M.; Heng, J.Y. Surface chemistry and humidity in powder electrostatics: A comparative study between tribocharging and corona discharge. *ACS Omega* **2017**, *2*, 1576-1582.

131. Berge, B. In *Liquid lens technology: Principle of electrowetting based lenses and applications to imaging*, Micro Electro Mechanical Systems, 2005. MEMS 2005. 18th IEEE International Conference on, 2005; IEEE: pp 227-230.

APPENDICES (MODEL EQUATIONS)

Details of COMSOL Simulation for contact Electrowetting

In COMSOL, the axisymmetric design is chosen due to the schematic of the droplet on the substrate. The rest of the steps are provided below:

-Definitions: The first step of simulating for contact electrowetting is providing the parameters as shown in Table 4. These amounts are plugged in the COMSOL.

Table 4. Parameter uses in the contact electrowetting.

Name	Expression	Value	Description
Theta0	90	1.5708 rad	Zero voltage contact angle
gamma	0.072	0.072 N/m	Surface tension
epsr	2.65	2.65	Relative dielectric constant
d_f	0.03	3E−5 m	Dielectric thickness

The voltage and contact angle provided in the variable part in Table 5 that was calculated from curve fitting of the MKWD voltage was applied in the variable section with the contact angle (64).

Table 5. Variables information in COMSOL.

Name	Expression	Unit	Description
theta	acos(cos(theta0) + V^2*epsr*epsilon0_const/(2*gamma*d_f))	deg	Contact angle
V	-3.909655708607368E-7[V/s]*t^6 + 5.660499334244992E-5[V/s]*t^5 - 0.003054451422720[V/s]*t^4 + 0.074539710922610[V/s]*t^3 - 0.801776710957060[V/s]*t^2 + 2.533455101584655[V/s]*t - 11.530789606238486	V	MKWD Voltage

- Geometry: The geometry of the droplet with the diameter of 2.4 mm with the electrode inside is provided in Fig. 66.

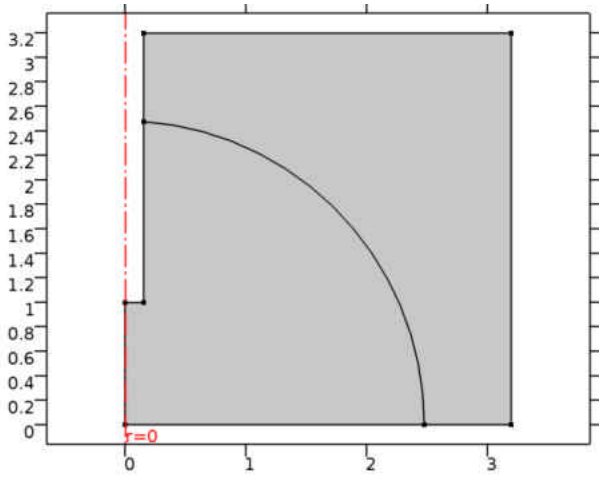

Fig. 66. The geometry of the axisymmetric droplet.

- Materials: The droplet properties are provided in Table 7 with the water parameters (Table 6) and the domain (Fig. 67)

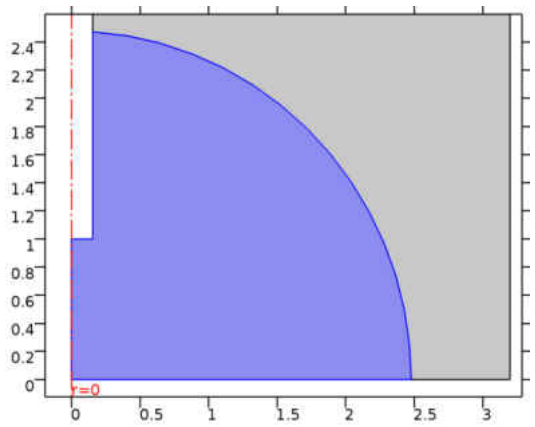

Fig. 67. Water is chosen in the droplet.

Table 6. Water parameters

Name	Value	Unit
Dynamic viscosity	eta(T[1/K])	Pa*s
Density	rho(T[1/K])[kg/m^3]	kg/m^3

Table 7. Water properties

Description	Value
Dynamic viscosity	eta(T[1/K])
Ratio of specific heats	1.0
Electrical conductivity	{{5.5e-6[S/m], 0, 0}, {0, 5.5e-6[S/m], 0}, {0, 0, 5.5e-6[S/m]}}
Heat capacity at constant pressure	Cp(T[1/K])[J/(kg*K)]
Density	rho(T[1/K])[kg/m^3]
Thermal conductivity	{{k(T[1/K])[W/(m*K)], 0, 0}, {0, k(T[1/K])[W/(m*K)], 0}, {0, 0, k(T[1/K])[W/(m*K)]}}
Speed of sound	cs(T[1/K])[m/s]
Relative permittivity	{{80, 0, 0}, {0, 80, 0}, {0, 0, 80}}

The top domain is chosen as air is shown in Fig. 68 with the air property (Table 8) and the water properties (Table 8).

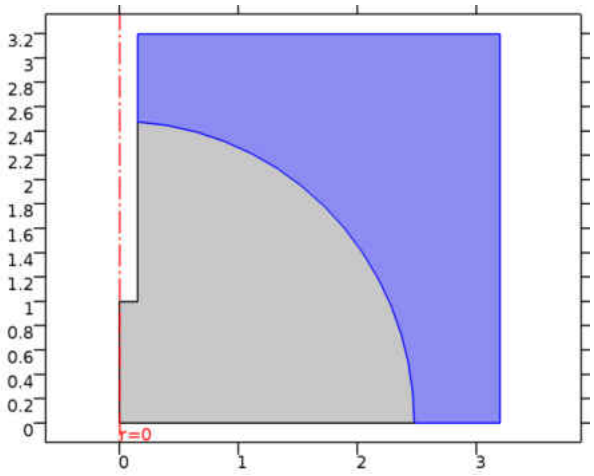

Fig. 68. Air is chosen in the droplet.

Table 8. Air parameter

Name	Value	Unit
Dynamic viscosity	eta(T[1/K]) [123]	Pa*s
Density	rho(pA[1/Pa],T[1/K])[kg/m^3]	kg/m^3

Table 9. Air properties

Description	Value
Relative permeability	{{1, 0, 0}, {0, 1, 0}, {0, 0, 1}}
Relative permittivity	{{1, 0, 0}, {0, 1, 0}, {0, 0, 1}}
Dynamic viscosity	eta(T[1/K])
Ratio of specific heats	1.4
Electrical conductivity	{{0[S/m], 0, 0}, {0, 0[S/m], 0}, {0, 0, 0[S/m]}}
Heat capacity at constant pressure	Cp(T[1/K])[J/(kg*K)]
Density	rho(pA[1/Pa], T[1/K])[kg/m^3]
Thermal conductivity	{{k(T[1/K])[W/(m*K)], 0, 0}, {0, k(T[1/K])[W/(m*K)], 0}, {0, 0, k(T[1/K])[W/(m*K)]}}
Speed of sound	cs(T[1/K])[m/s]

- Laminar Two-Phase Flow, Moving Mesh (physic): After defining the geometry and the material, the physics of Laminar Two-Phase Flow, Moving Mesh should be chosen by clicking the whole domains.

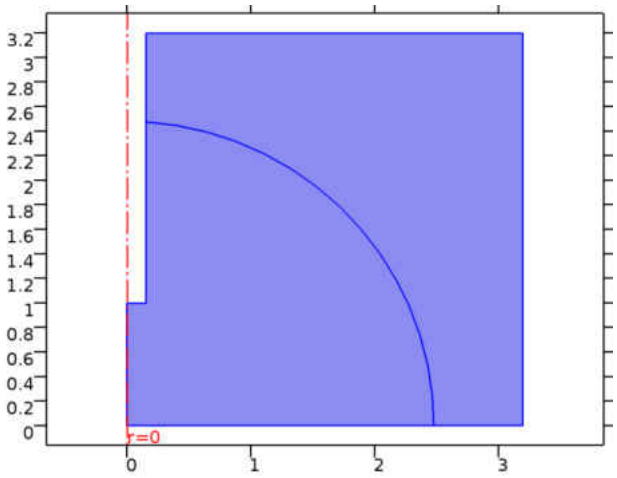

Fig. 69. Chosen domains for Laminar Two-Phase Flow, Moving Mesh.

- Free Deformation: All fluids are chosen as free deformation by default of the software.

- Prescribed Mesh Displacement: The vertical walls are clicked as a Prescribed Mesh Displacement boundary condition (blue line in Fig. 70). Regarding Table 10, the vertical walls do not have a movement in the r direction.

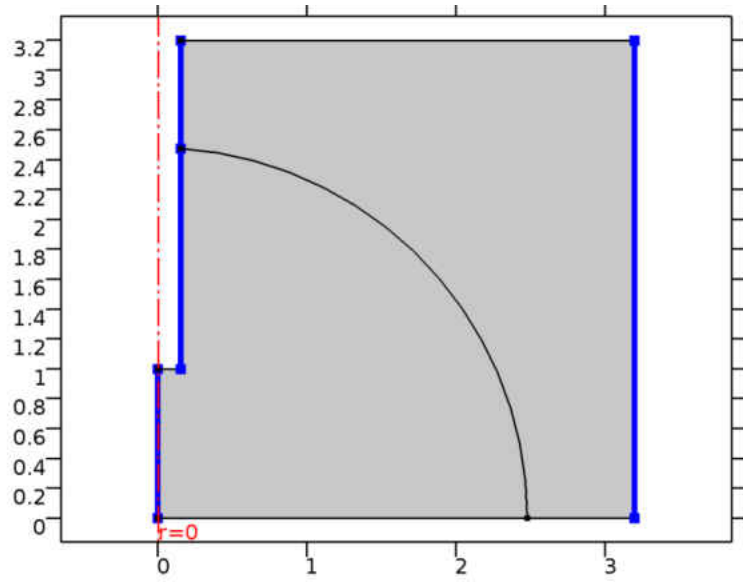

Fig. 70. Prescribed mesh displacement 1.

Table 10. Shape functions

Constraint	Constraint force	Shape function	Selection
R-tpfmm.r_free	test(-tpfmm.r_free)	Lagrange (Linear)	Boundaries 1, 4–5, 8
0	0		Boundaries 1, 4–5, 8
0	test(-tpfmm.z_free)	Lagrange (Linear)	Boundaries 1, 4–5, 8

-Axial symmetry: The boundary on the left bottom is chosen axial symmetry (blue line in Fig. 71) due to the definition of the cylindrical coordinate.

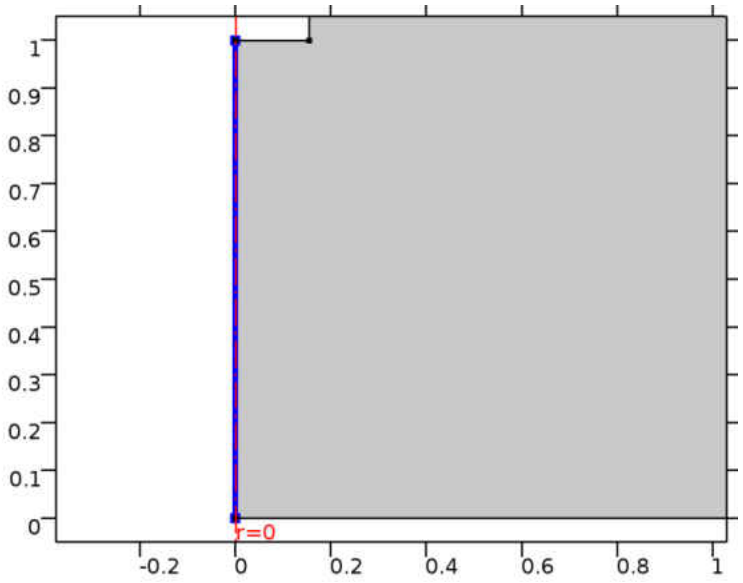

Fig. 71. Axial symmetry boundary condition.

- Wall: The walls in the device are defined in the blue line in Fig. 72, and the equation for this boundary is u=0, where u contains velocity in r and z coordinates.

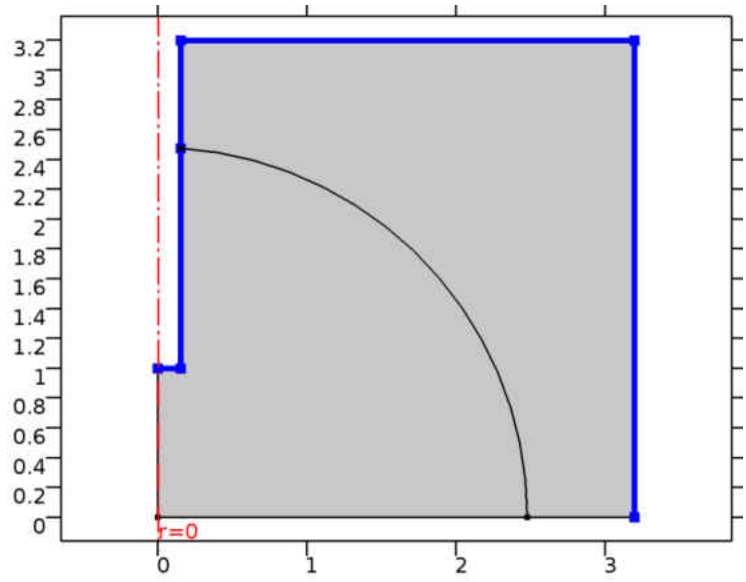

Fig. 72. Wall boundary condition.

-Initial Values: For the whole domain, the velocity field and pressure were chosen as 0.

-Fluid-Fluid interface: The boundary condition for the Fluid-Fluid interface is the blue line in Fig. 73.

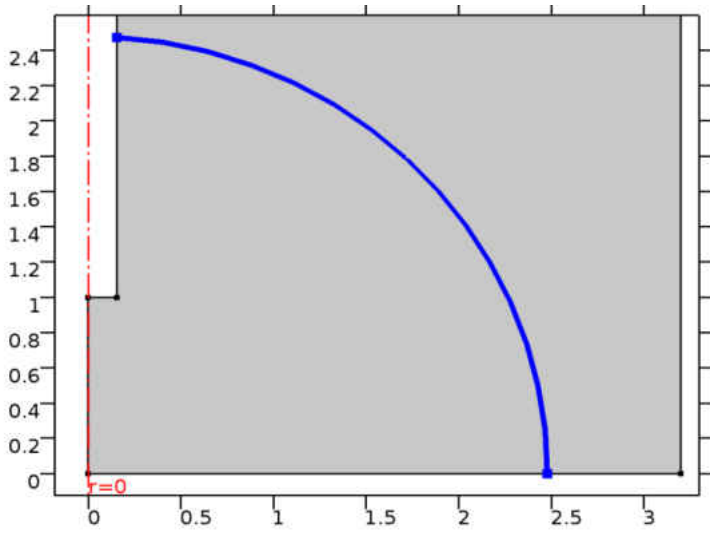

Fig. 73. Fluid-Fluid interface boundary condition.

$$u_1 = u_2,\ \ u_1.T_1 - n_1.T_2 = \sigma(\nabla_t.n_1)n_1 - \nabla_t\sigma \quad (84)$$

$$u_1 = u_2 + M_f(\frac{1}{\rho_1} + \frac{1}{\rho_2})\ n_1 \quad (85)$$

$$u_{mesh} = (u_1.n_1) - \frac{M_f}{\rho_1}\ n_1 \quad (86)$$

where $M_f, T_1, T_2, \nabla_t, n_1, n_2, \rho_1, \rho_2, \sigma, u_1$ and u_2 represented mass flux (considered zero) and interface normal Surface tension coefficients.

-Wall-Fluid interface: The contact angle is chosen at the point of the air and water and vertical surface area, and the θ is defined in the theta parameters section.

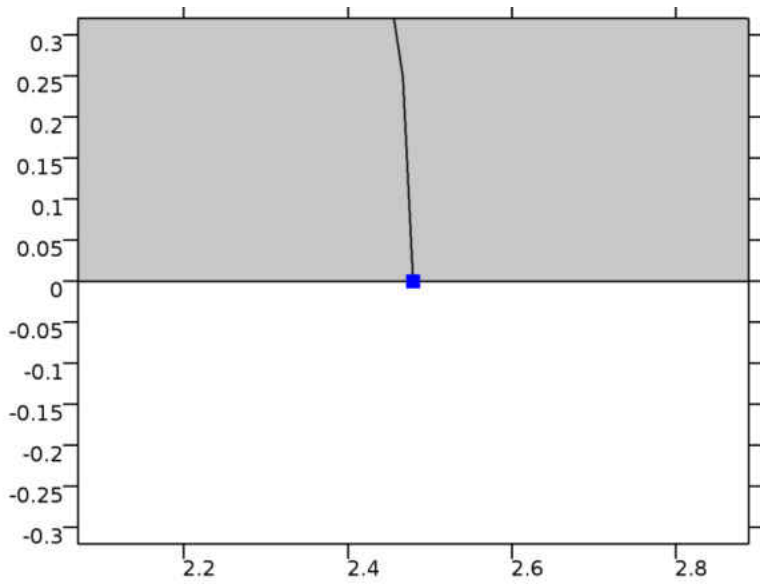

Fig. 74. the points that contact angle is chosen

- Prescribed Mesh Displacement: All vertical walls (blue line in Fig. 75) are chosen at zero mesh displacement in the z-direction.

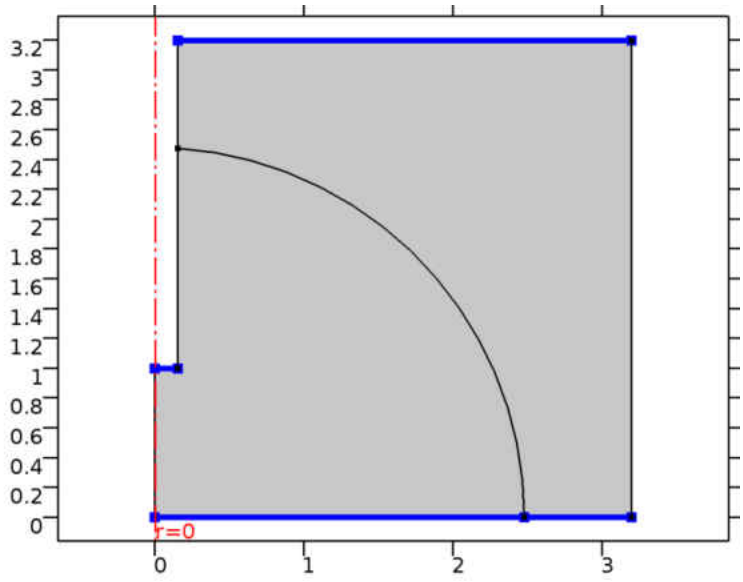

Fig. 75. Prescribed Mesh Displacement.

Navier slip: The bottom wall is chosen Navier slip (blue shown in Fig. 76). The Navier slip is as follows:

$$u.n_{wall} = 0 \tag{87}$$

$$F_{fr} = -\frac{\mu}{\beta}u \tag{88}$$

where n, μ, β present normal, viscosity, and the slip length (β =0.2*h, where h is mesh element size),

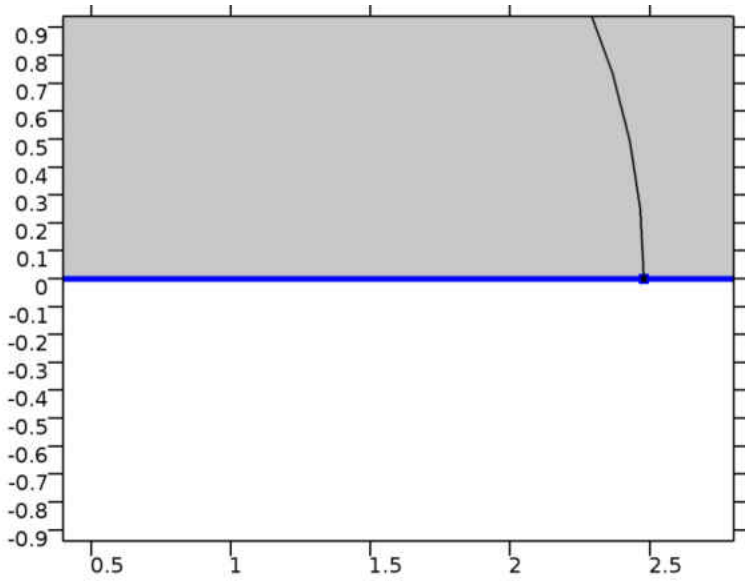

Fig. 76. Navier slip on the bottom wall.

- Mesh: Mesh statistics are provided in

Table 11 based on the normal element size that is an option in the mesh setting. Thus, the result of building up the mesh is in Fig. 77. Mesh on the model of electrowetting.

Table 11. Mesh statistics

Description	**Value**
Minimum element quality	0.7437
Average element quality	0.9844
Triangular elements	15422
Edge elements	400
Vertex elements	8

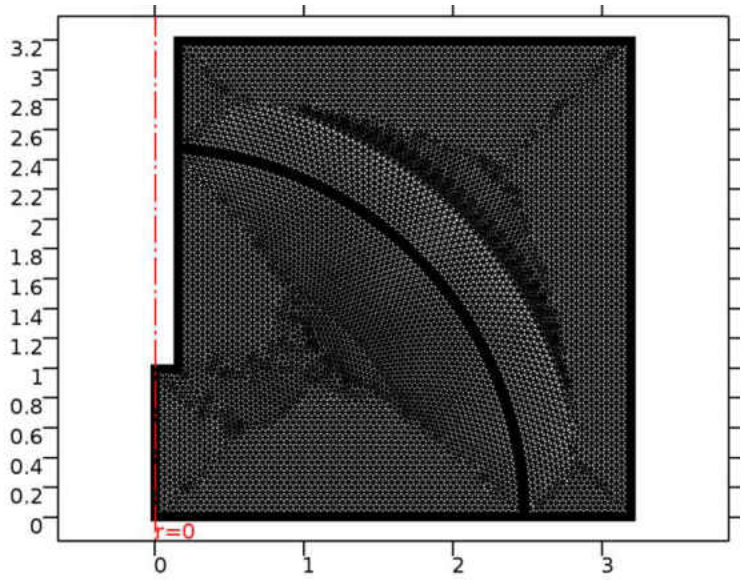

Fig. 77. Mesh on the model of electrowetting.

Table 12. Mesh size in fluid dynamics

Description	**Value**
Calibrate for	Fluid dynamics
Maximum element size	0.0416
Minimum element size	4.8E-4
Curvature factor	0.25
Maximum element growth rate	1.08
Predefined size	Extra fine

Time-Dependent: Regarding the time that the experiment result was obtained, the range of the time is chosen between 0 to 57 with the time step of 1.

- A solution of the model: By completing all the mentioned steps, the amount of the result can be calculated. By clicking the calculated bottom, the software will be run. Then, the result can be ready for post-processing.

Details of COMSOL Simulation for contactless Electrowetting:

Regarding the physical concept of the contactless electrowetting, the boundary condition will change while the droplet rises up and then collapse suddenly. Thus, there are two phases in the simulation:

Phase one

Parameters and variable: The parameters and variable that were applied in the simulation are provided in Table 13 and

Table 14.

Table 13. Parameters

Name	Expression	Value	Description
perm_water	80	80	Permittivity, water
perm_air	1	1	Permittivity, air

Table 14. Input variable in the simulation.

Name	Expression	Unit	Description
Tem11	-epsilon0_const*epsilon_r/2*(es.Er^2 + es.Ez^2) + epsilon0_const*epsilon_r*es.Er^2	Pa	Maxwell stress tensor, 11-component
Tem22	-epsilon0_const*epsilon_r/2*(es.Er^2 + es.Ez^2) - epsilon0_const*epsilon_r*es.Ez^2	Pa	Maxwell stress tensor, 22-component
Tem12	epsilon0_const*epsilon_r*es.Er*es.Ez	Pa	Maxwell stress tensor, 12-component
Tem21	epsilon0_const*epsilon_r*es.Er*es.Ez	Pa	Maxwell stress tensor, 21-component
Fr	d(Tem11, r) + d(Tem21, z)	N/m^3	Force, x-component
Fz	d(Tem12, r) + d(Tem22, z)	N/m^3	Force, y-component

Name	Expression	Unit	Description
epsilon_r	0.22*perm_water + 0.77*perm_air		Phase dependent permittivity

The geometry of the droplet is provided in Fig. 78. The droplet volume is 10µl. And the diameter of the geometry is 1.7mm.

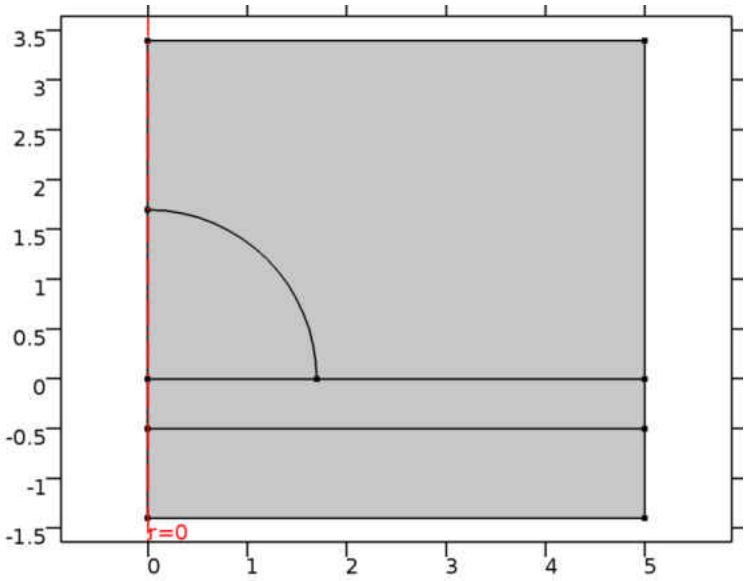

Fig. 78. The geometry of the contactless electrowetting droplet.

- Materials: The domain for water droplet and air are the same as previous contact electrowetting. The bottom material in the blue domain is chosen Titanium beta-215 (Fig. 79)

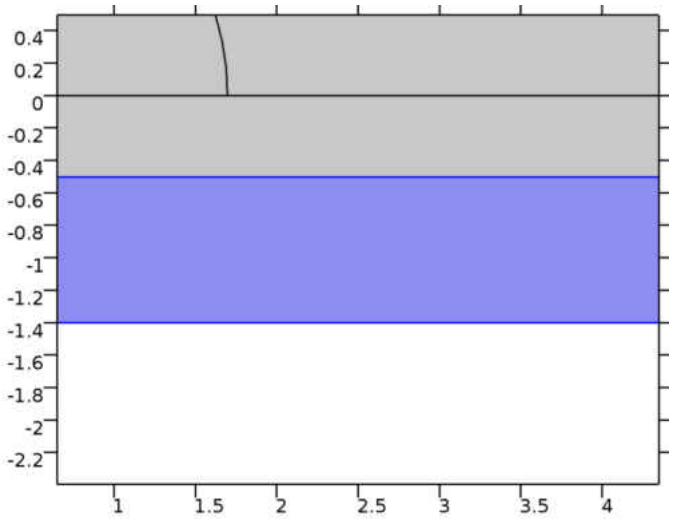

Fig. 79. Chosen Titanium beta-215 domain.

Table 15. Chosen Titanium beta

Description	Value
Relative permeability	{{1, 0, 0}, {0, 1, 0}, {0, 0, 1}}
Electrical conductivity	{{7.407e5[S/m], 0, 0}, {0, 7.407e5[S/m], 0}, {0, 0, 7.407e5[S/m]}}
Coefficient of thermal expansion	{{7.06e-6[1/K], 0, 0}, {0, 7.06e-6[1/K], 0}, {0, 0, 7.06e-6[1/K]}}
Heat capacity at constant pressure	710[J/(kg*K)]
Relative permittivity	{{1, 0, 0}, {0, 1, 0}, {0, 0, 1}}
Density	4940[kg/m^3]
Thermal conductivity	{{7.5[W/(m*K)], 0, 0}, {0, 7.5[W/(m*K)], 0}, {0, 0, 7.5[W/(m*K)]}}

The domain with the blue color is chosen PDMS with the thickness of 0.5 mm as shown in Fig. 80.

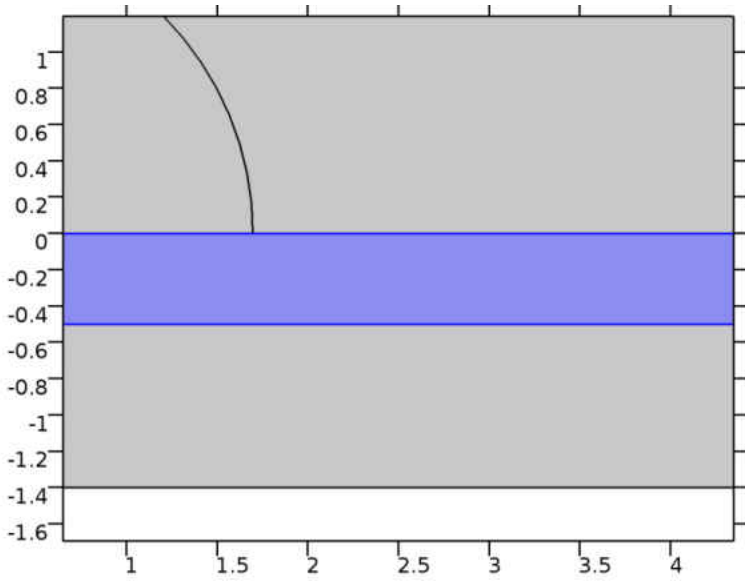

Fig. 80. PDMS – Polydimethylsiloxane domain.

The property of Polydimethylsiloxane PDMS is added in COMSOL (Table 16)

Table 16. Polydimethylsiloxane PDMS properties

Description	**Value**
Coefficient of thermal expansion	{{9e-4[1/K], 0, 0}, {0, 9e-4[1/K], 0}, {0, 0, 9e-4[1/K]}}
Heat capacity at constant pressure	1460[J/(kg*K)]
Relative permittivity	{{2.75, 0, 0}, {0, 2.75, 0}, {0, 0, 2.75}}
Density	970[kg/m^3]
Thermal conductivity	{{0.16[W/(m*K)], 0, 0}, {0, 0.16[W/(m*K)], 0}, {0, 0, 0.16[W/(m*K)]}}
Young's modulus	750[kPa]
Poisson's ratio	0.50

- Electrostatic: All domains are chosen as the electrostatic physics. The boundaries for electrostatic physic are contained as follows:

- Charge Conservation: All domains are chosen as conservation domains.

- Axial Symmetry: The blue line in Fig. 81 is activated as Axial Symmetry.

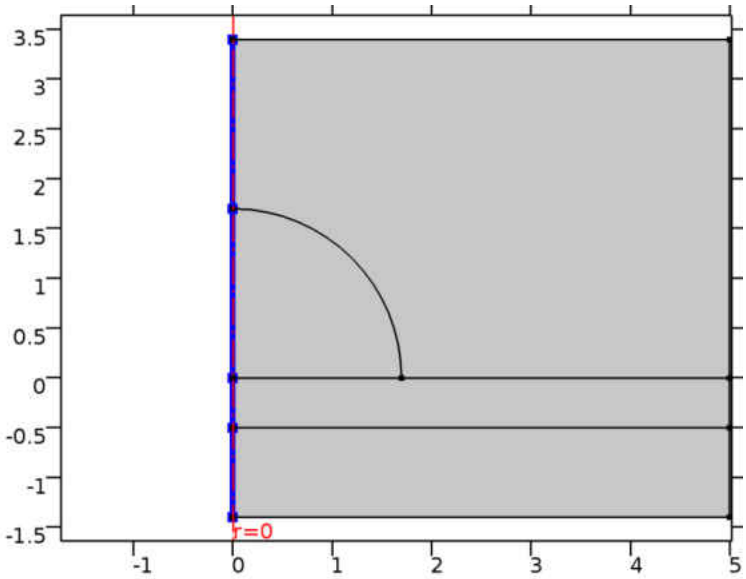

Fig. 81. Axial Symmetry boundary condition

-Zero Charge: The right wall is chosen as positive as shown in Fig. 82. The meaning of the zero charge contains n. D=0, where n and D denote normality of the surface and surface charge density.

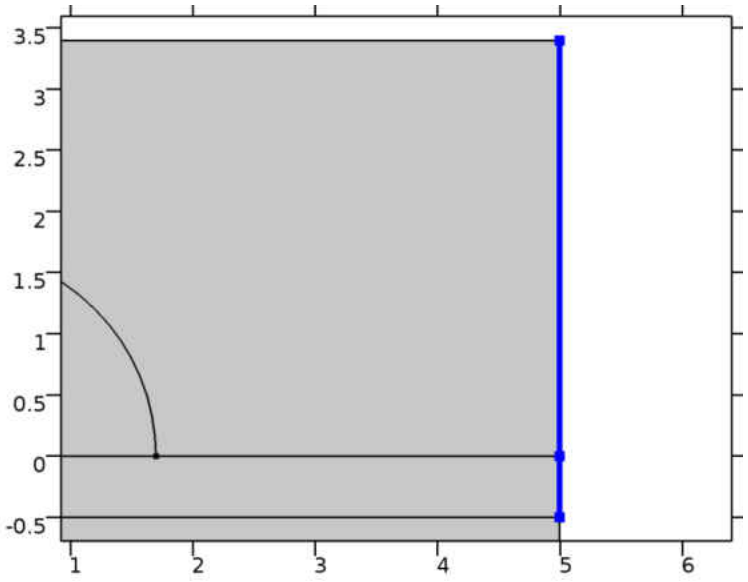

Fig. 82. Zero charge boundary condition.

- Initial Values: For the initial value, all of the domains are chosen. Moreover, the amount of electrical potential is zero.

- Electrical potential: The top wall in the electrostatic physic is chosen as a potential applied to the device due to the top electrode in the device as shown in Fig. 83. And the more information of the amount of voltage is considered 1060.9V.

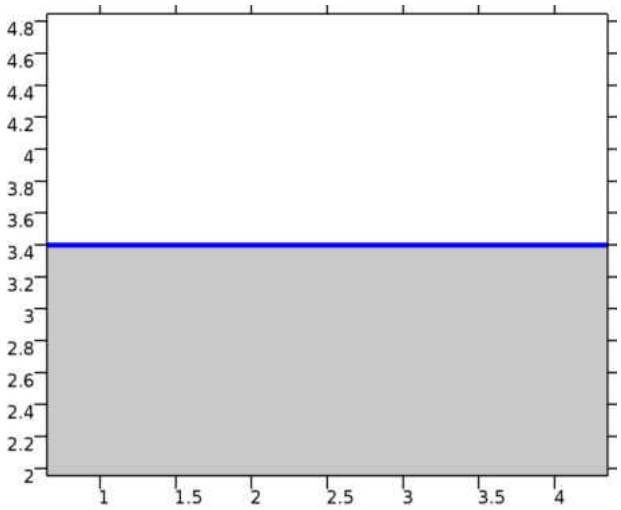

Fig. 83. Electrical potential

- Laminar Two-Phase Flow, Moving Mesh: The domains that are chosen for Laminar Two-Phase Flow. Moving Mesh is shown in Fig. 84.

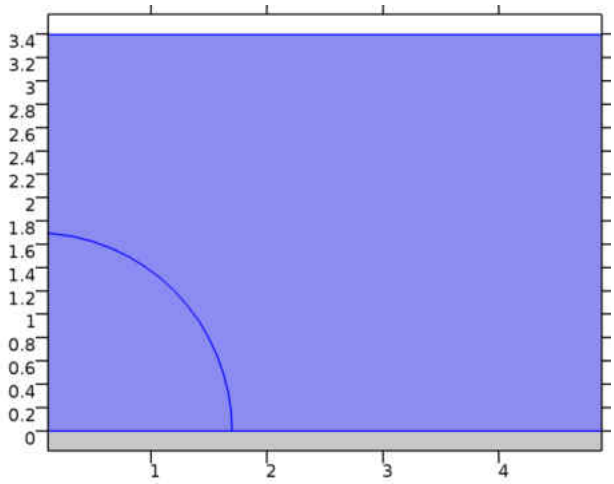

Fig. 84. Laminar Two-Phase Flow, Moving Mesh.

- Free deformation: All of these physics are chosen as free deformation with the amount of initial mesh displacements being zero.

- Prescribed Mesh Displacement: The prescribed mesh displacement on the top and bottom of the wall are considered zero in the z-direction as shown in Fig. 85.

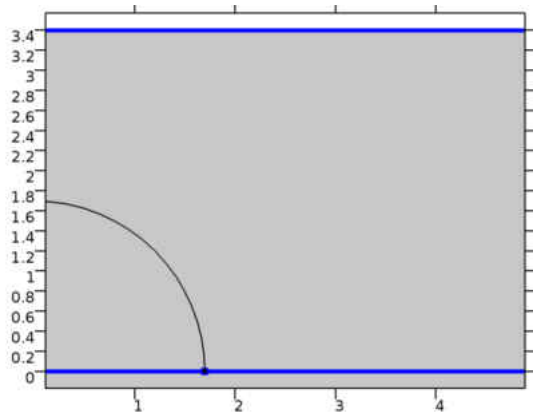

Fig. 85. Prescribed mesh displacement.

- Axial symmetry: The left wall is considered as an axial symmetry since the solution is in r and z coordinates.

- Wall: The top boundary is defined as a wall. Thus, the velocity is zero (u=0)

- Initial Values: All of the Laminar Two-Phase Flow is considered. Additionally, the initial value of the velocity field and pressure are equal zero.

- Prescribed Mesh Displacement: The walls in the z-direction are chosen to be equal zero in the r direction.

- Volume force: All of the domains for Laminar Two-Phase Flow are chosen. Two forces (F_r and F_z) are defined.

- Navier slip: The top of the PDMS layer is chosen as Navier slip, and the governing equation is the same as same contact electrowetting.

- Fluid-Fluid Interface: The interface between the water and air is considered as a fluid-fluid interface, and the governing equation as same as contact electrowetting.

-Mesh: The mesh for the first phase of the contactless electrowetting is in Fig. 86. Mesh for the whole of the domain. Table 17 shows the mesh size that is plugged into the software.

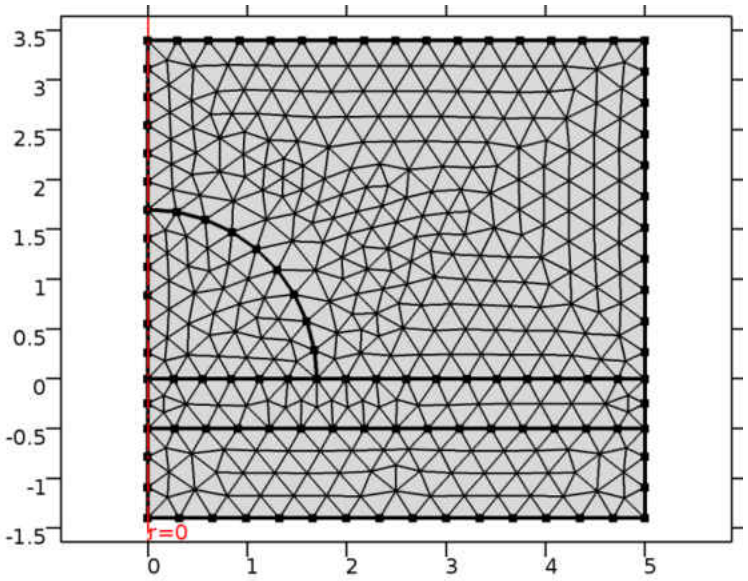

Fig. 86. Mesh for the whole of the domain.

Table 17. Mesh statistics

Description	**Value**
Minimum element quality	0.7962
Average element quality	0.9614
Triangular elements	712
Edge elements	106
Vertex elements	10

Table 18. Size of the mesh

Description	**Value**
Maximum element size	0.335
Minimum element size	0.0015
Curvature factor	0.3
Maximum element growth rate	1.3

-Study: The range of the time for the phase one of the simulation is applied from 0 to 0.5 with the time step of 0.25.

Phase two: The whole of the process of the boundary conditions are the same as the contact electrowetting, but the geometry is the same as the last time at phase one (Fig. 87).

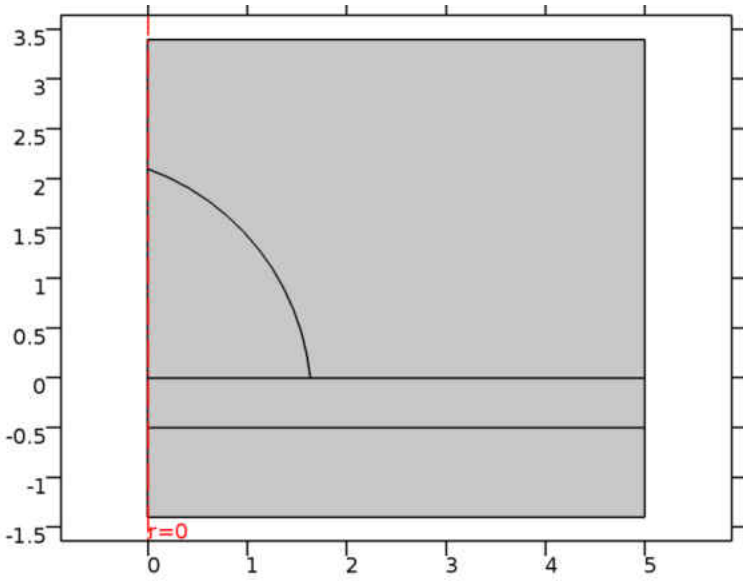

Fig. 87. The geometry of phase two.

The mesh elements in phase two are chosen normal as shown in Fig. 88, and the size of the mesh elements are provided in Table 18. Size of the mesh

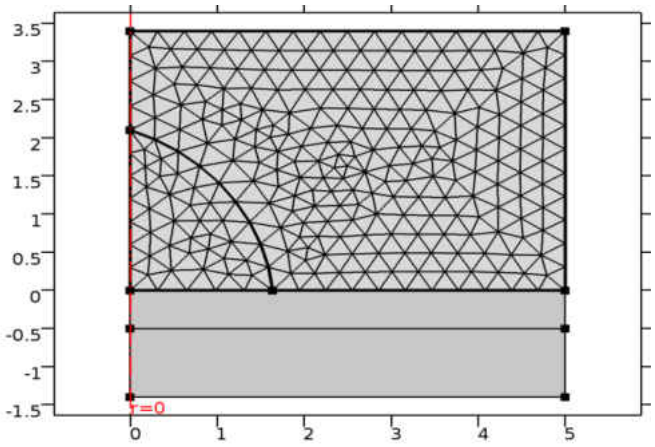

Fig. 88. Mesh for the phase two

Table 19. Mesh setting

Description	**Value**
Maximum element size	0.335
Minimum element size	0.0015
Curvature factor	0.3
Maximum element growth rate	1.3

VITA

Elias Yazdanshenas
635 West 28th street,
Norfolk, VA, 23508

Department of Mechanical and Aerospace Engineering
Old Dominion University
5115 Hampton Blvd, Norfolk, VA 23529

Education:

Azad University Semnan Branch
September 2006-February 2011
Bachelor of Science

Old Dominion University
September 2013- September 2015
Master of Science

Old Dominion University
September 2015- April 2018
Doctor of Philosophy

Publications:

Elias Yazdanshenas, Tang Qiang, Xiaoyu Zhang, Electrowetting Using a Microfluidic Kelvin Water Dropper, Micromachines journal, 25 February 2018

Elias Yazdanshenas, F. Asgari, Es. Yazdanshenas, Experimental investigation of a solar LiCl dryer system, 42nd Annual National Solar Conference – Solar 2013, Baltimore, Maryland, April 16-20, 2013

Elias Yazdanshenas, A. Khalesi Doost, Energy saving of a solar heating system with Phase Change Material (PCM) heat exchanger, ISES Solar World Congress, Kassel University, Germany, 28 Aug-2 Sep 2011

Elias Yazdanshenas, A. Khalesi Doost, Experimental investigation on a shell and tube heat exchanger for storing solar heat energy by Phase Change Material (PCM), Published in First Annual Clean Energy Conference on International Center for Science, High Technology & Environmental Sciences, Kerman, 2011